Supplemental figures

Geochemistry, petrologic evolution, and ore deposits of the Miocene Bodie Hills Volcanic Field, California and Nevada

Edward A. du Bray, David A. John, Brian L. Cousens, Leslie A. Hayden and Peter G. Vikre

American Mineralogist: March 2016
Deposit AM-16-35440

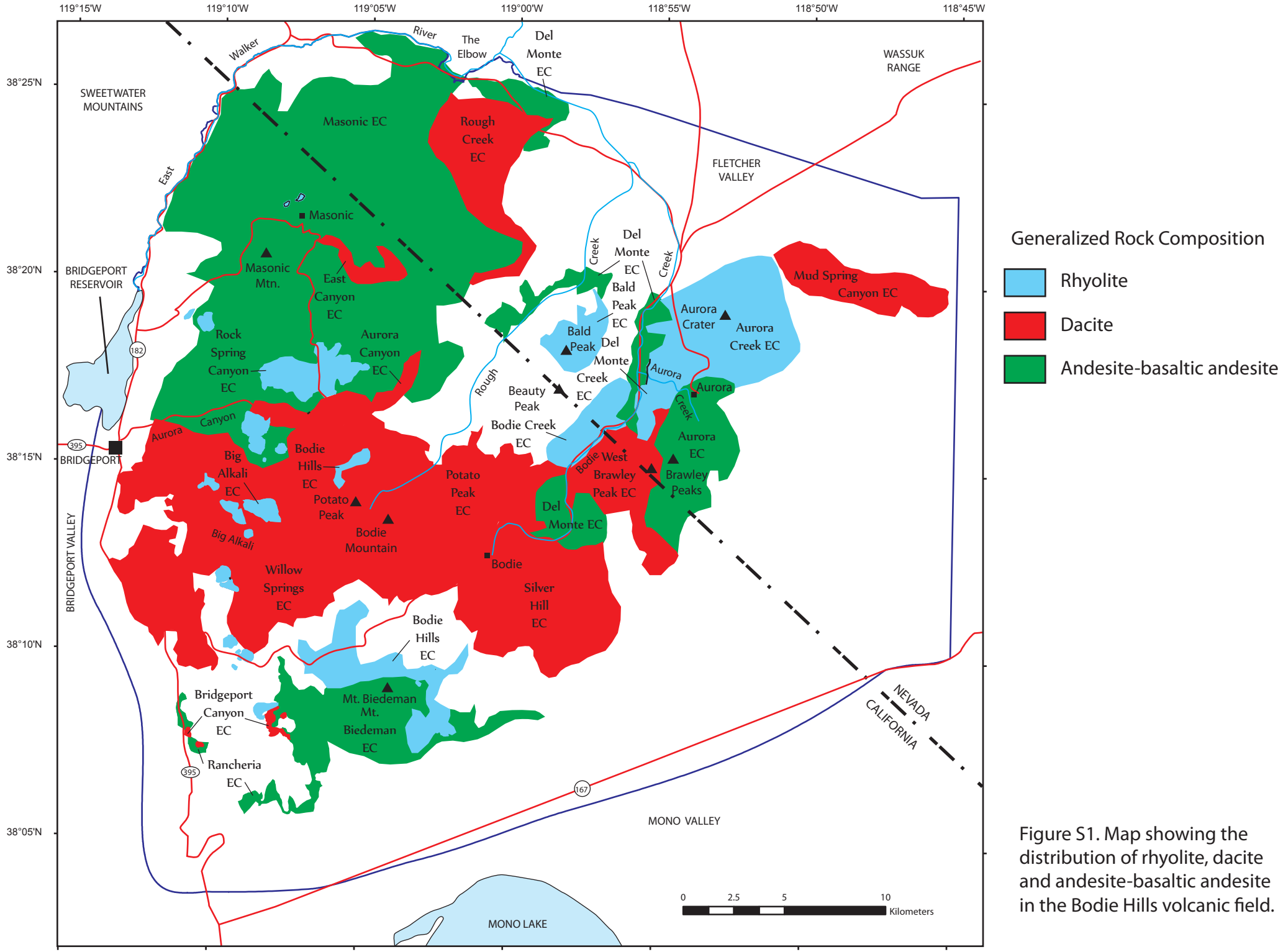

Figure S1 du Bray, John, Cousens, Hayden, and Vikre

Figure S1. Map showing the distribution of rhyolite, dacite and andesite-basaltic andesite in the Bodie Hills volcanic field.

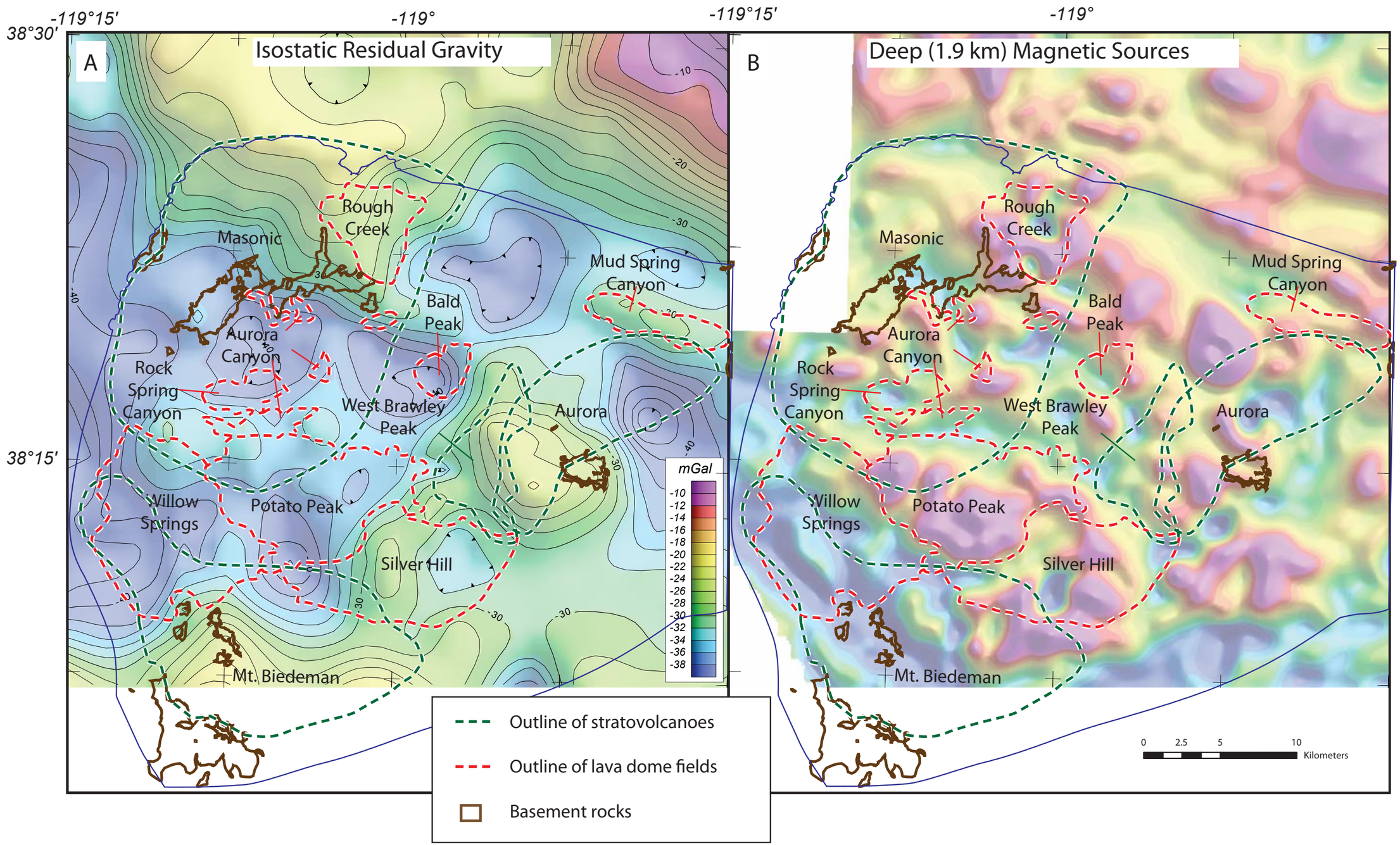

Supplemental figure 2. Maps showing (A) isostatic residual gravity anomalies and (B) magnetic anomalies filtered to emphasize deep (1.9 km) magnetic sources, modified from John et al. (2012). Outline of stratovolcanoes and lava dome fields from John et al. (2015). John et al. (2012, 2015) interpreted these figures to show:

1. The Bodie Hills Volcanic Field has complex magnetic signatures that in most cases are associated with mapped lava domes and inferred vents of stratovolcanoes. Good examples include magnetic highs underlying the Potato Peak, Rough Creek, Silver Hill, and parts of the Aurora Canyon dome fields and areas directly under inferred vents of the Mount Biedeman, West Brawley Peak, and Masonic stratovolcanoes.
2. Pronounced negative gravity anomalies are notable beneath many of the dome complexes suggesting that the domes underlie low density plutons.
3. The broad negative gravity anomaly in the center of the Bodie Hills may reflect the deeper part of the volcanic field and suggests an underlying composite pluton.

Figure S2 du Bray, John, Cousens, Hayden, and Vikre

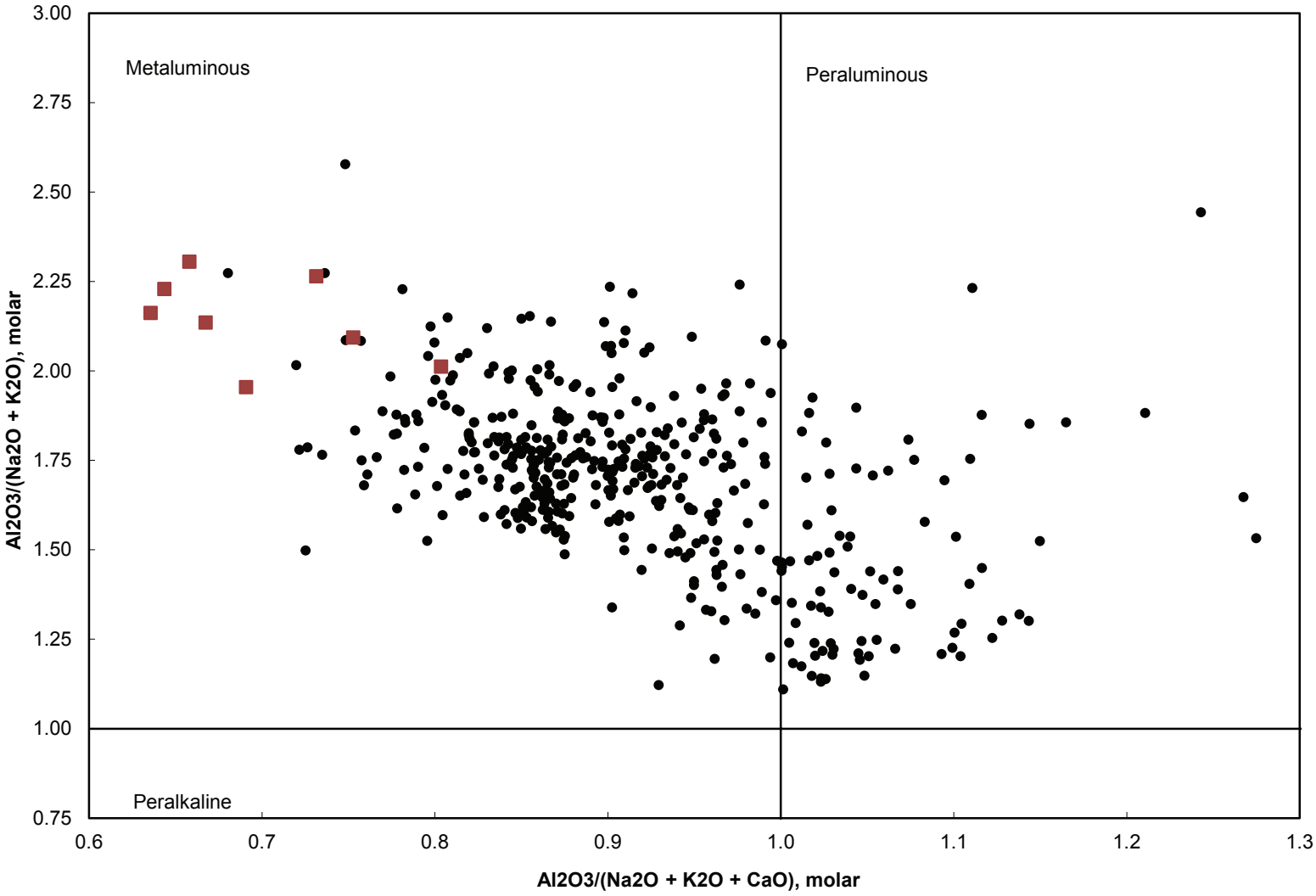

Figure S3. Variation diagram showing molar major-oxide compositions of Bodie Hills volcanic field rocks (black dots) as a function of relative alumina and alkali saturation; compositions of the most primitive samples, which represent possible parental magma compositions, are shown by tan squares.

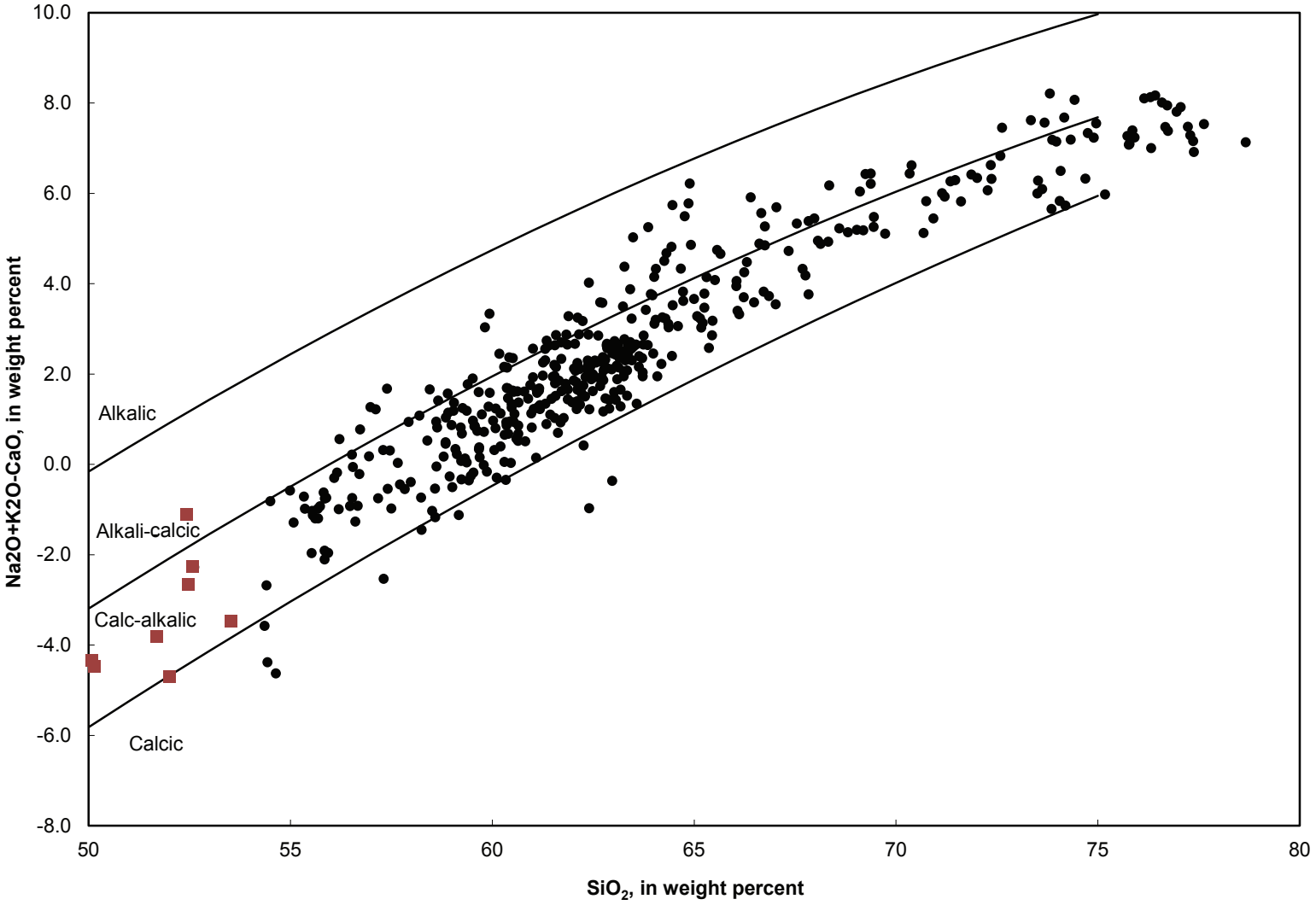

Figure S4. Na2O + K2O – CaO versus SiO2 variation diagram showing the composition of Bodie Hills volcanic field rocks (black dots) relative to boundaries between alkalic, alkali-calcic, calc-alkalic, and calcic rock series. Boundaries between various rock series from Frost et al. (2001); compositions of the most primitive samples, which represent possible parental magma compositions, are shown by tan squares.

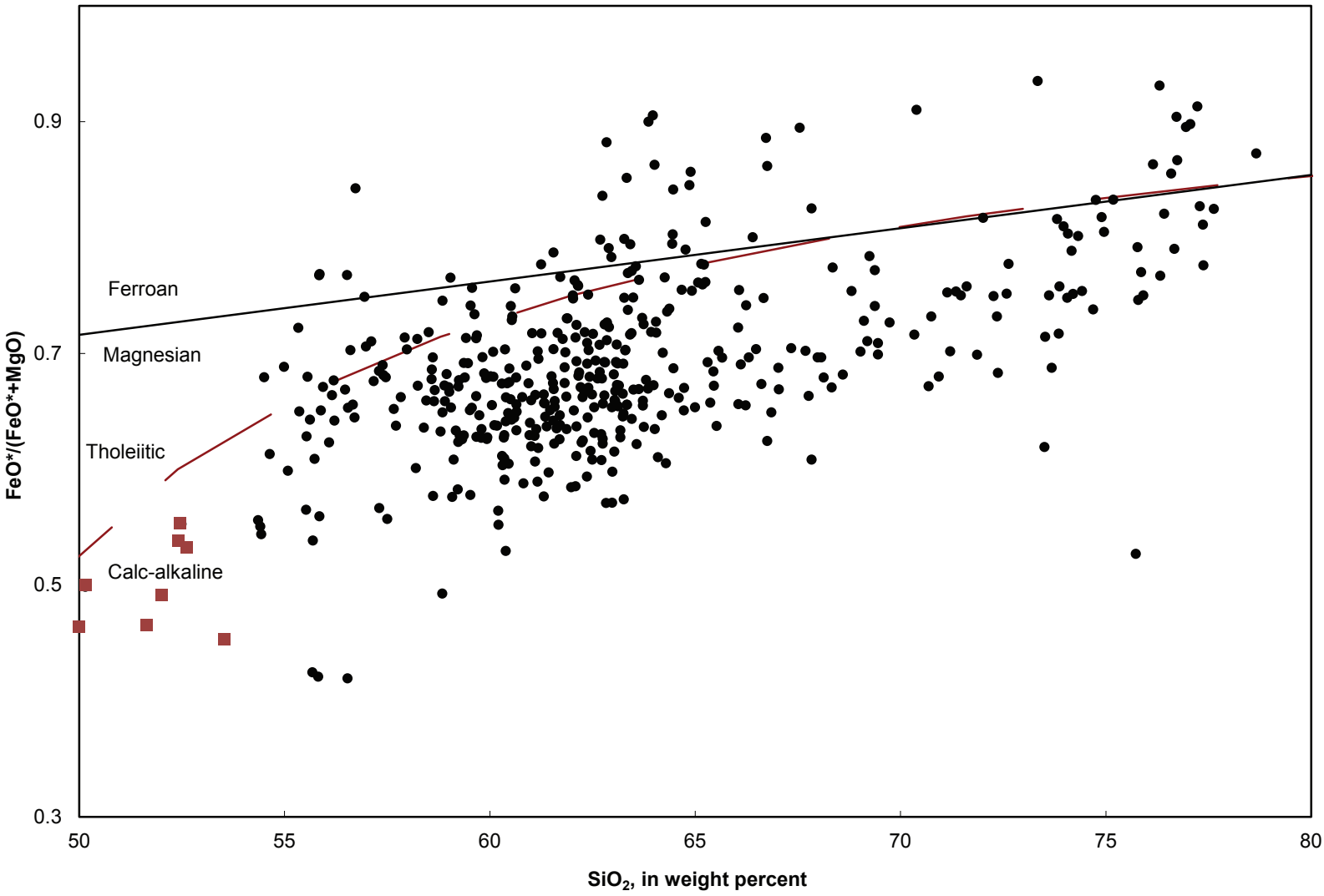

Figure S5. FeO*/(FeO* + MgO) variation diagram showing the composition of volcanic rocks (black dots) erupted in the Bodie Hills volcanic field relative to boundaries between ferroan and magnesian rocks as well as between tholeiitic and calc-alkaline rocks; compositions of the most primitive samples, which represent possible parental magma compositions, are shown by tan squares. Ferroan versus magnesian boundary (black line) from Frost et al. (2001); tholeiitic versus calc-alkaline boundary (dashed red line) from Miyashiro (1974) southern arc segment rocks.

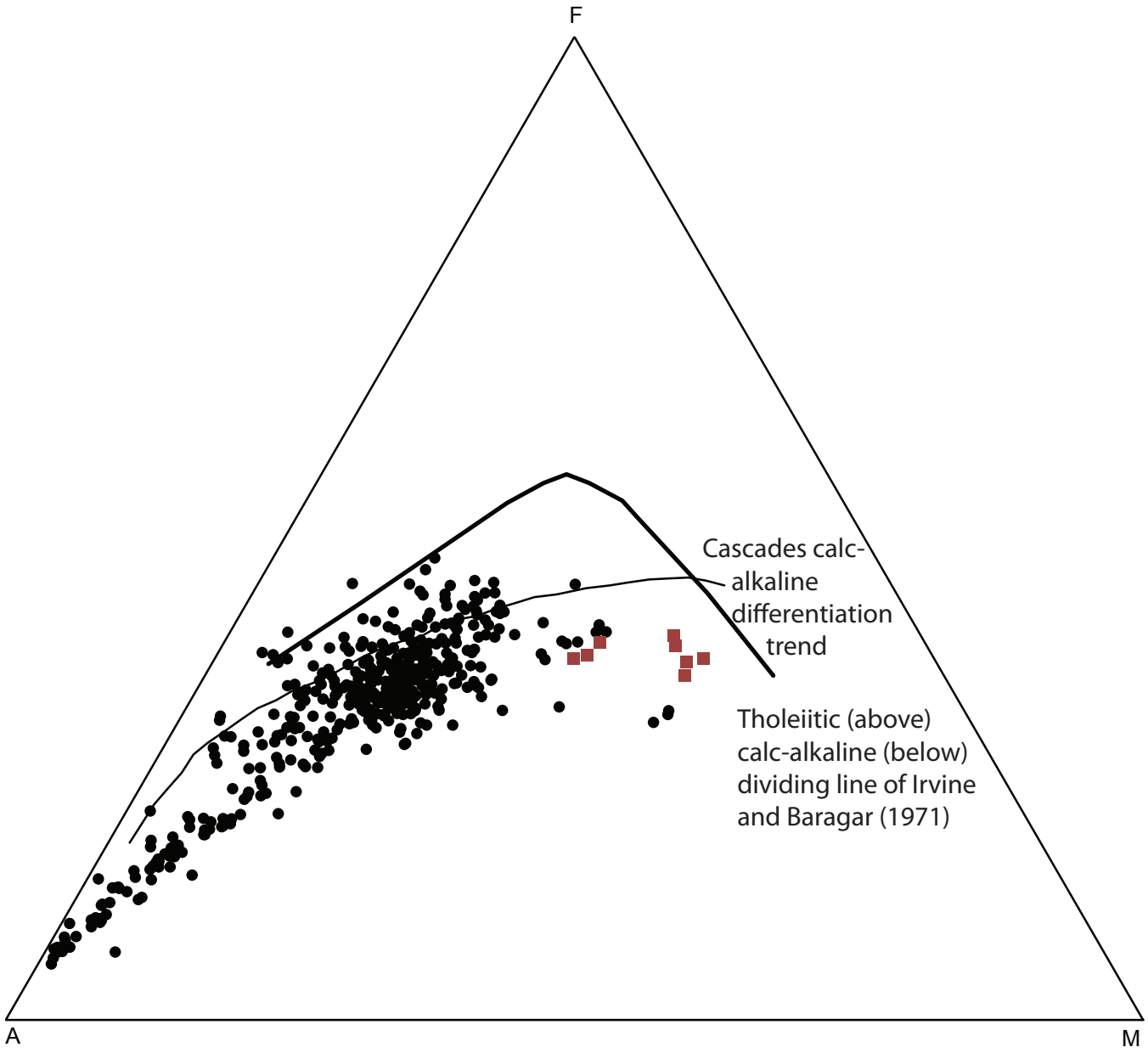

Figure S6. Ternary AFM (Na2O + K2O, FeO*, MgO) diagram showing compositions of volcanic rocks (black dots) erupted in the Bodie Hills volcanic field relative to the tholeiitic versus calc-alkaline dividing line of Irvine and Baragar (1971); compositions of the most primitive samples, which represent possible parental magma compositions, are shown by tan squares.

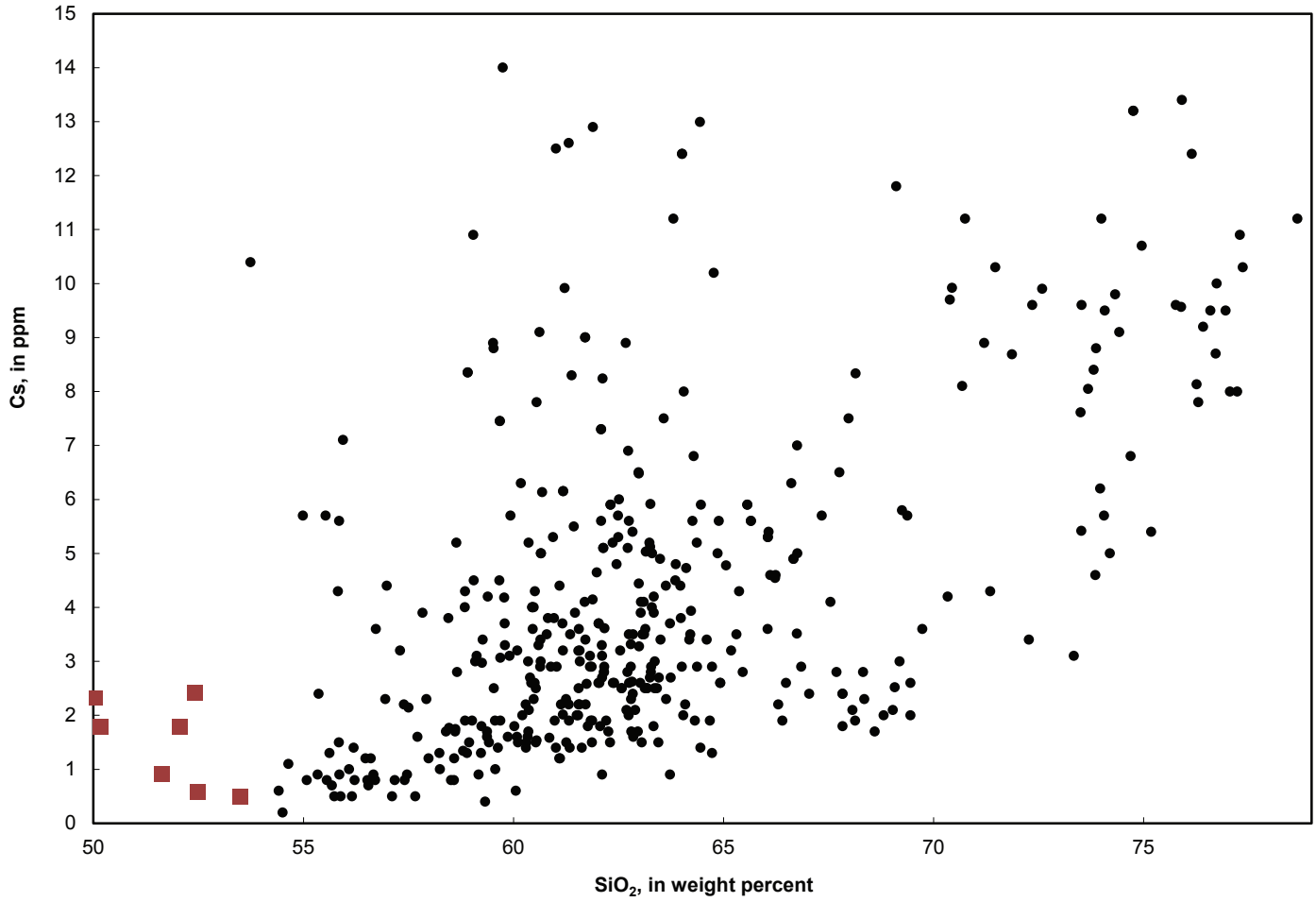

Figure S7. Variation diagram showing Cs (ppm) versus SiO2 (wt%) abundances in Bodie Hills volcanic field rocks (black dots); compositions of the most primitive samples, which represent possible parental magma compositions, are shown by tan squares.

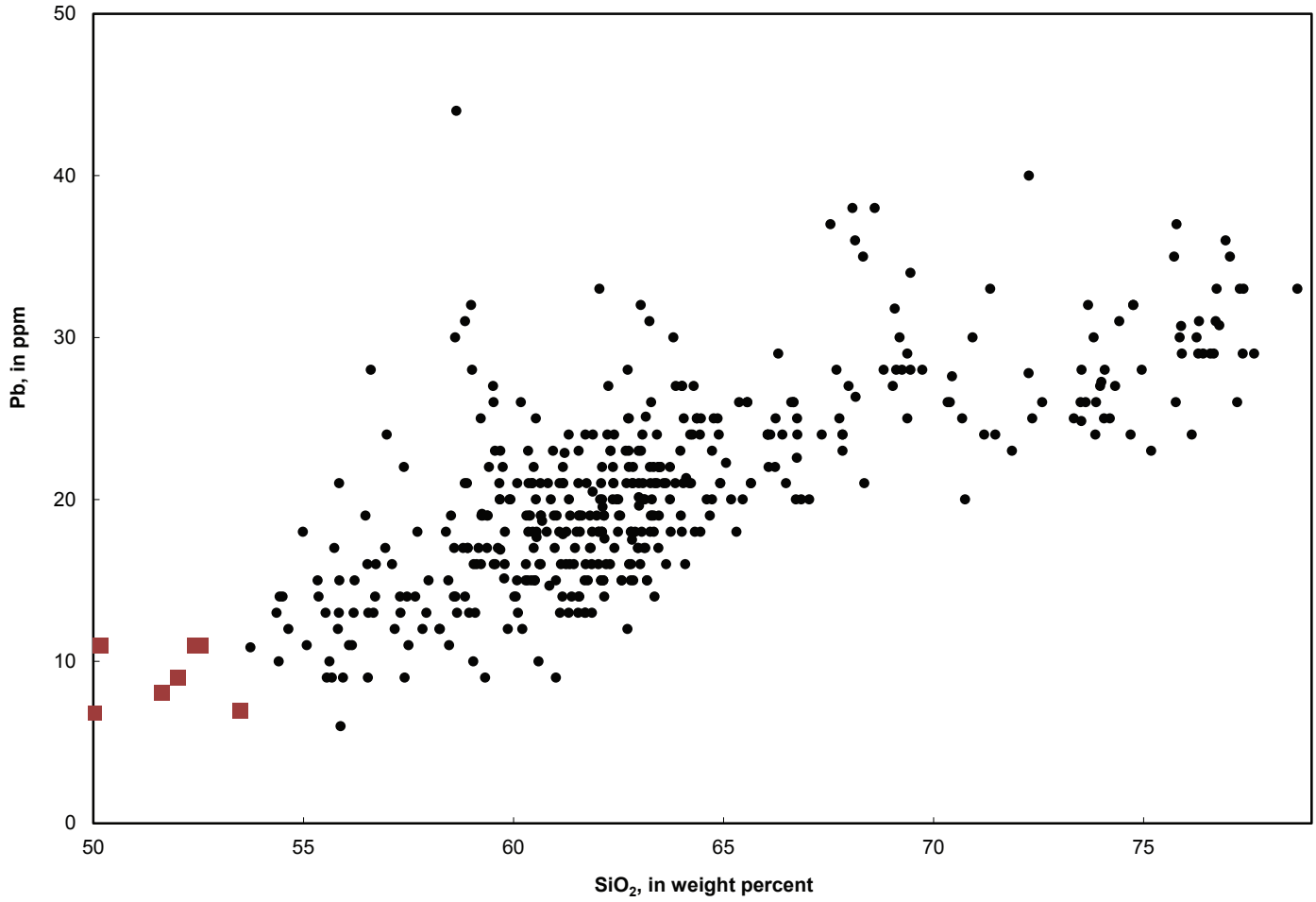

Figure S8. Variation diagram showing Pb (ppm) versus SiO2 (wt%) abundances in Bodie Hills volcanic field rocks (black dots); compositions of the most primitive samples, which represent possible parental magma compositions, are shown by tan squares.

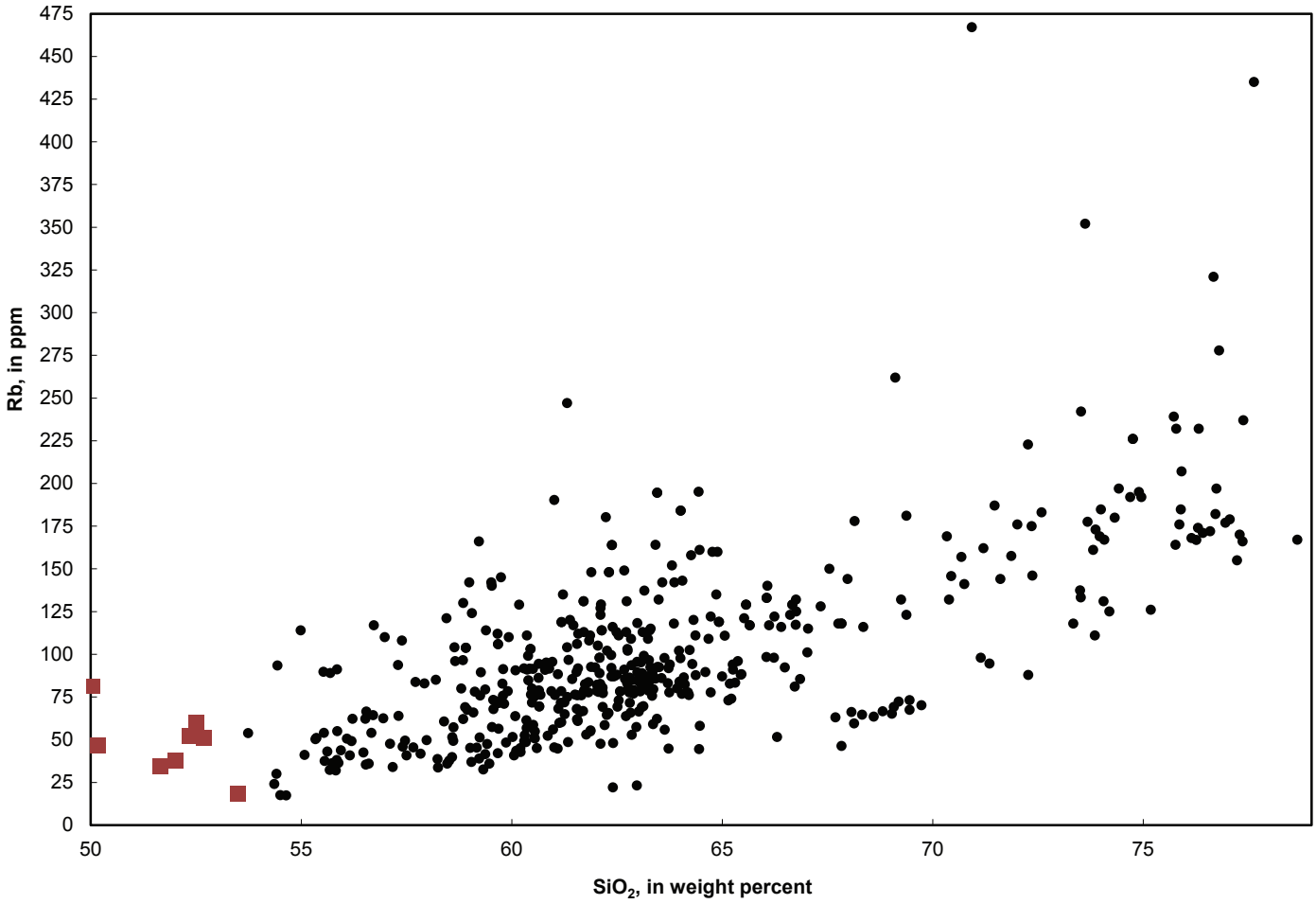

Figure S9. Variation diagram showing Rb (ppm) versus SiO2 (wt%) abundances in Bodie Hills volcanic field rocks (black dots); compositions of the most primitive samples, which represent possible parental magma compositions, are shown by tan squares.

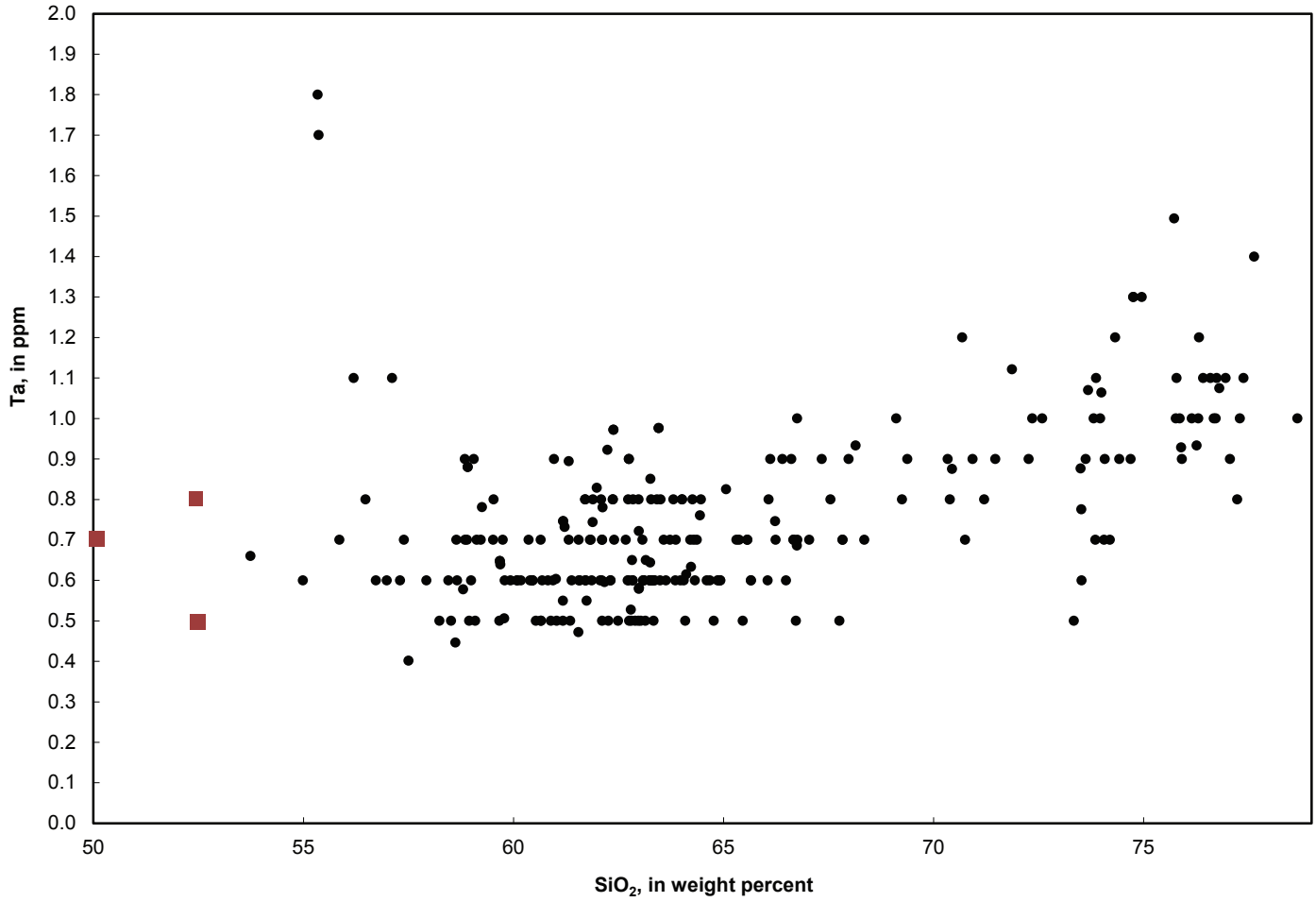

Figure S10. Variation diagram showing Ta (ppm) versus SiO2 (wt%) abundances in Bodie Hills volcanic field rocks (black dots); compositions of the most primitive samples, which represent possible parental magma compositions, are shown by tan squares.

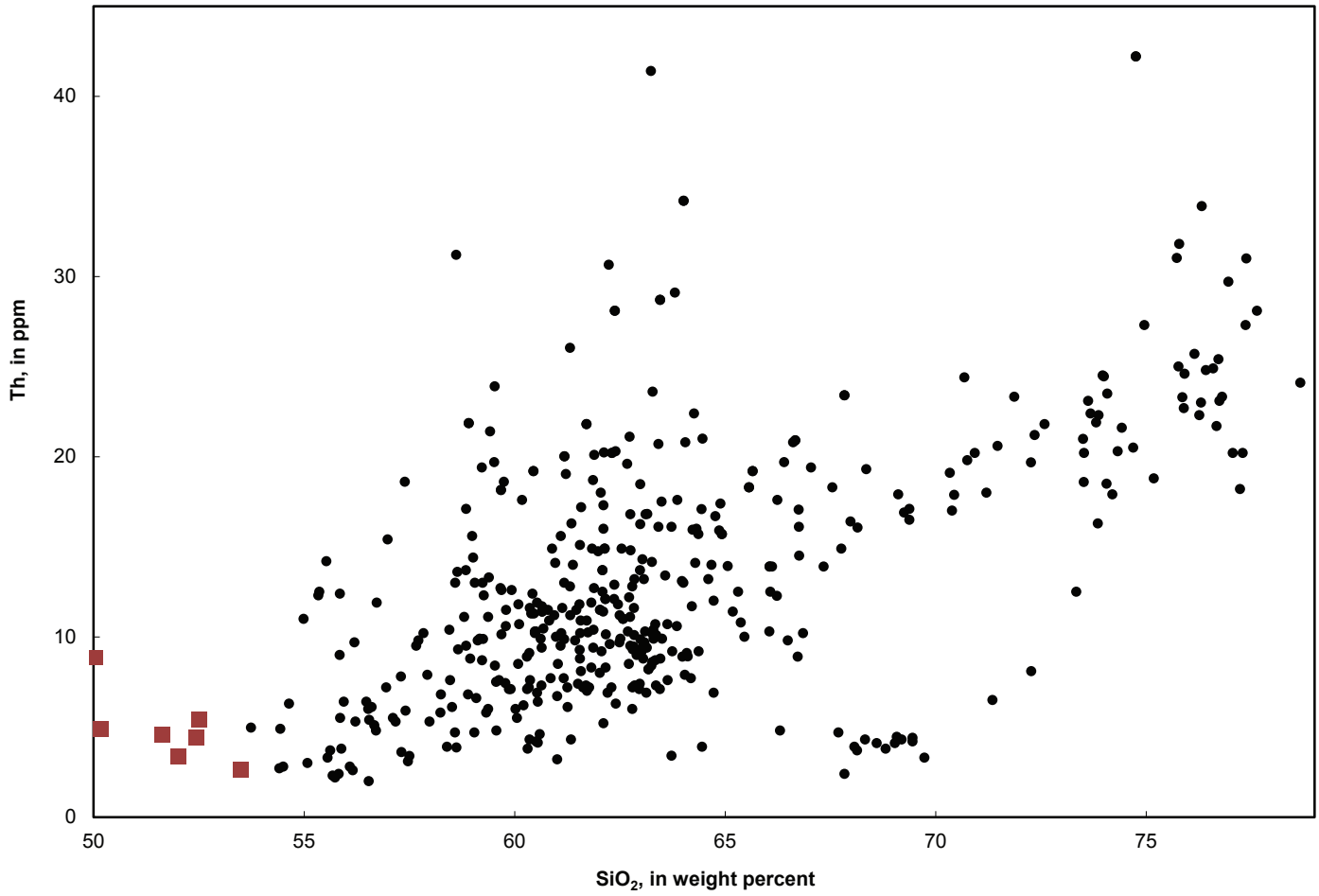

Figure S11. Variation diagram showing Th (ppm) versus SiO2 (wt%) abundances in Bodie Hills volcanic field rocks (black dots); compositions of the most primitive samples, which represent possible parental magma compositions, are shown by tan squares.

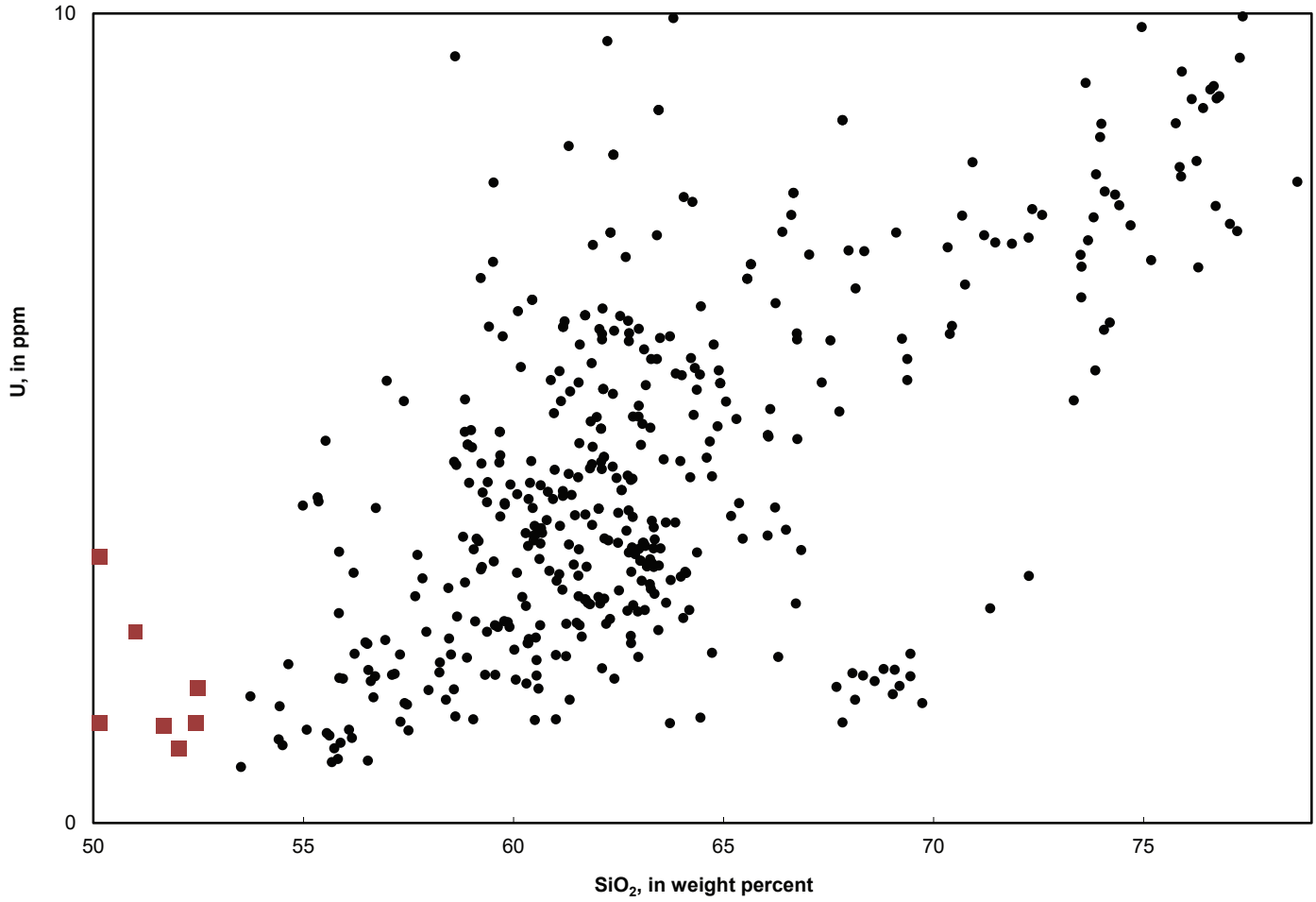

Figure S12. Variation diagram showing U (ppm) versus SiO2 (wt%) abundances in Bodie Hills volcanic field rocks (black dots); compositions of the most primitive samples, which represent possible parental magma compositions, are shown by tan squares.

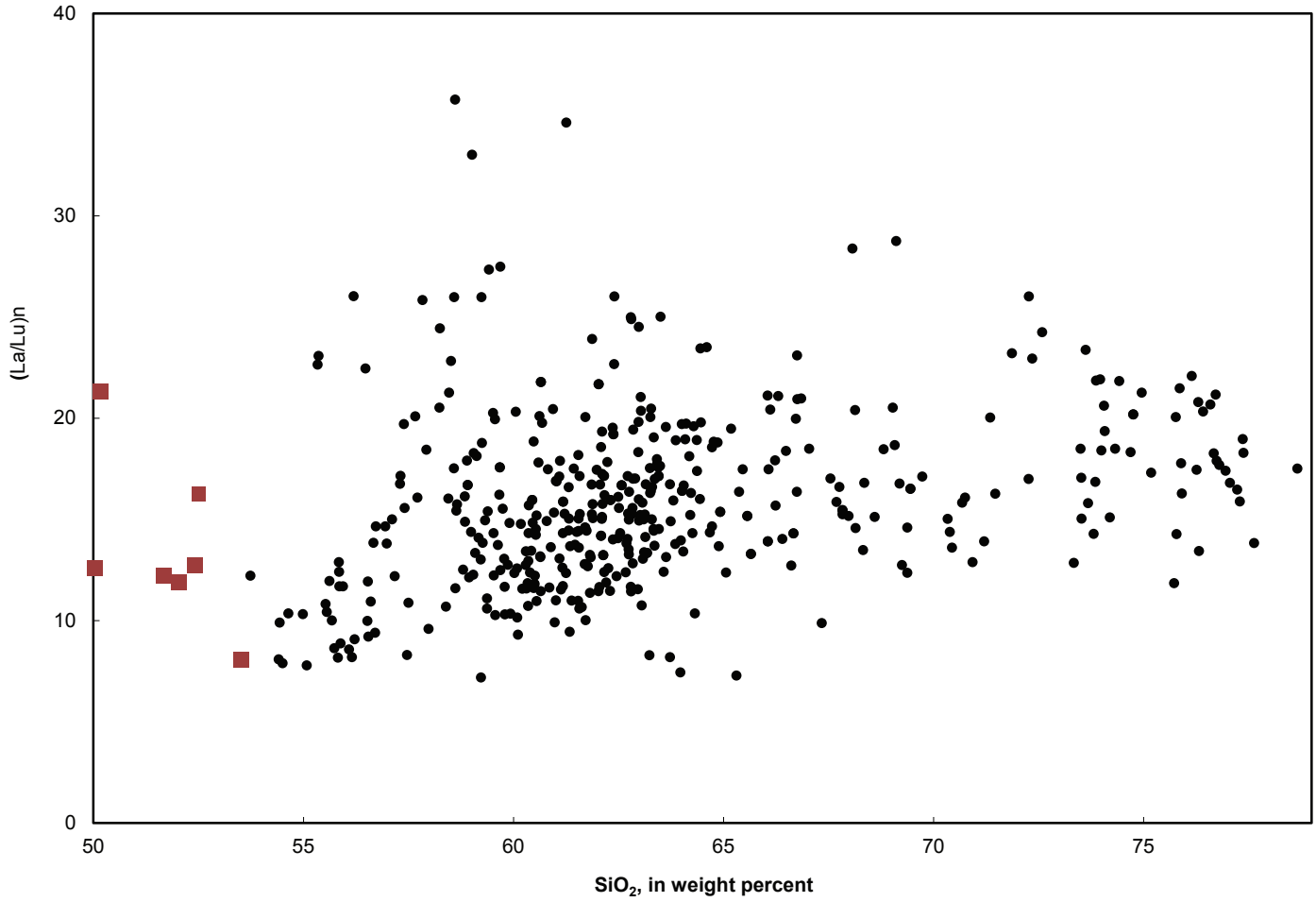

Figure S13. Variation diagram showing $(La/Lu)_N$ versus SiO2 (wt%) abundances in Bodie Hills volcanic field rocks (black dots); compositions of the most primitive samples, which represent possible parental magma compositions, are shown by tan squares.

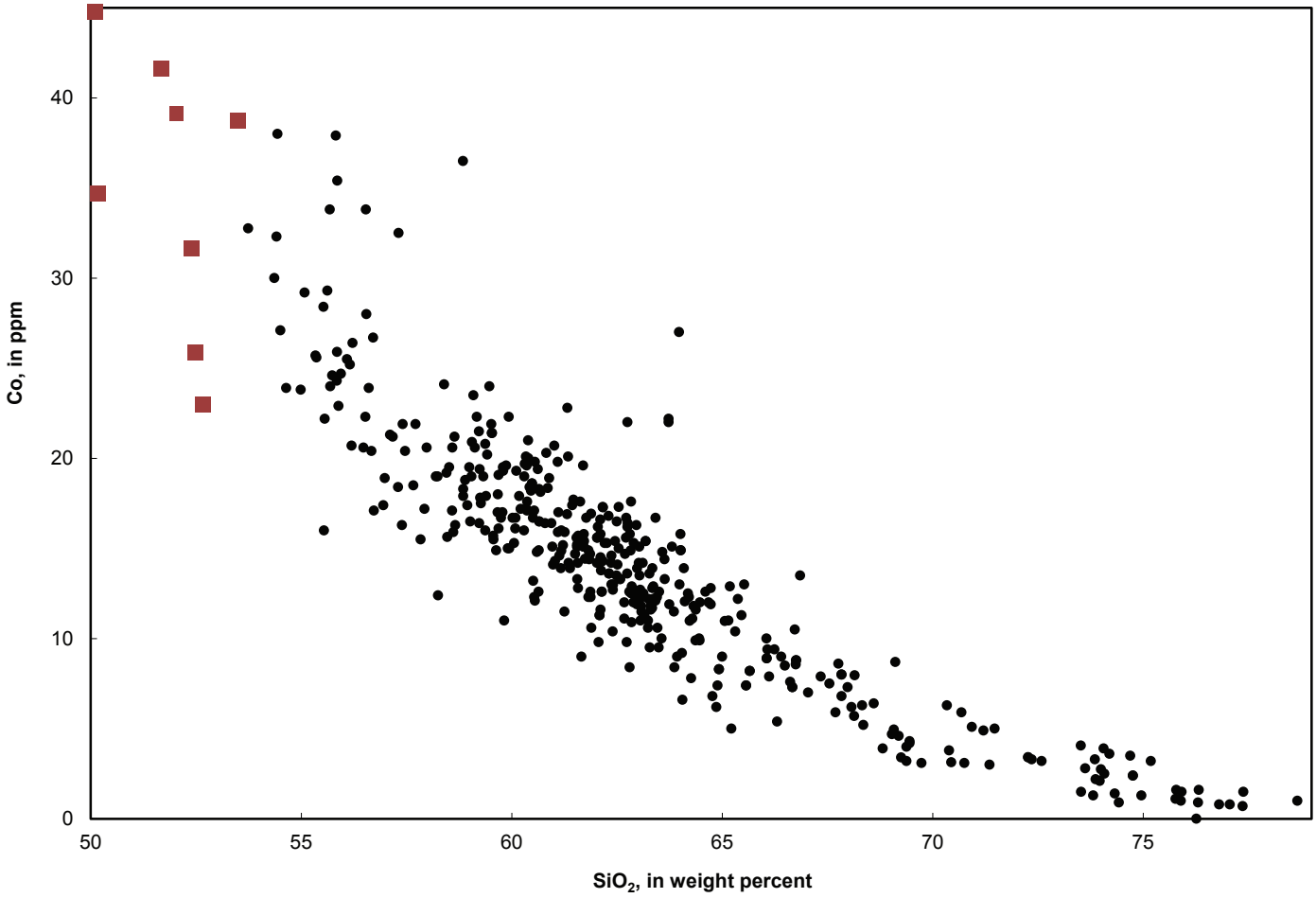

Figure S14. Variation diagram showing Co (ppm) versus SiO2 (wt%) abundances in Bodie Hills volcanic field rocks (black dots); compositions of the most primitive samples, which represent possible parental magma compositions, are shown by tan squares.

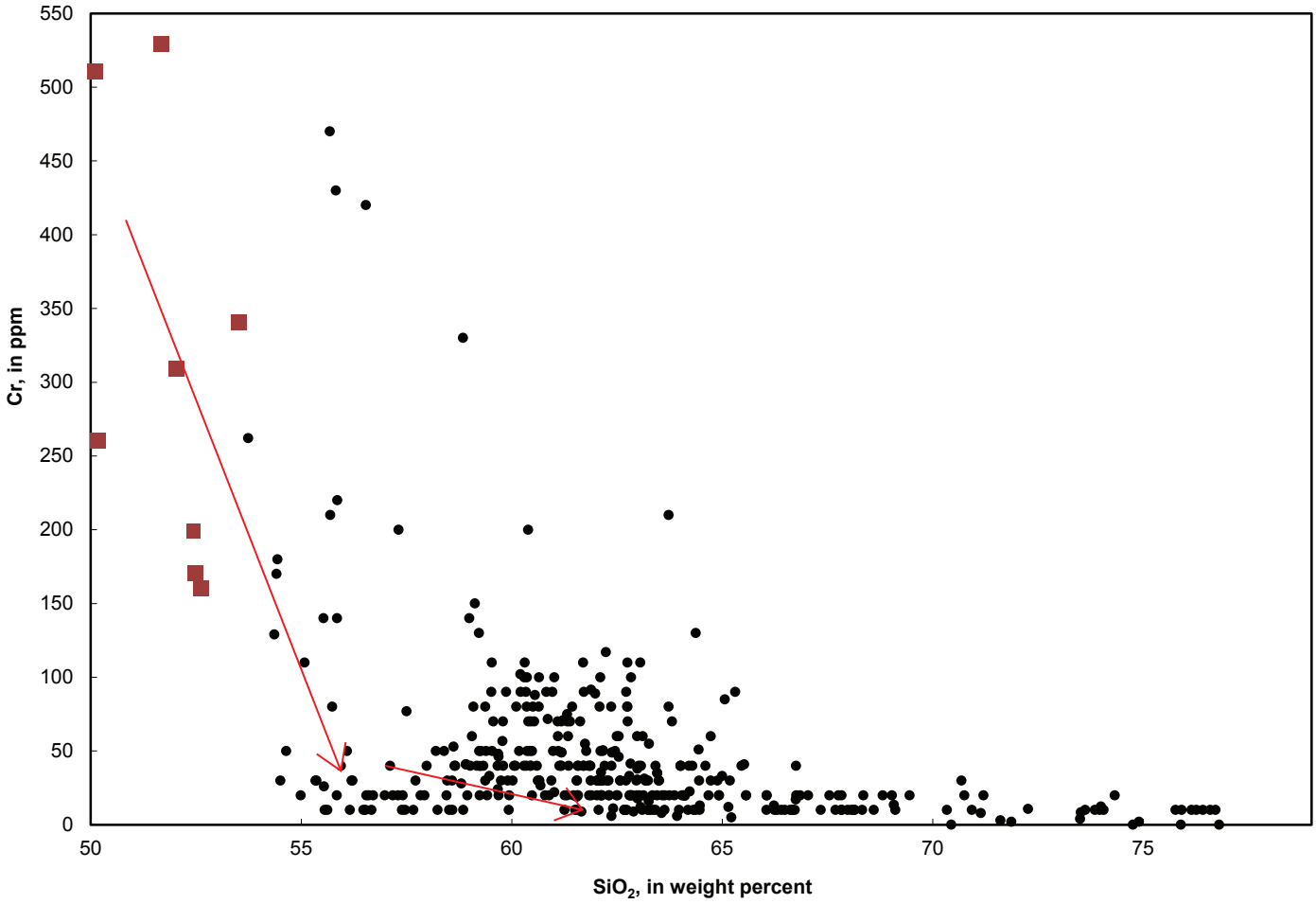

Figure S15. Variation diagram showing Cr (ppm) versus SiO2 (wt%) abundances in Bodie Hills volcanic field rocks (black dots); compositions of the most primitive samples, which represent possible parental magma compositions, are shown by tan squares. Red lines define distinct fractionation trends that likely contributed to the observed compositonal variation.

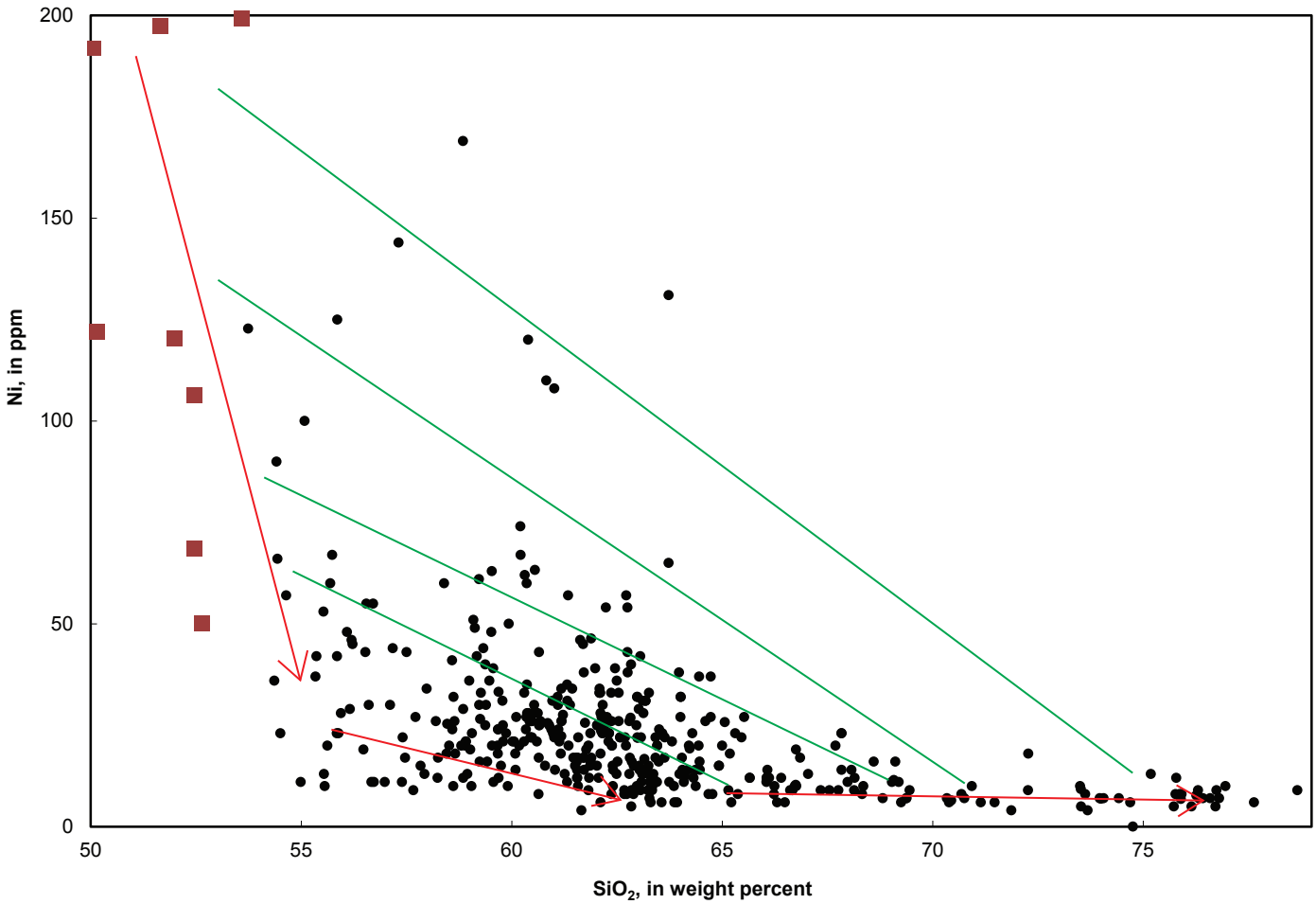

Figure S16. Variation diagram showing Ni (ppm) versus SiO2 (wt%) abundances in Bodie Hills volcanic field rocks (black dots); compositions of the most primitive samples, which represent possible parental magma compositions, are shown by tan squares. Red lines define distinct fractionation trends and green lines depict potential mixing arrays that likely both contributed to the observed compositonal variation.

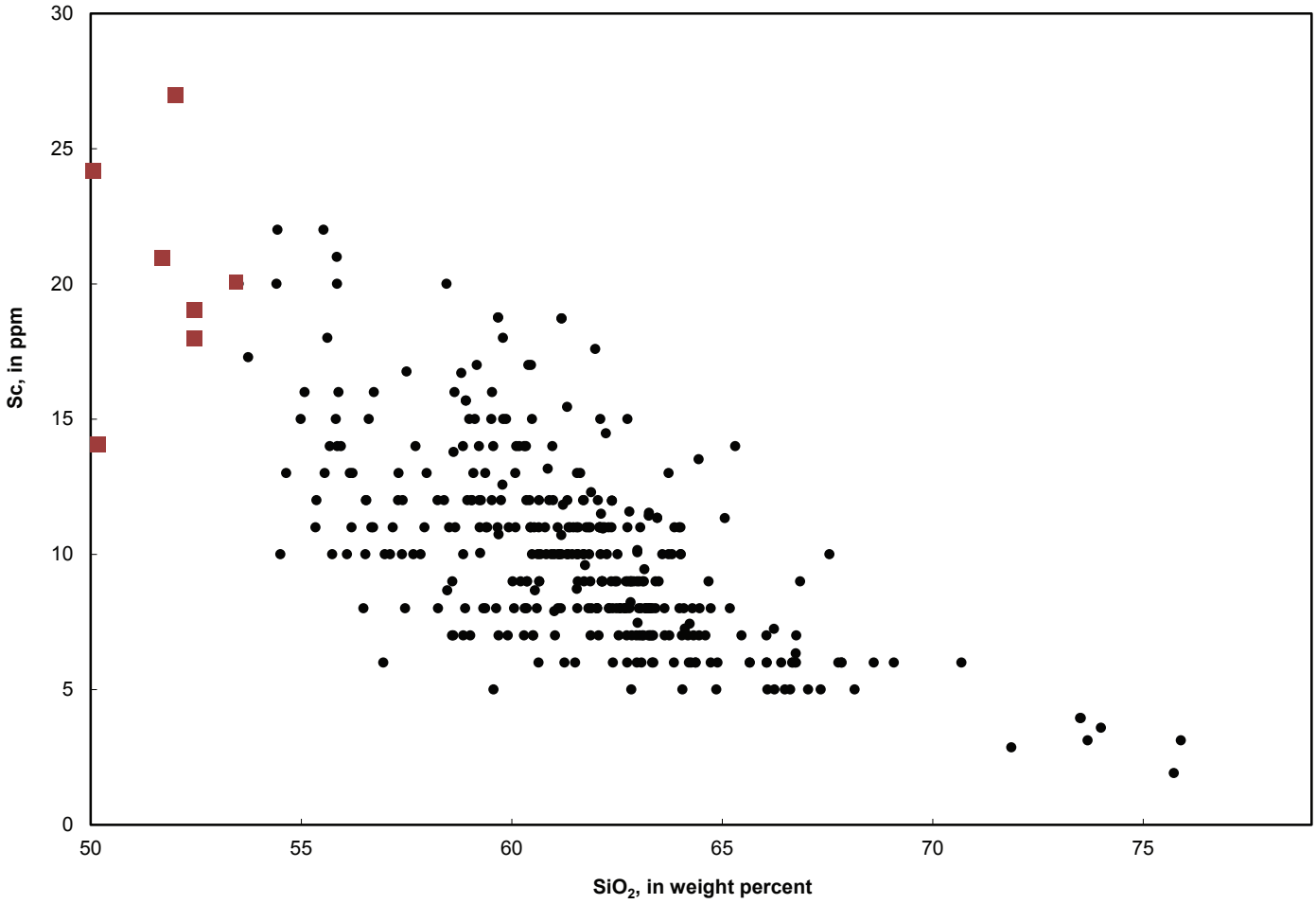

Figure S17. Variation diagram showing Sc (ppm) versus SiO2 (wt%) abundances in Bodie Hills volcanic field rocks (black dots); compositions of the most primitive samples, which represent possible parental magma compositions, are shown by tan squares.

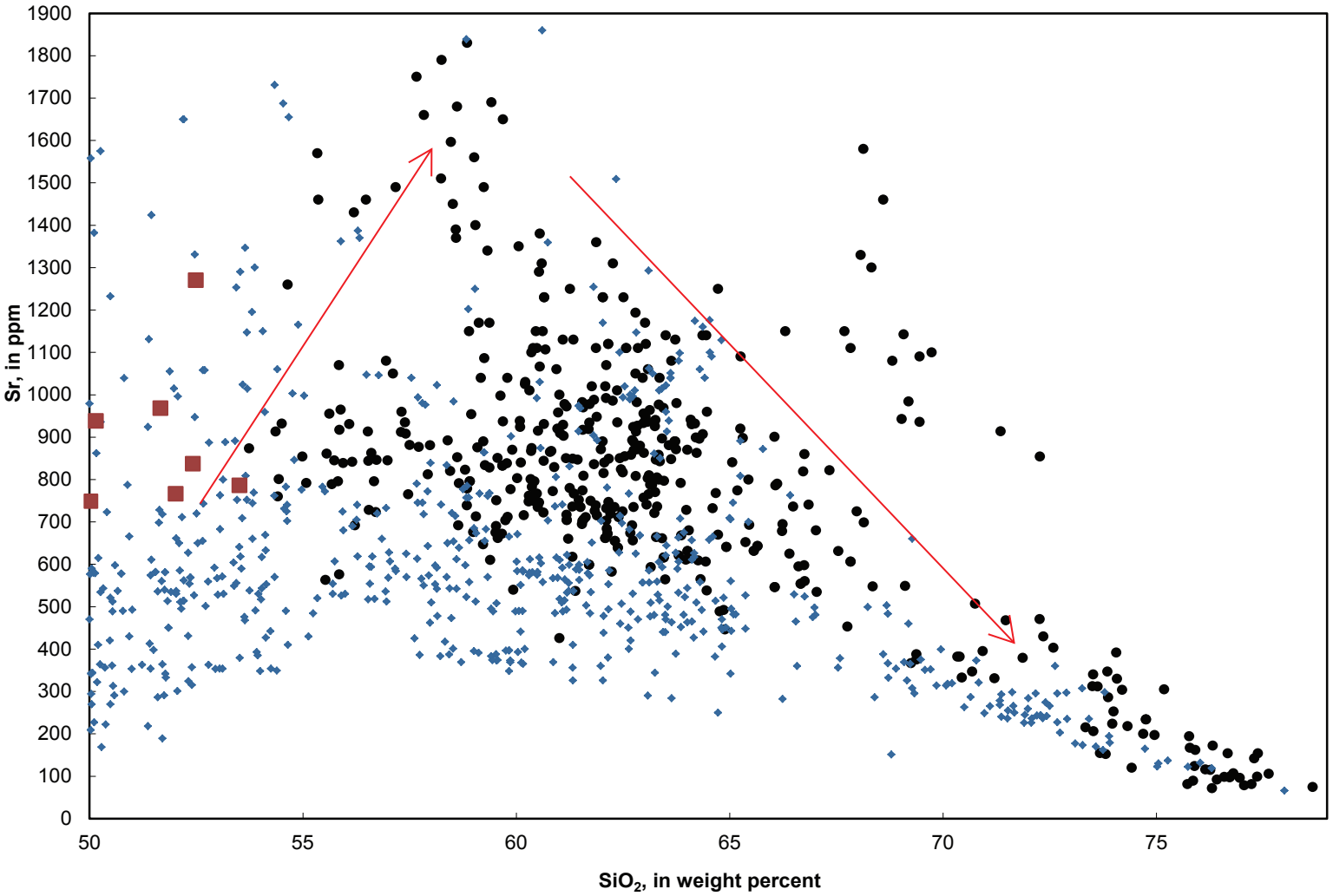

Figure S18. Variation diagram showing Sr (ppm) versus SiO2 (wt%) abundances in Bodie Hills volcanic field rocks (black dots); compositions of the most primitive samples, which represent possible parental magma compositions, are shown by tan squares. Blue diamonds represent compositions of the modern High Cascades arc rocks (data from GEOROC, 2010). Red lines define distinct fractionation trends that likely contributed to the observed compositonal variation.

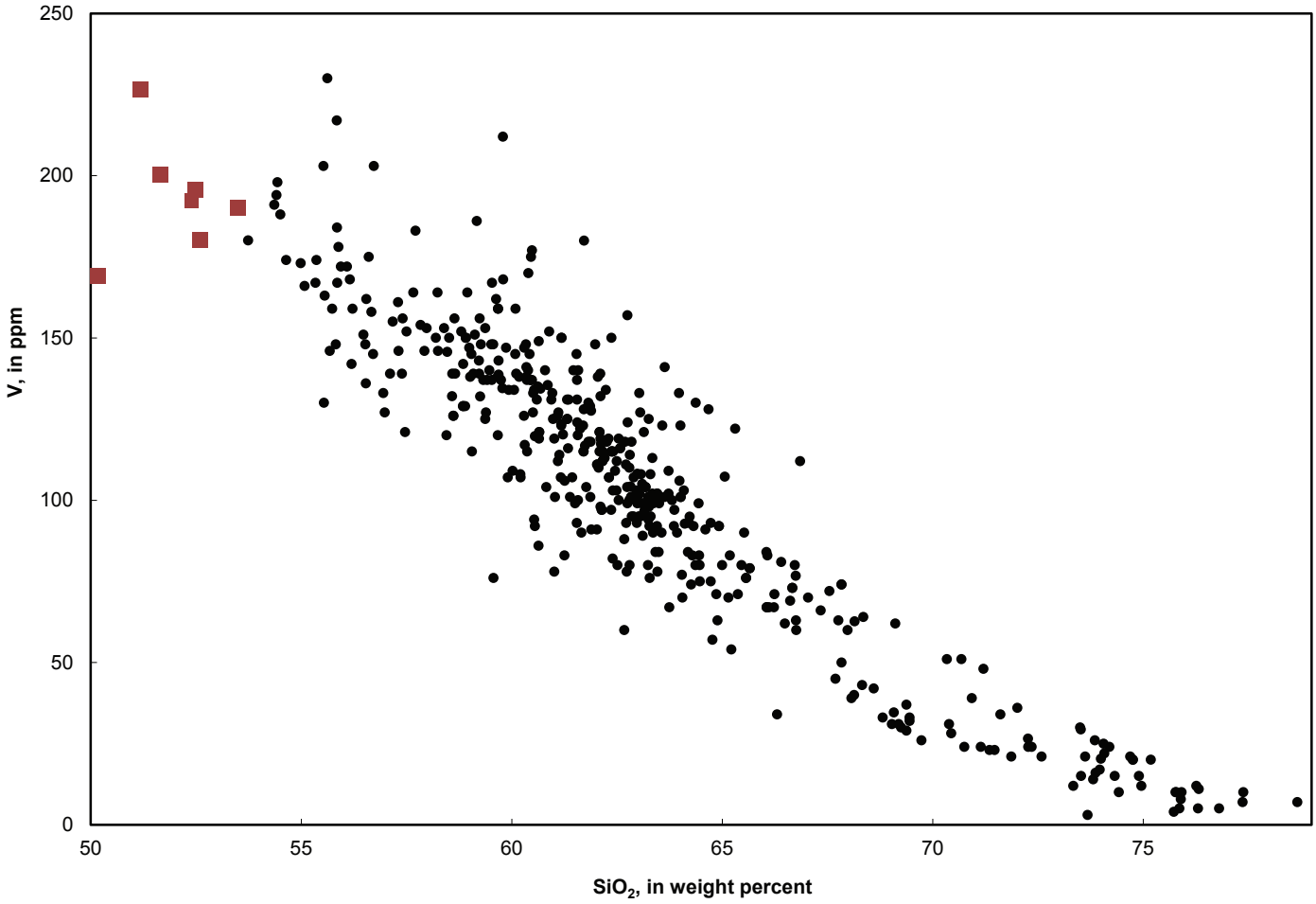

Figure S19. Variation diagram showing V (ppm) versus SiO2 (wt%) abundances in Bodie Hills volcanic field rocks (black dots); compositions of the most primitive samples, which represent possible parental magma compositions, are shown by tan squares.

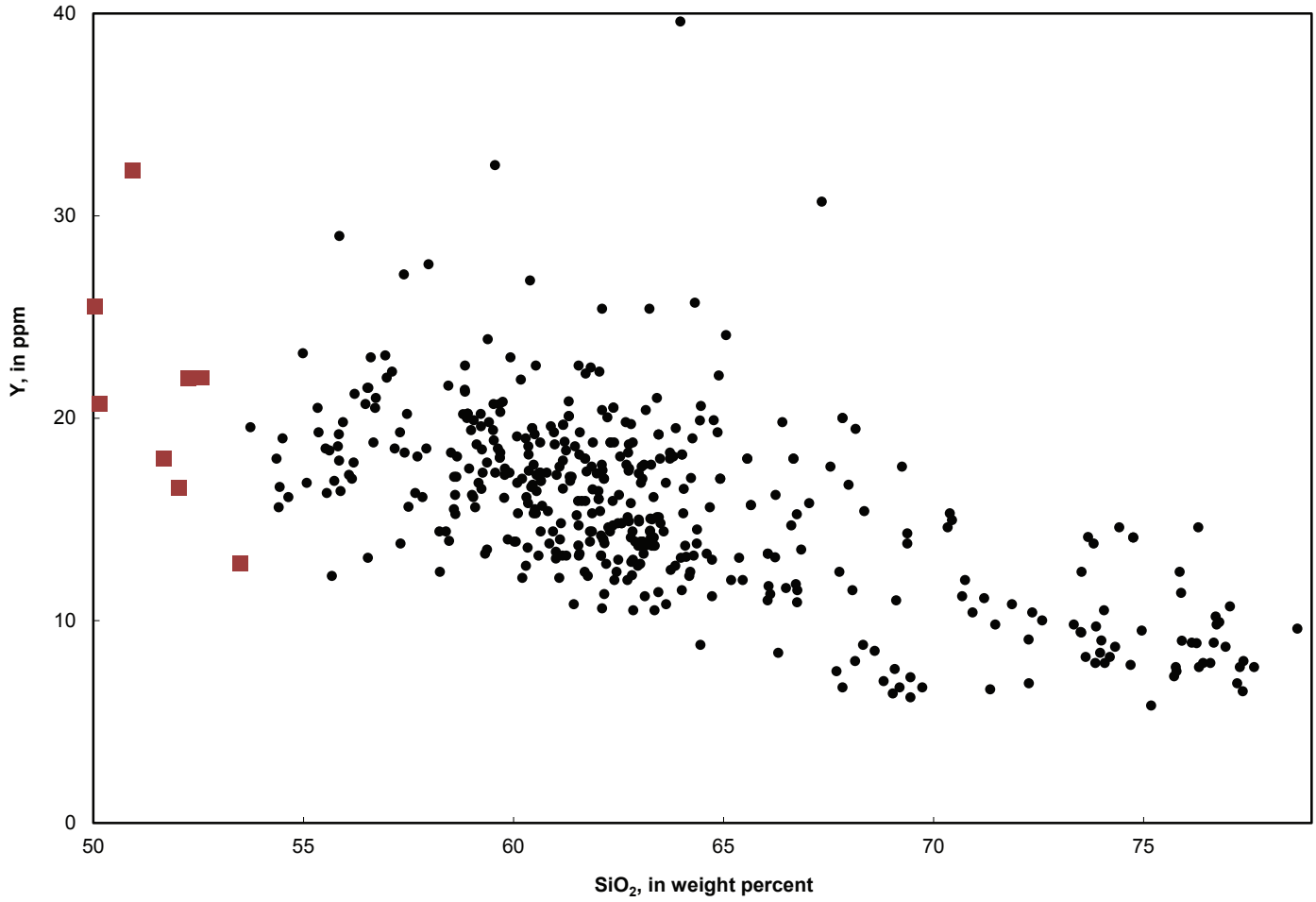

Figure S20. Variation diagram showing Y (ppm) versus SiO2 (wt%) abundances in Bodie Hills volcanic field rocks (black dots); compositions of the most primitive samples, which represent possible parental magma compositions, are shown by tan squares.

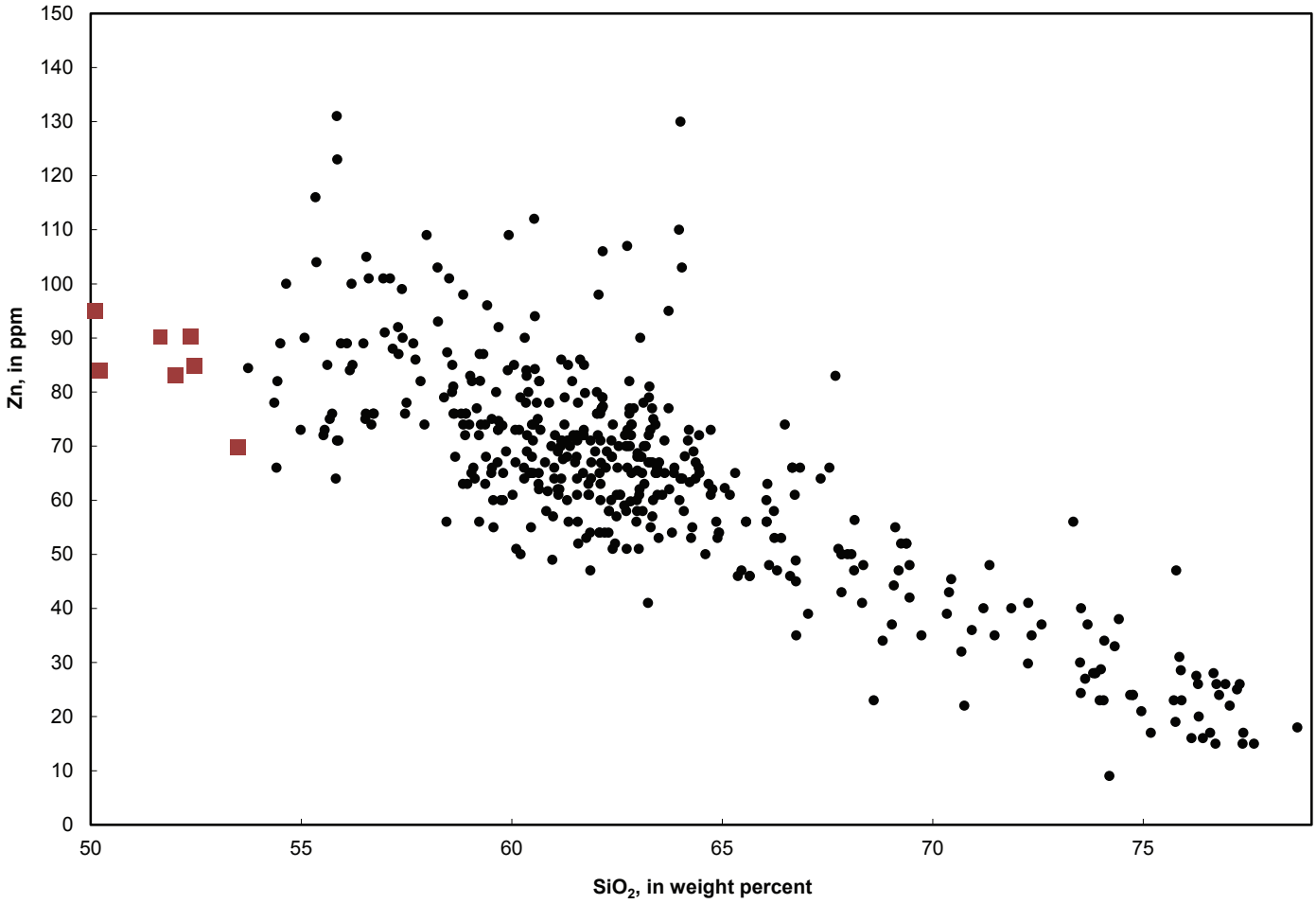

Figure S21. Variation diagram showing Zn (ppm) versus SiO2 (wt%) abundances in Bodie Hills volcanic field rocks (black dots); compositions of the most primitive samples, which represent possible parental magma compositions, are shown by tan squares.

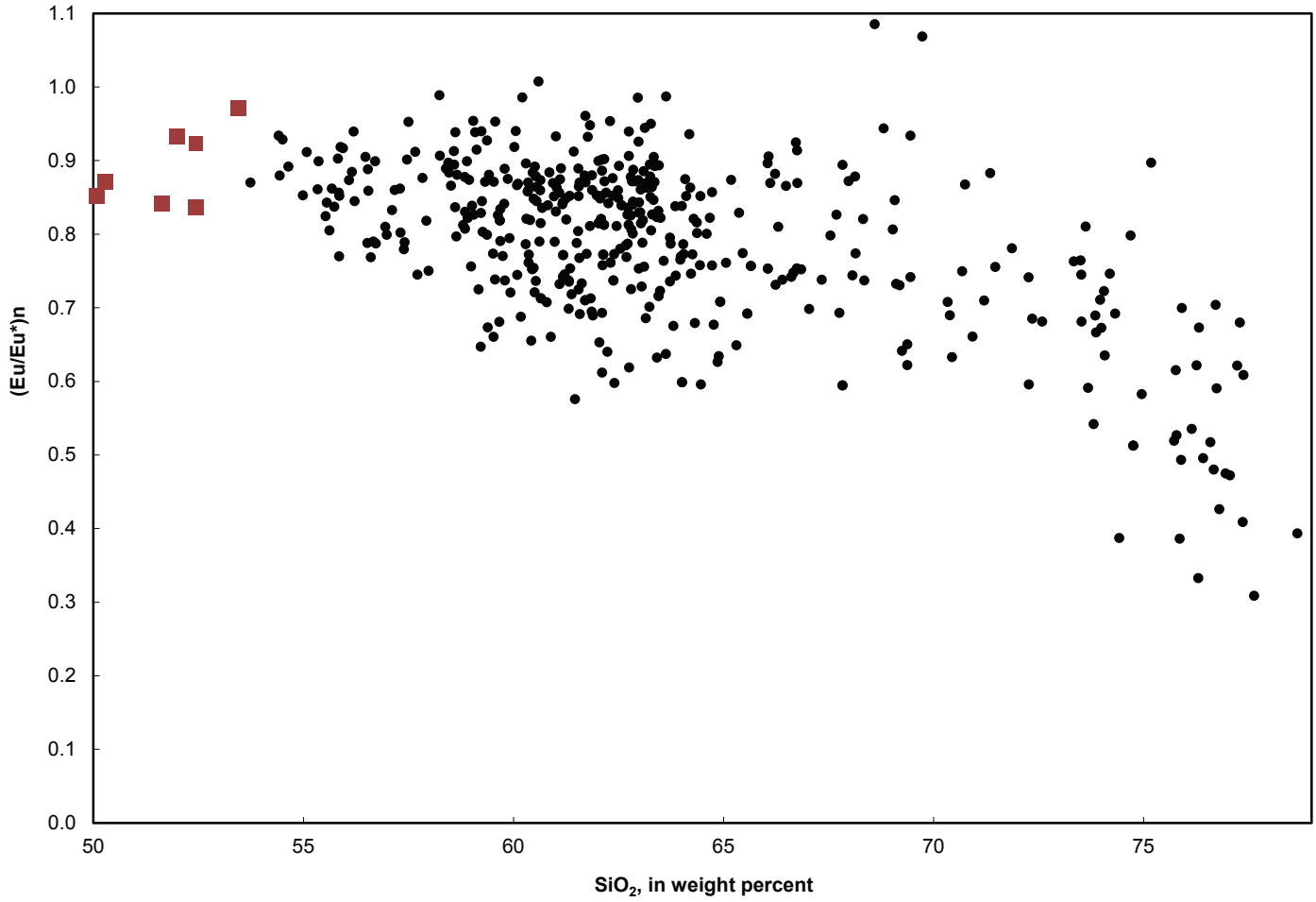

Figure S22. Variation diagram showing Eu/Eu* versus SiO2 (wt%) abundances in Bodie Hills volcanic field rocks (black dots); compositions of the most primitive samples, which represent possible parental magma compositions, are shown by tan squares.

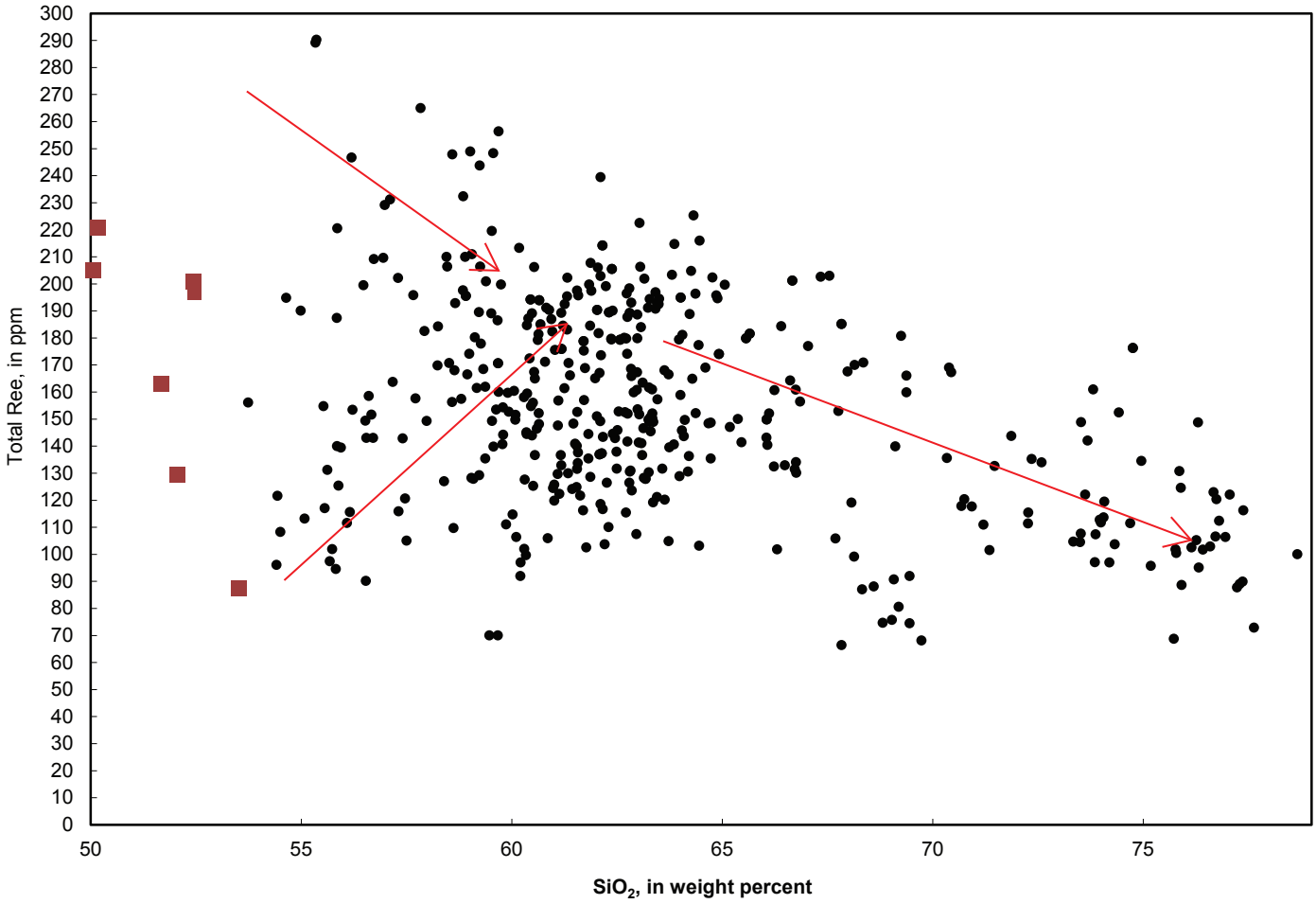

Figure S23. Variation diagram showing total REE (ppm) versus SiO2 (wt%) abundances in Bodie Hills volcanic field rocks (black dots); compositions of the most primitive samples, which represent possible parental magma compositions, are shown by tan squares. Red lines define distinct fractionation trends that likely contributed to the observed compositonal variation.

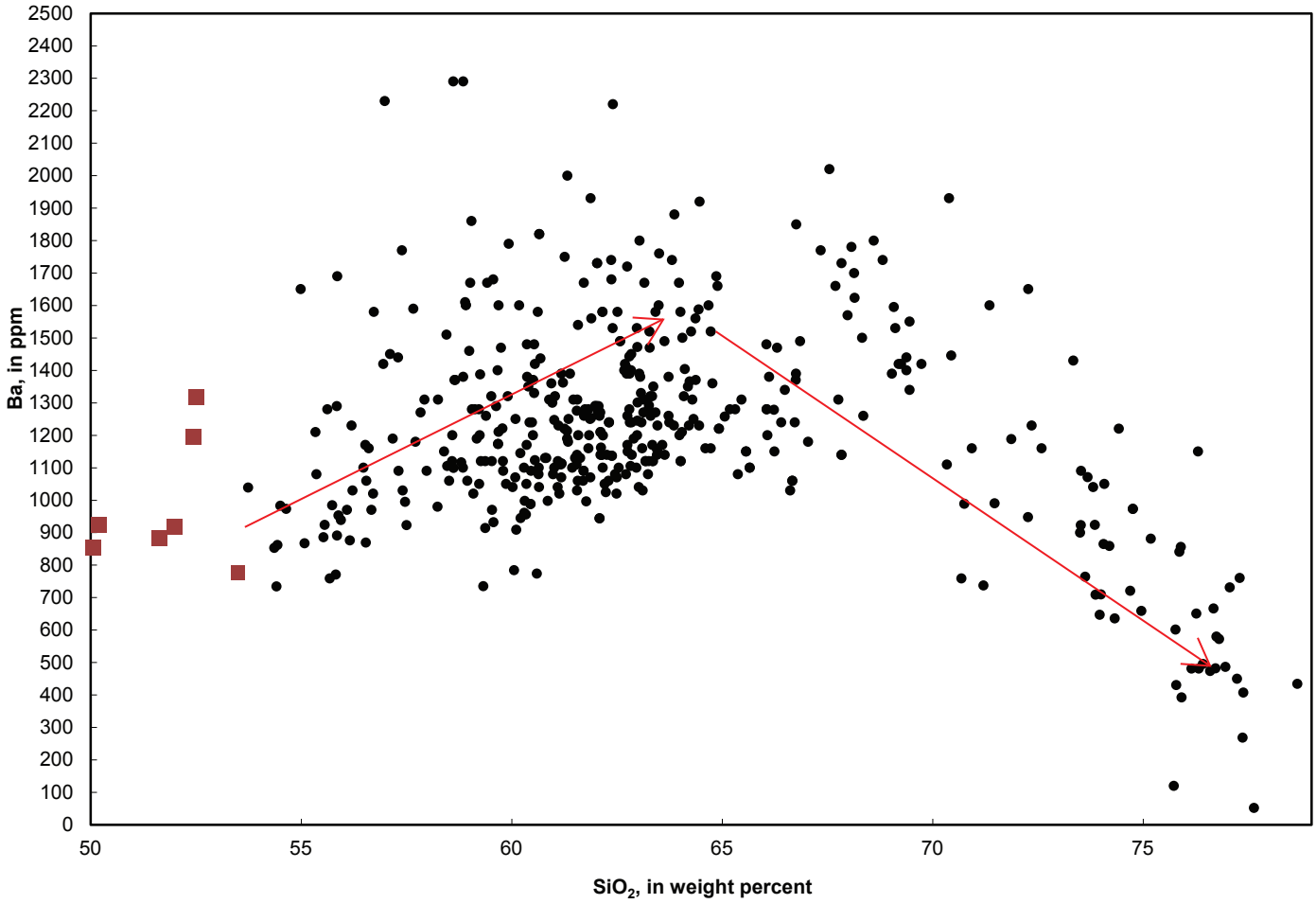

Figure S24. Variation diagram showing Ba (ppm) versus SiO2 (wt%) abundances in Bodie Hills volcanic field rocks (black dots); compositions of the most primitive samples, which represent possible parental magma compositions, are shown by tan squares. Red lines define distinct fractionation trends that likely contributed to the observed compositonal variation.

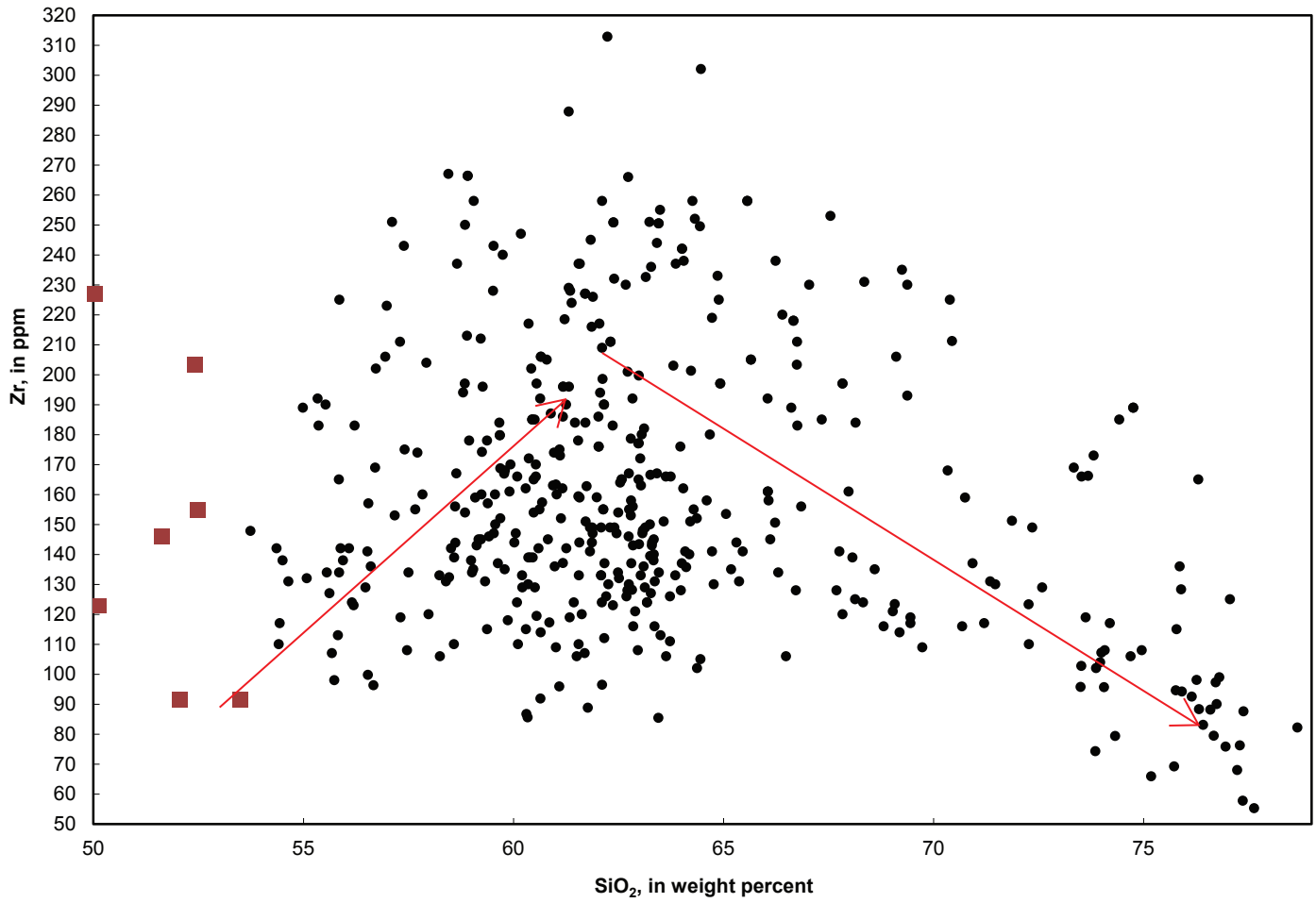

Figure S25. Variation diagram showing Zr (ppm) versus SiO2 (wt%) abundances in Bodie Hills volcanic field rocks (black dots); compositions of the most primitive samples, which represent possible parental magma compositions, are shown by tan squares. Red lines define distinct fractionation trends that likely contributed to the observed compositonal variation.

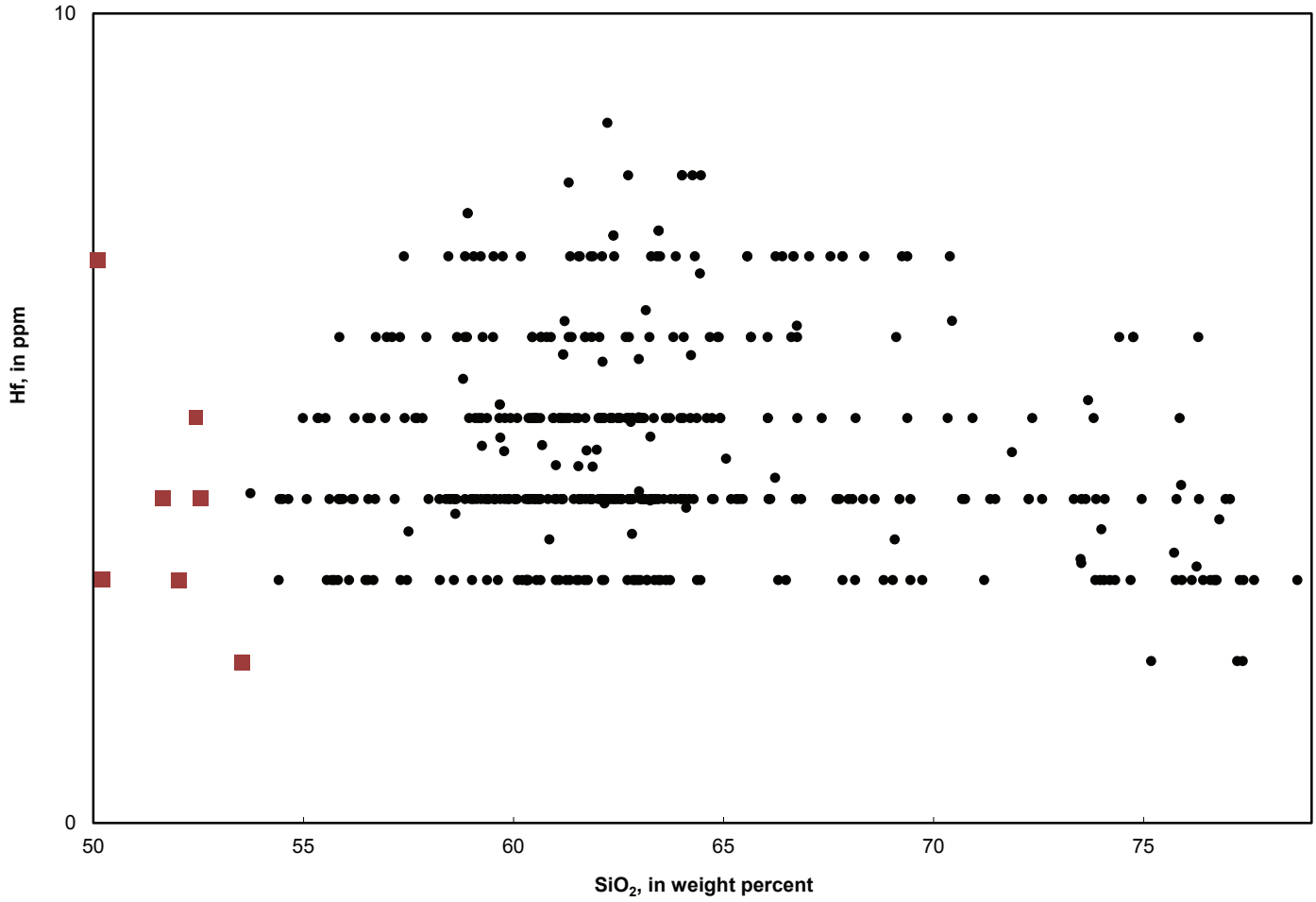

Figure S26. Variation diagram showing Hf (ppm) versus SiO2 (wt%) abundances in Bodie Hills volcanic field rocks (black dots); compositions of the most primitive samples, which represent possible parental magma compositions, are shown by tan squares.

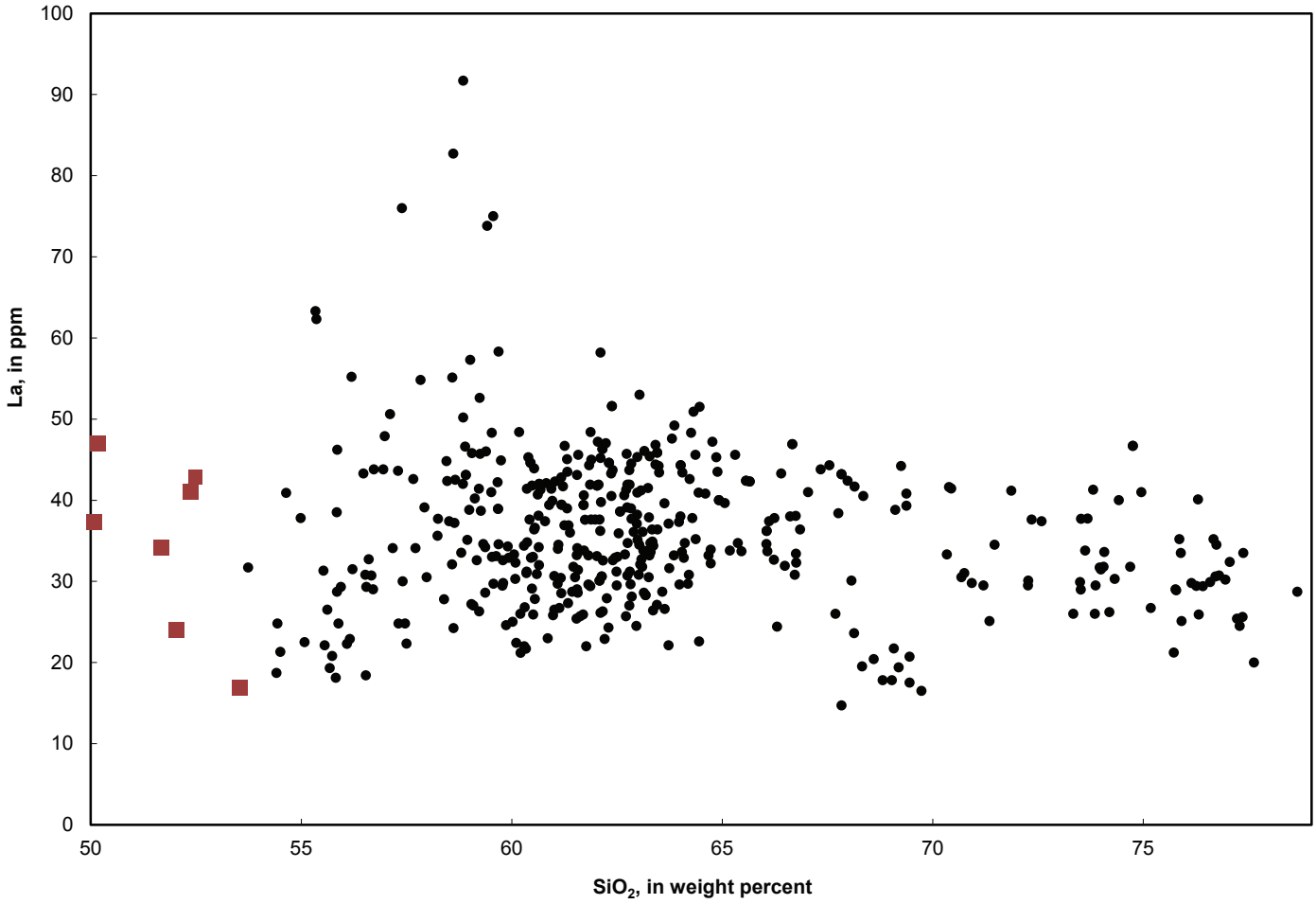

Figure S27. Variation diagram showing La (ppm) versus SiO2 (wt%) abundances in Bodie Hills volcanic field rocks (black dots); compositions of the most primitive samples, which represent possible parental magma compositions, are shown by tan squares.

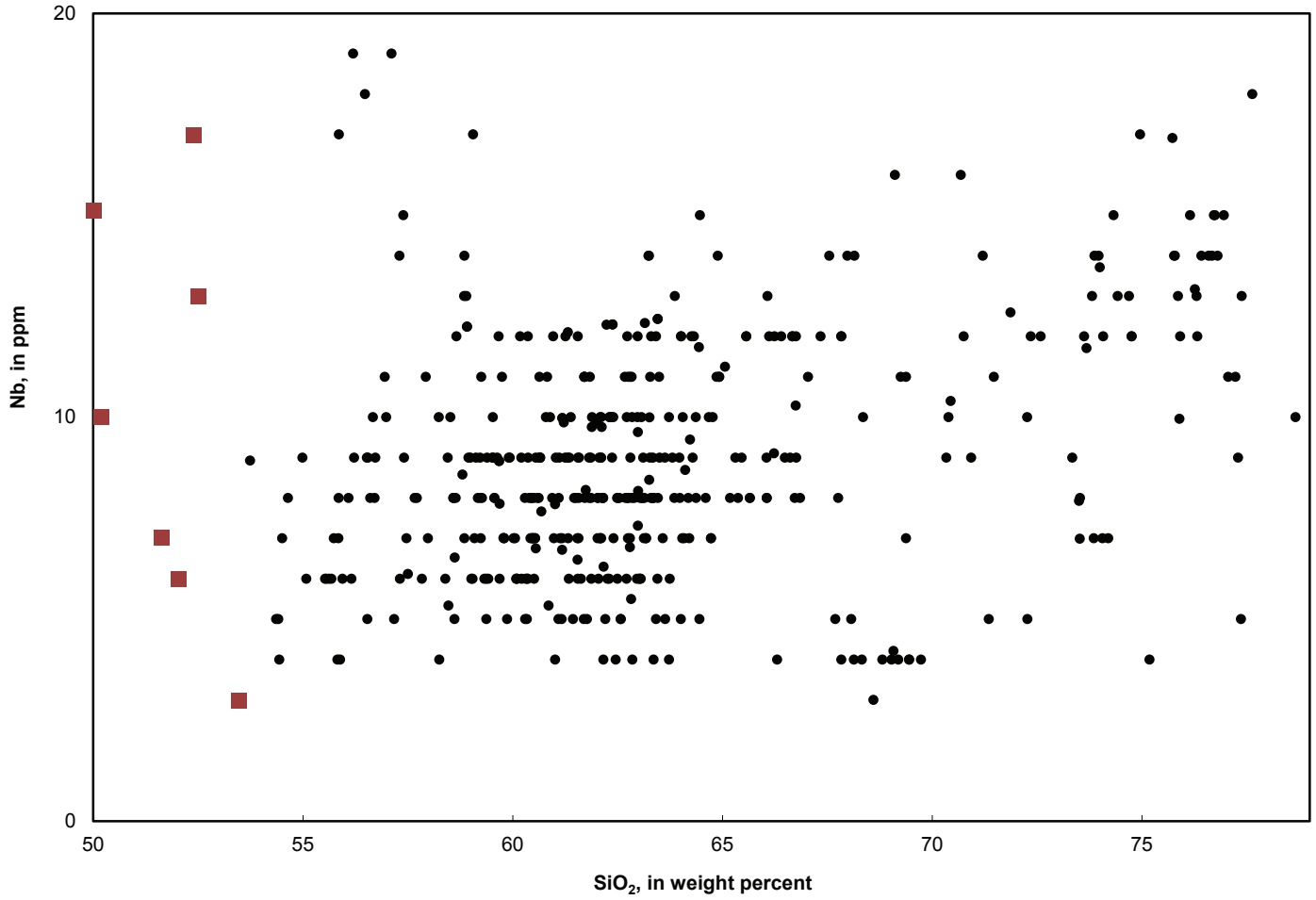

Figure S28. Variation diagram showing Nb (ppm) versus SiO2 (wt%) abundances in Bodie Hills volcanic field rocks (black dots); compositions of the most primitive samples, which represent possible parental magma compositions, are shown by tan squares.

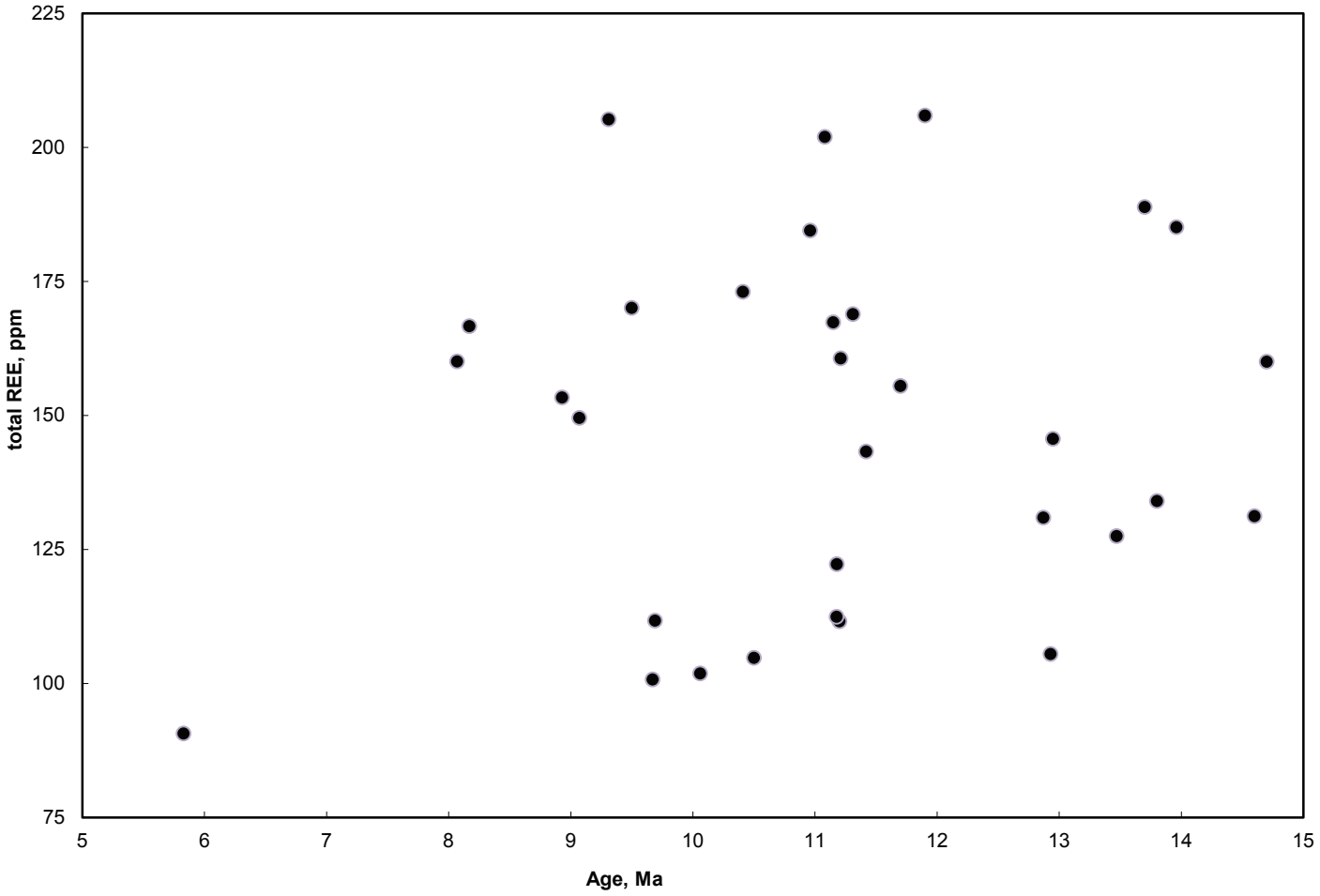

Figure S29. Variation diagram showing average total REE content (ppm) versus age for map units of the Bodie Hills volcanic field (black dots).

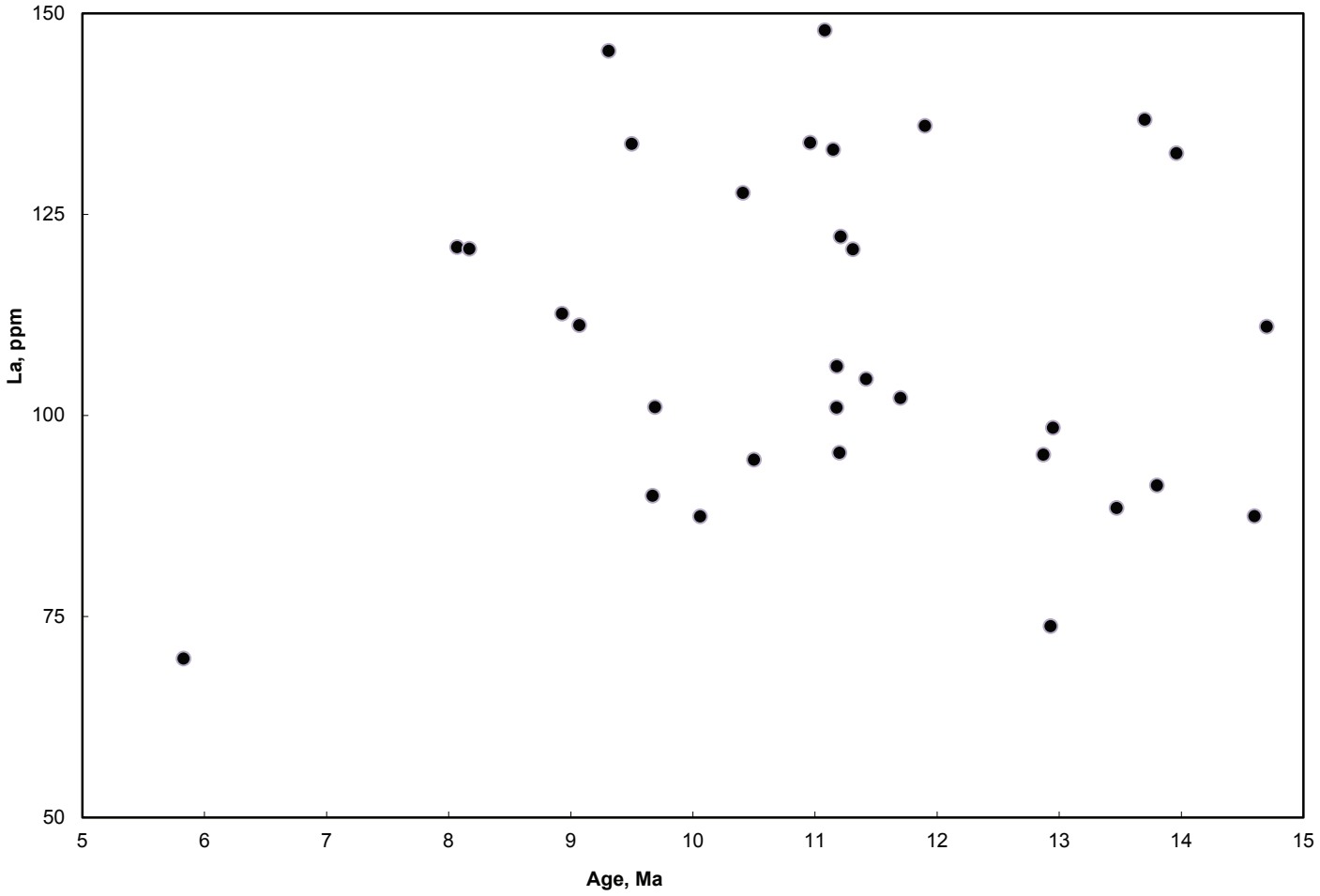

Figure S30. Variation diagram showing average La content (ppm) versus age for map units of the Bodie Hills volcanic field (black dots).

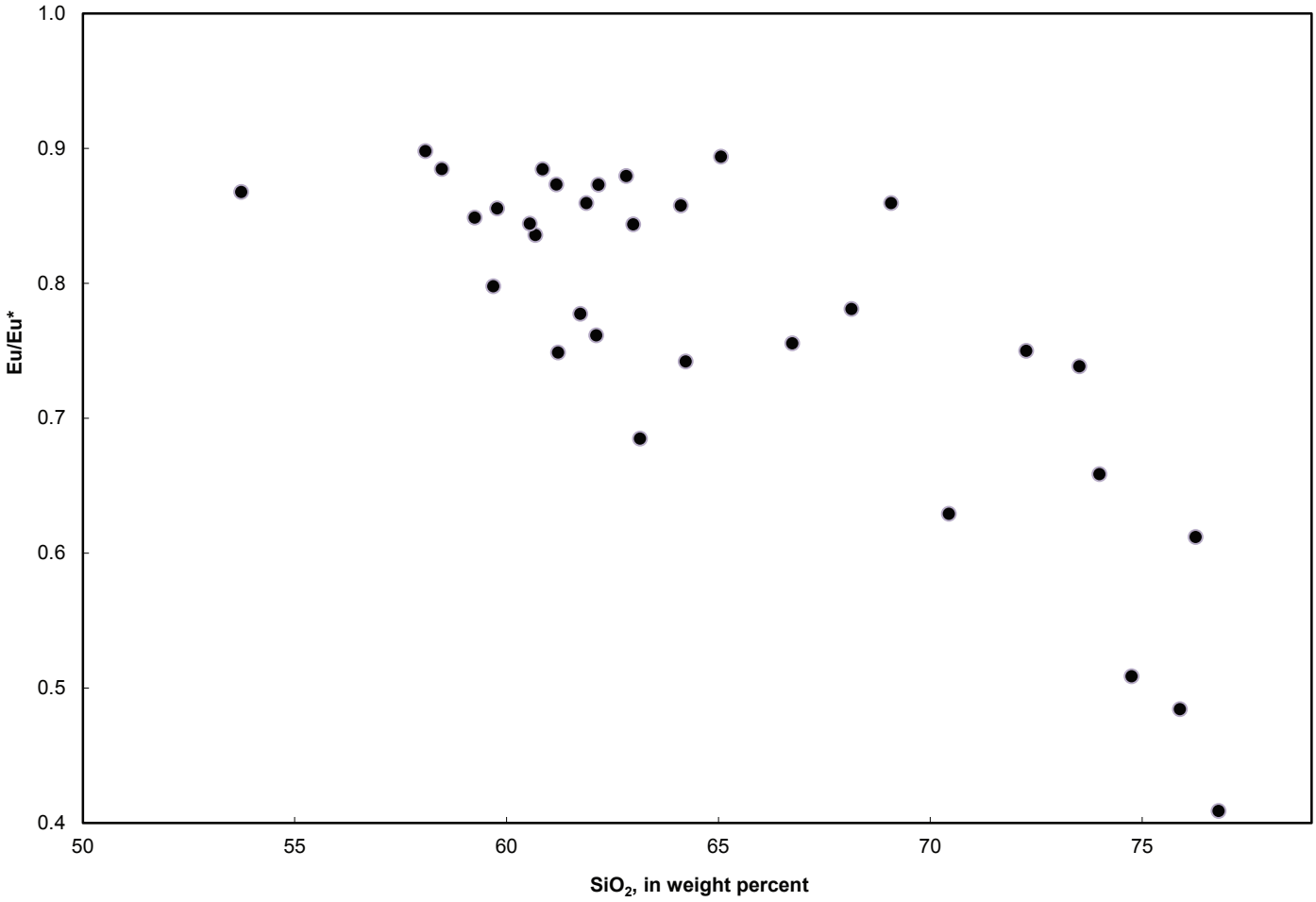

Figure S31. Variation diagram showing average Eu/Eu* versus SiO2 abundance for map units of the Bodie Hills volcanic field (black dots).

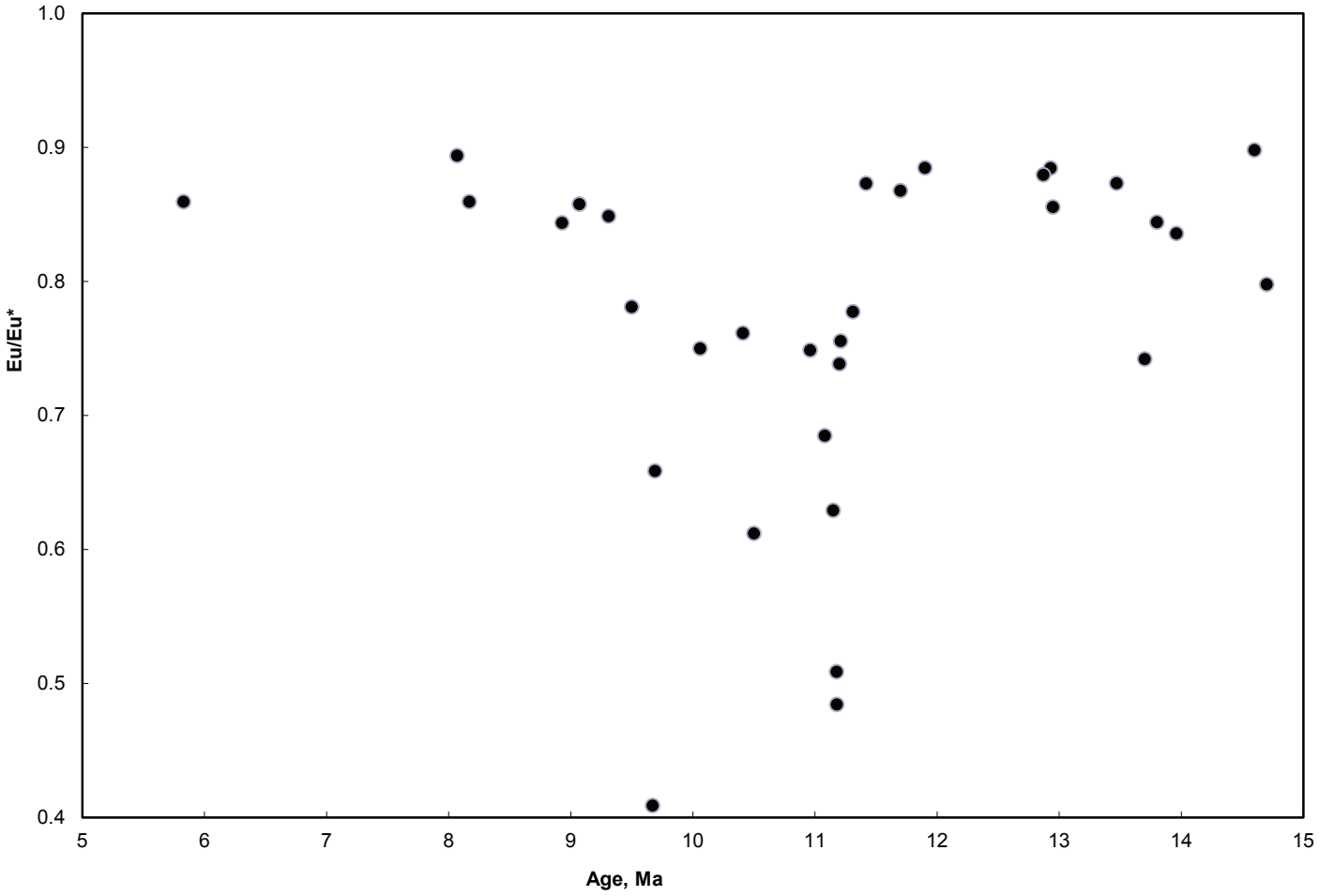

Figure S32. Variation diagram showing average Eu/Eu* versus age for map units of the Bodie Hills volcanic field (black dots).

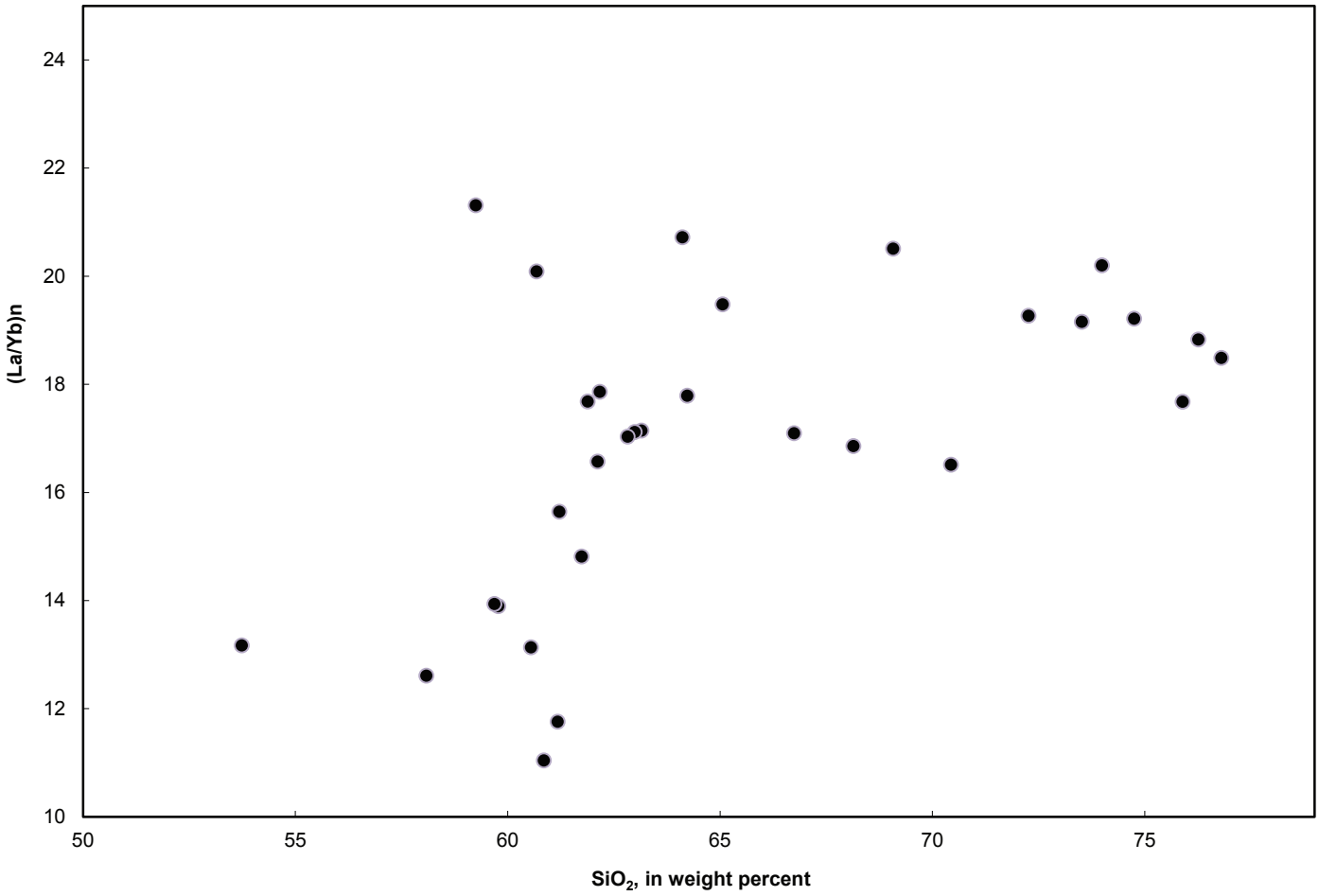

Figure S33. Variation diagram showing average $(La/Yb)_N$ versus SiO2 abundance for map units of the Bodie Hills volcanic field (black dots).

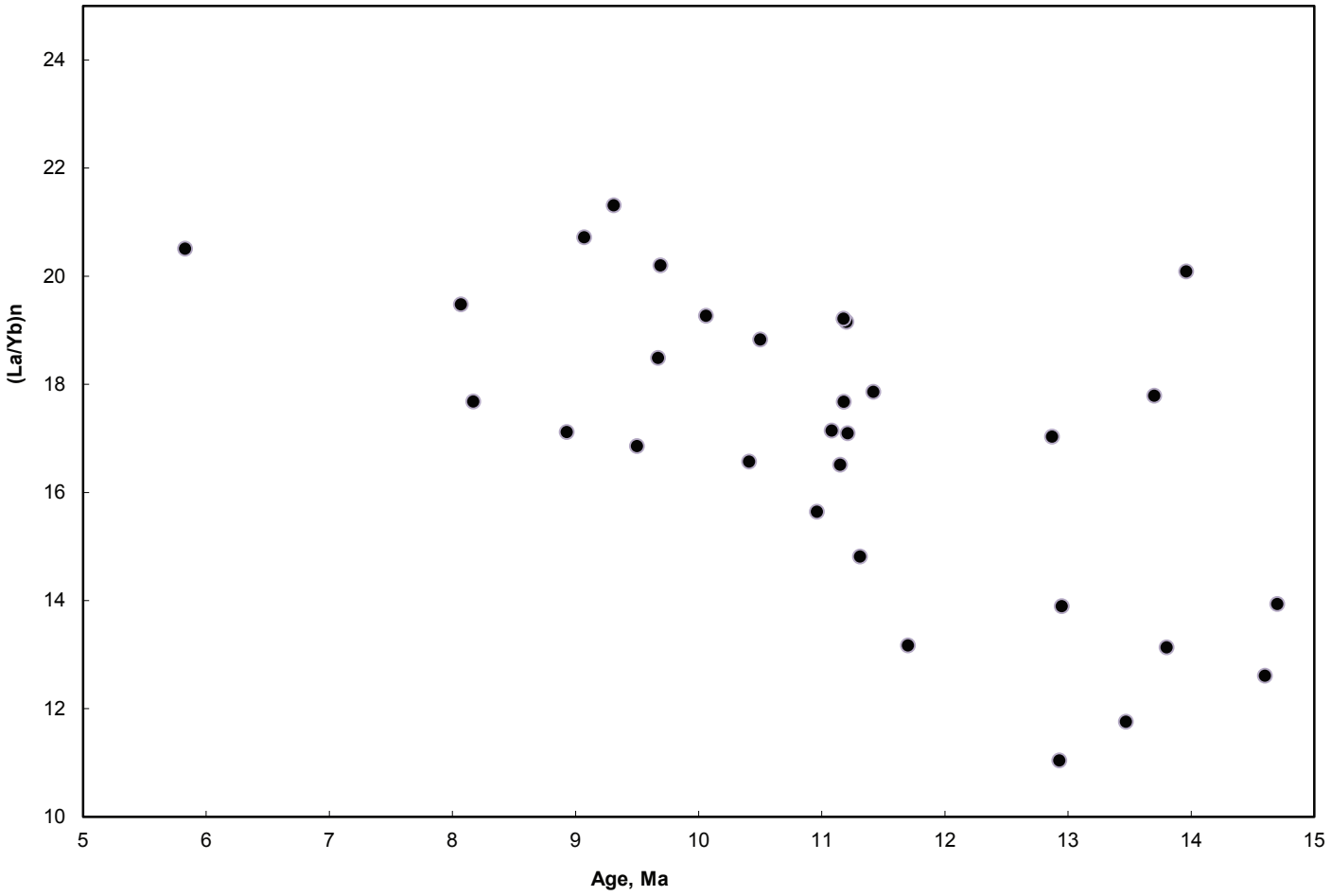

Figure S34. Variation diagram showing average $(La/Yb)_N$ versus age for map units of the Bodie Hills volcanic field (black dots).

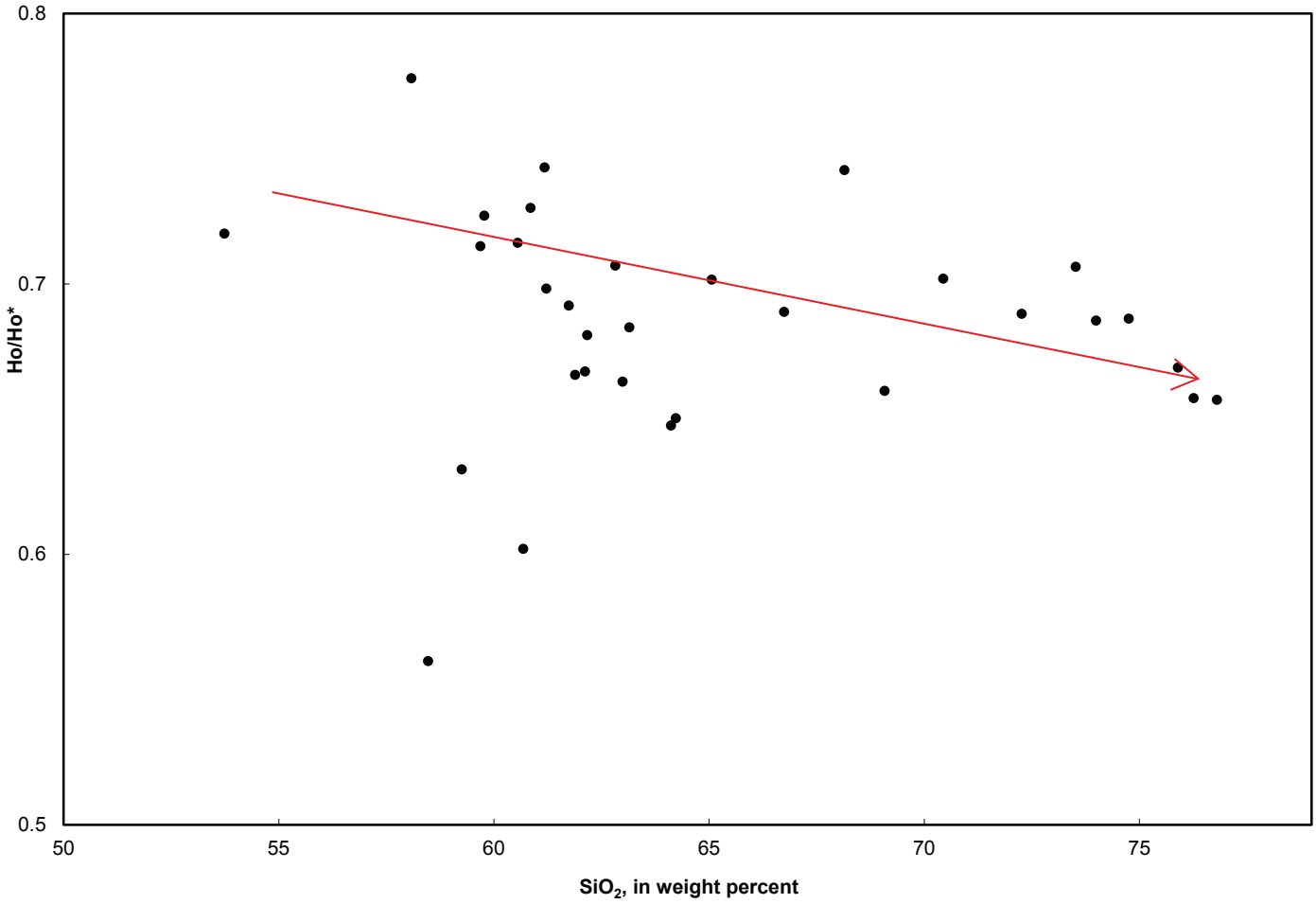

Figure S35. Variation diagram showing average Ho/Ho* versus SiO2 abundance for map units of the Bodie Hills volcanic field (black dots). Red line defines distinct fractionation trend that likely contributed to the observed compositonal variation.

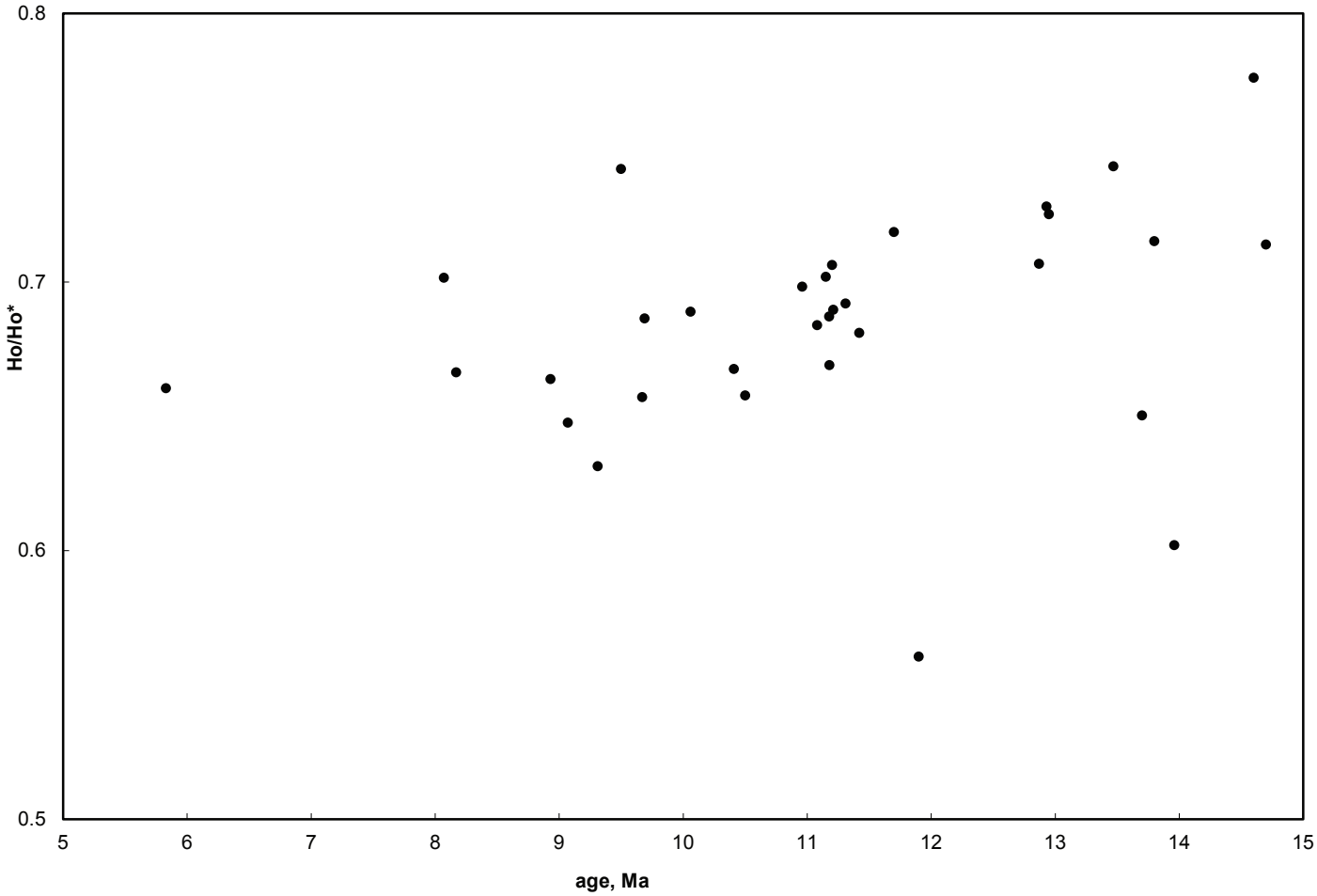

Figure S36. Variation diagram showing average Ho/Ho* versus age for map units of the Bodie Hills volcanic field (black dots).

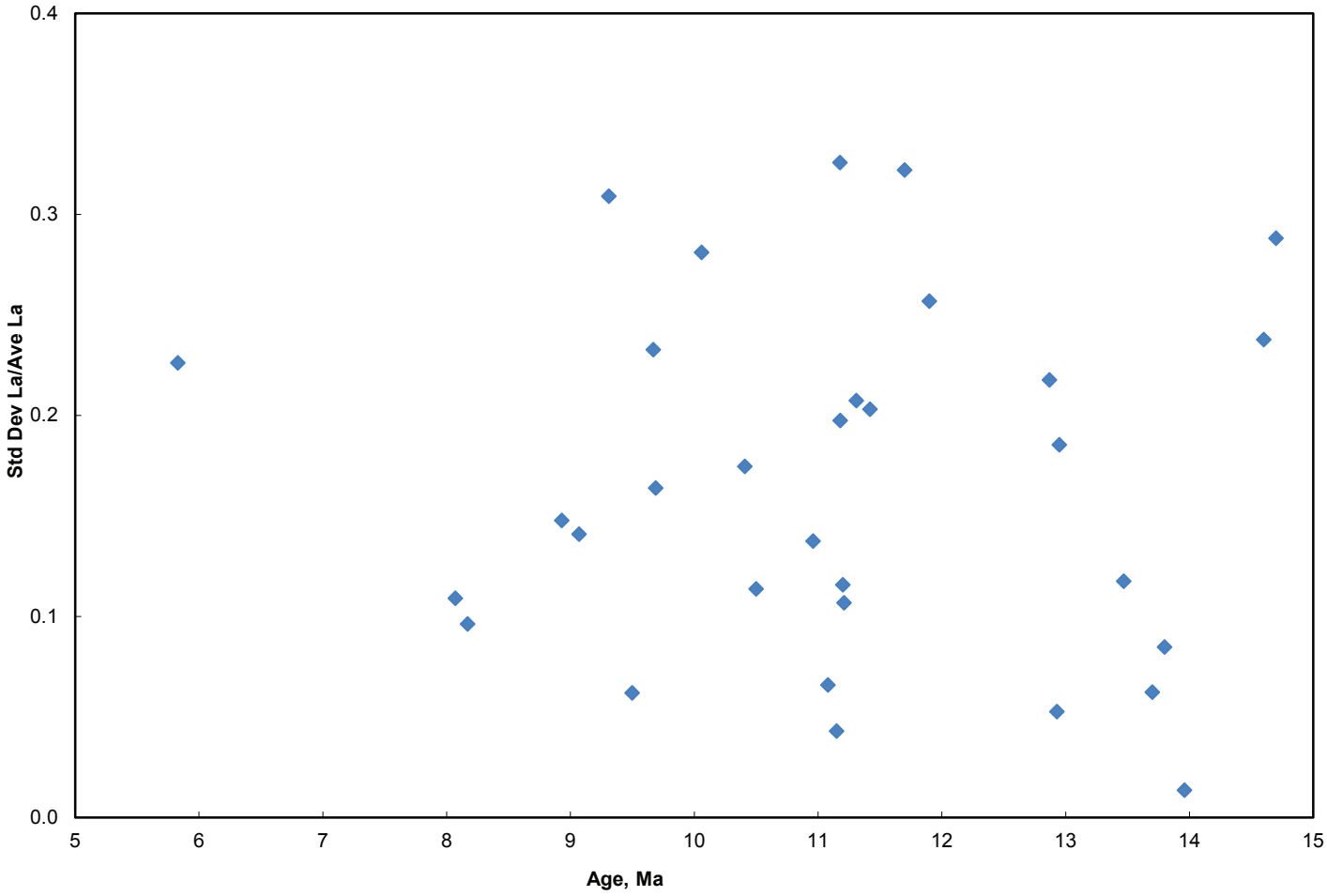

Figure S37. Variation diagram showing average standard deviation of La abundance divided by average La abundance (REE dispersion) versus age for map units of the Bodie Hills volcanic field (blue diamonds).

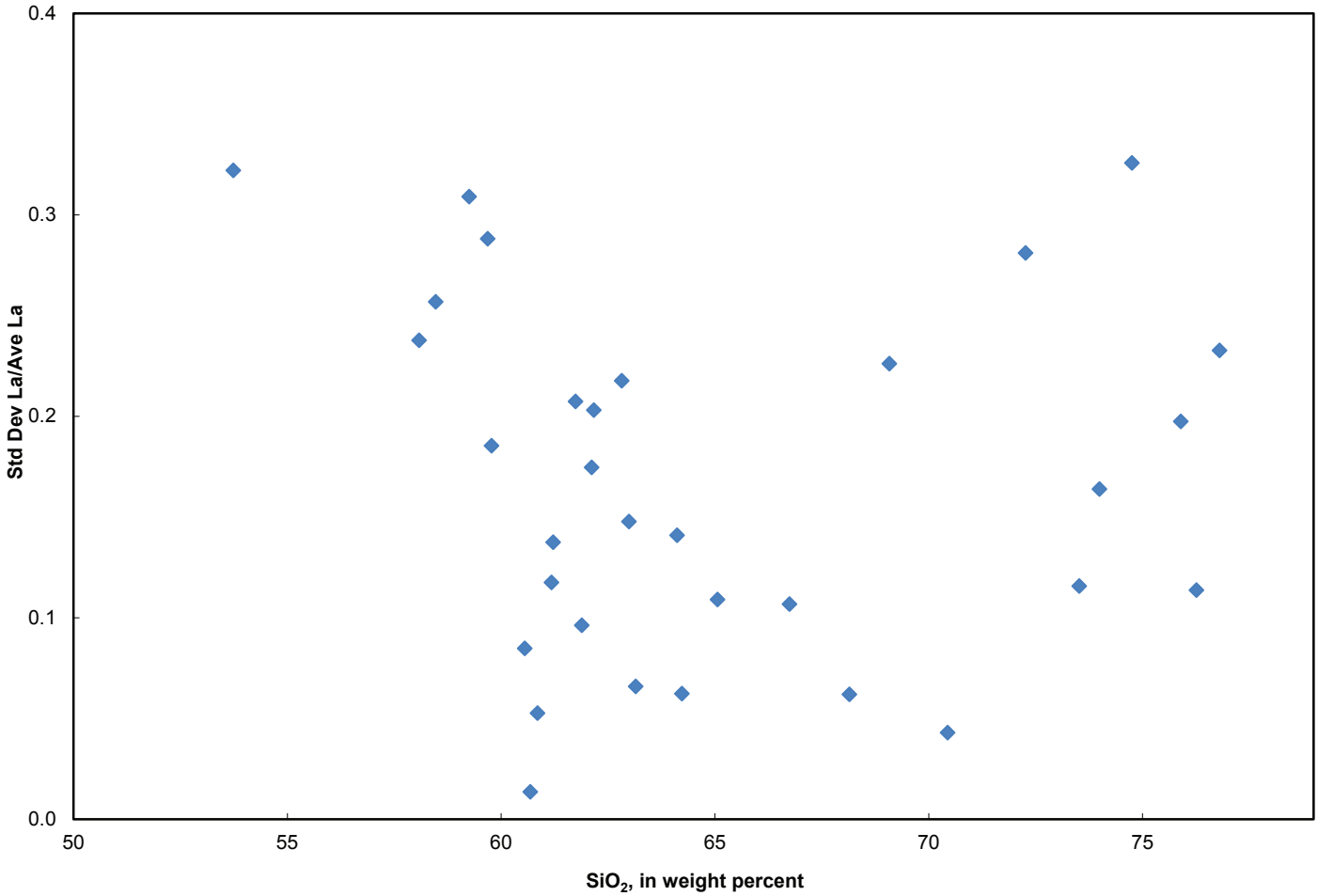

Figure S38. Variation diagram showing average standard deviation of La abundance divided by average La abundance (REE dispersion) versus SiO2 abundance for map units of the Bodie Hills volcanic field (blue diamonds).

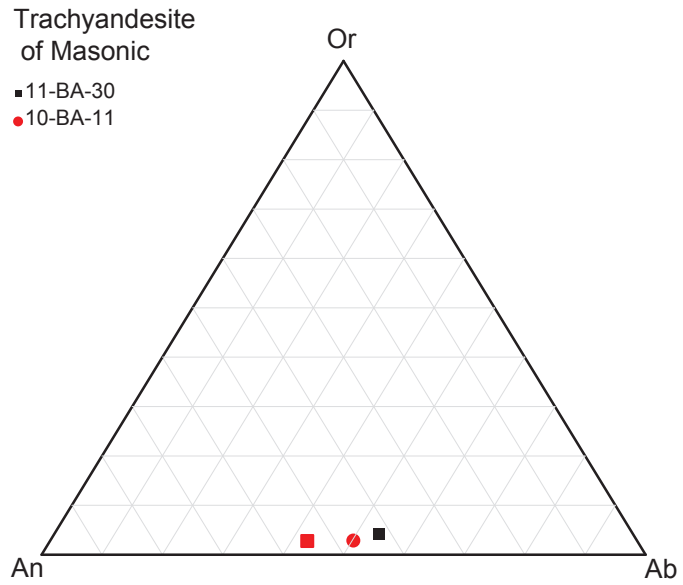

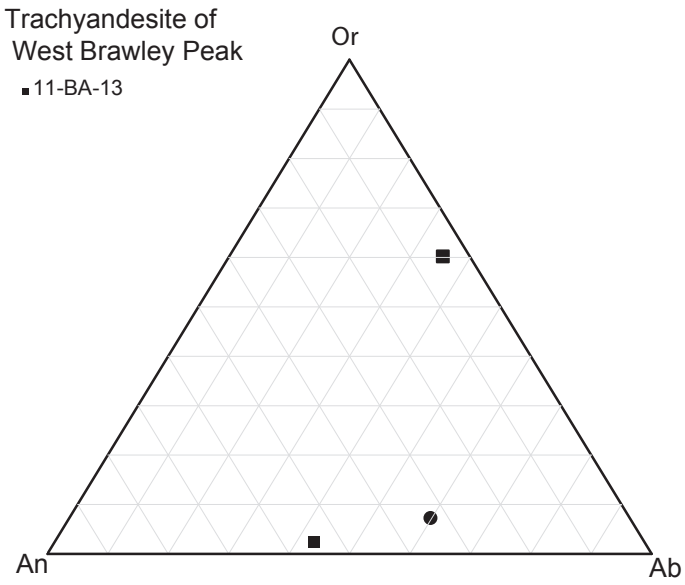

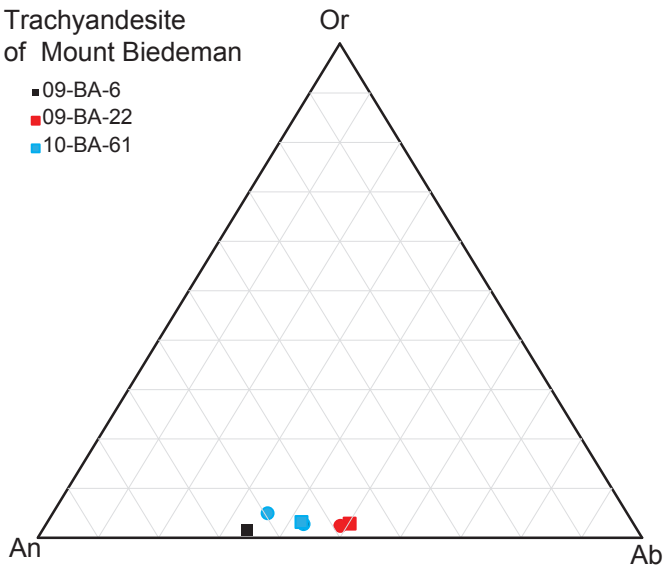

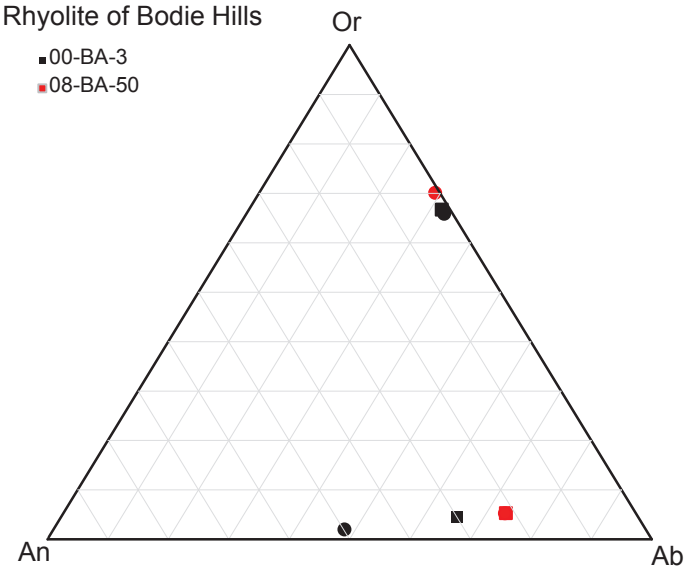

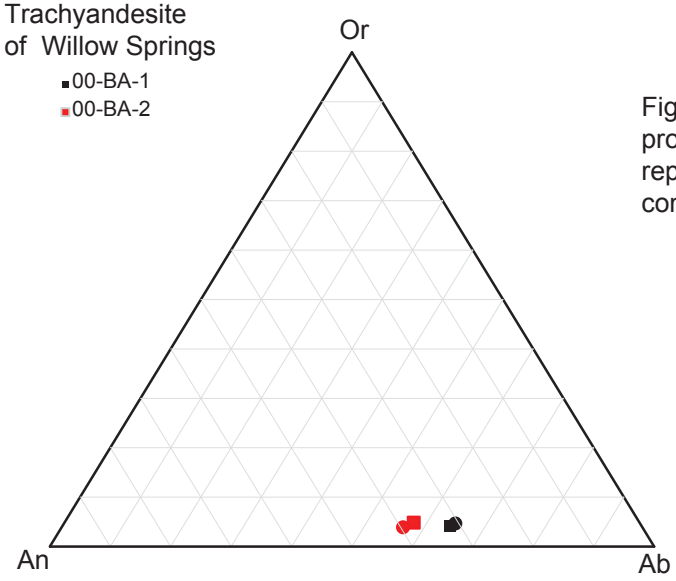

Figure S39. Ternary diagram showing molecular end member proportions of feldspars in BHVF rocks. Square plot symbols represent rim compositions and circle symbols represent core compositions.

Figure S39 du Bray, John, Cousens, Hayden, and Vikre

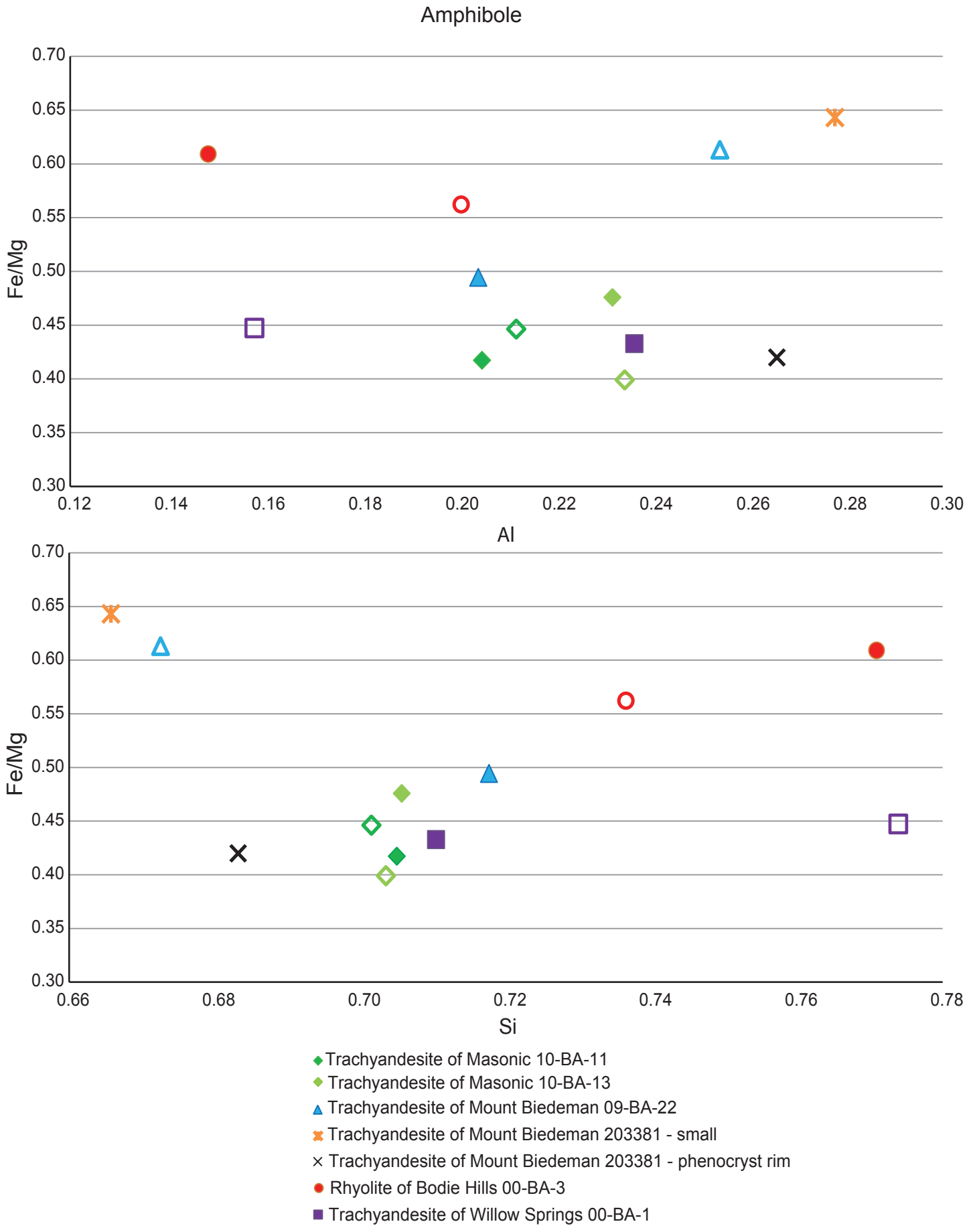

Figure S40. Diagram showing cation proportions of amphibole in BHVF rocks. Solid plot symbols represent rim compositions and open symbols represent core compositions.

Figure S40 du Bray, John, Cousens, Hayden, and Vikre

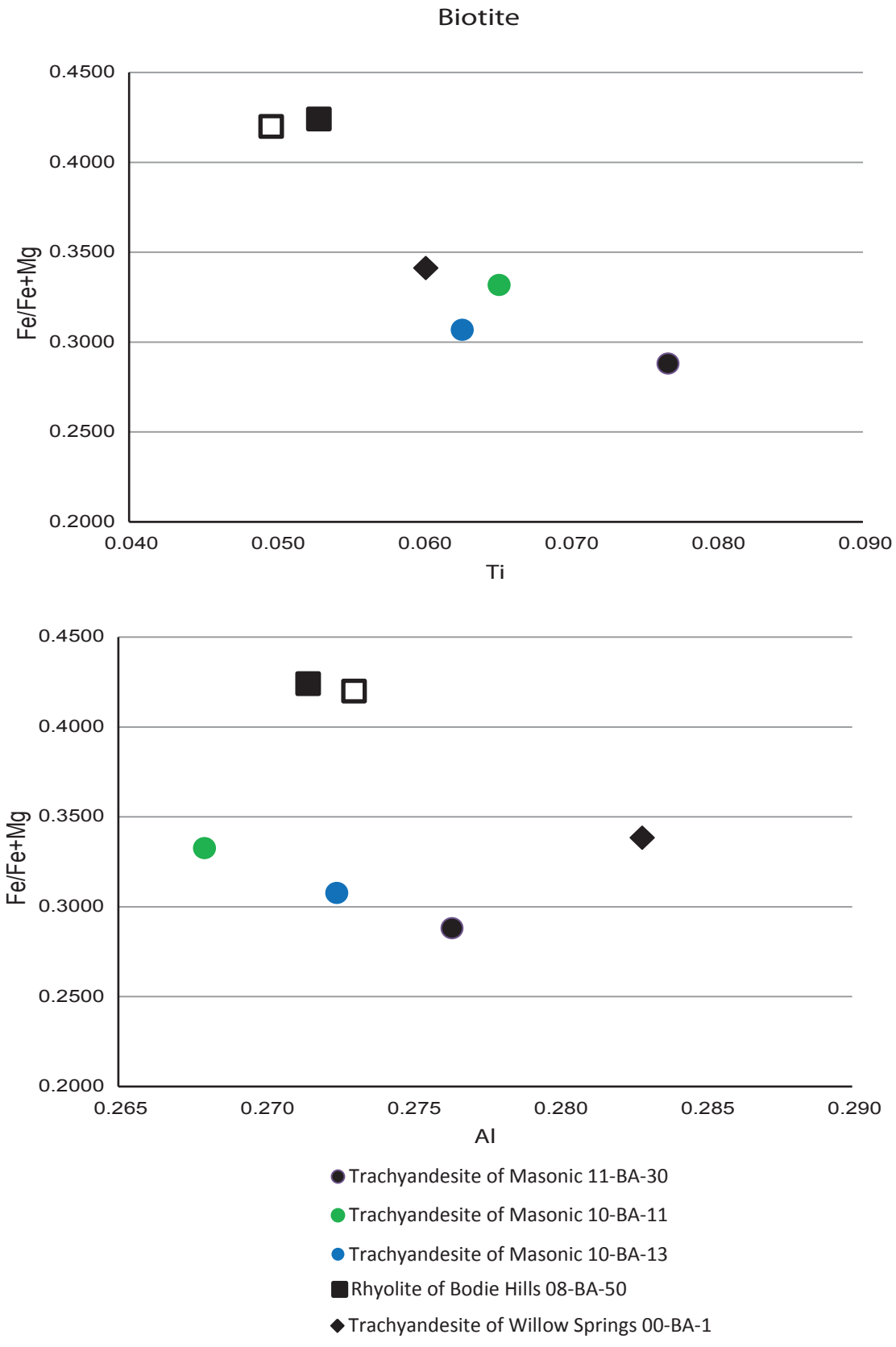

Figure S41. Diagram showing cation proportions of biotite in BHVF rocks. Solid plot symbols represent rim compositions and open symbols represent core compositions.

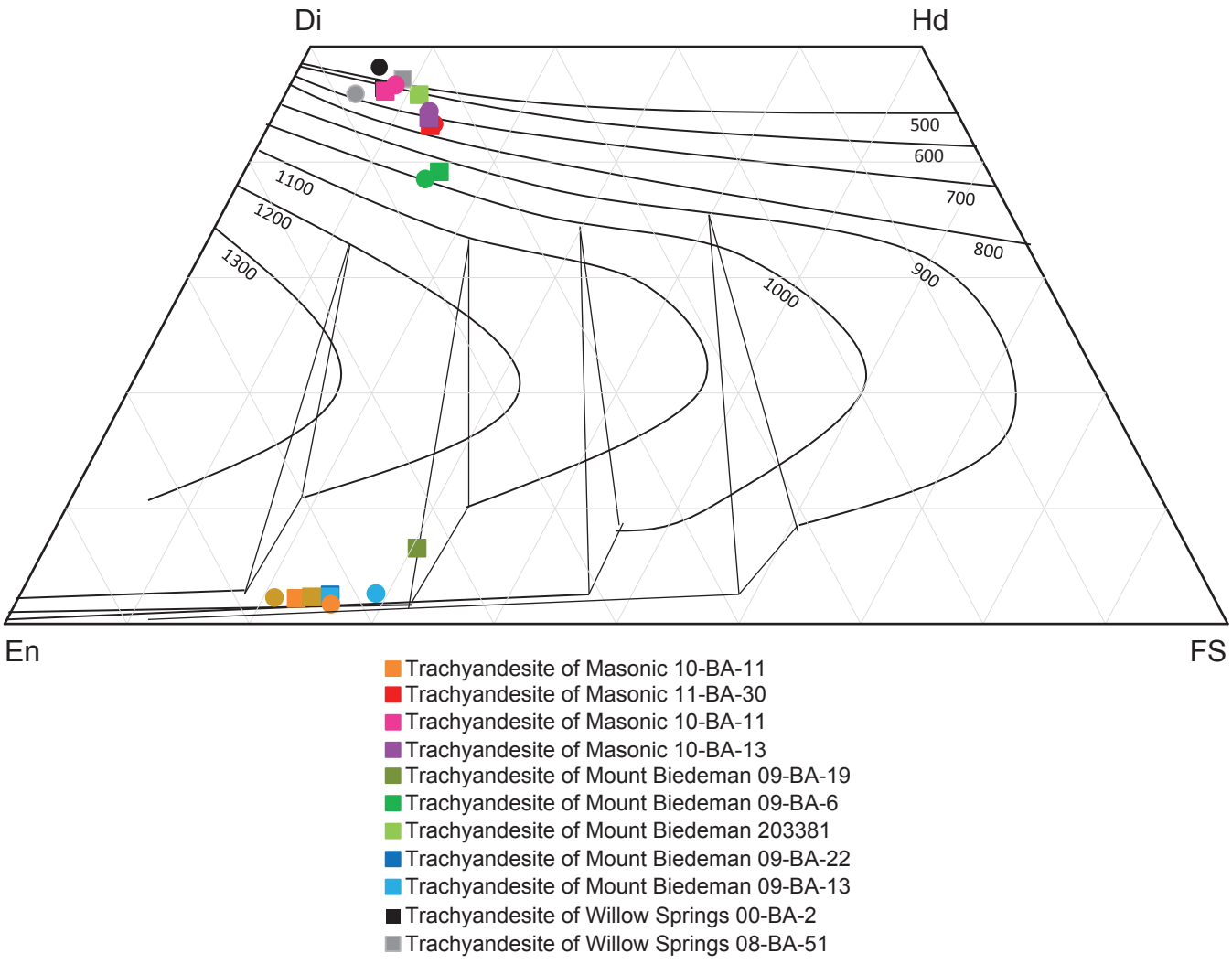

Figure S42. Ternary diagram showing molecular end member proportions of pyroxene in BHVF rocks. Temperature contours of Anderson and Linsdley (1983).

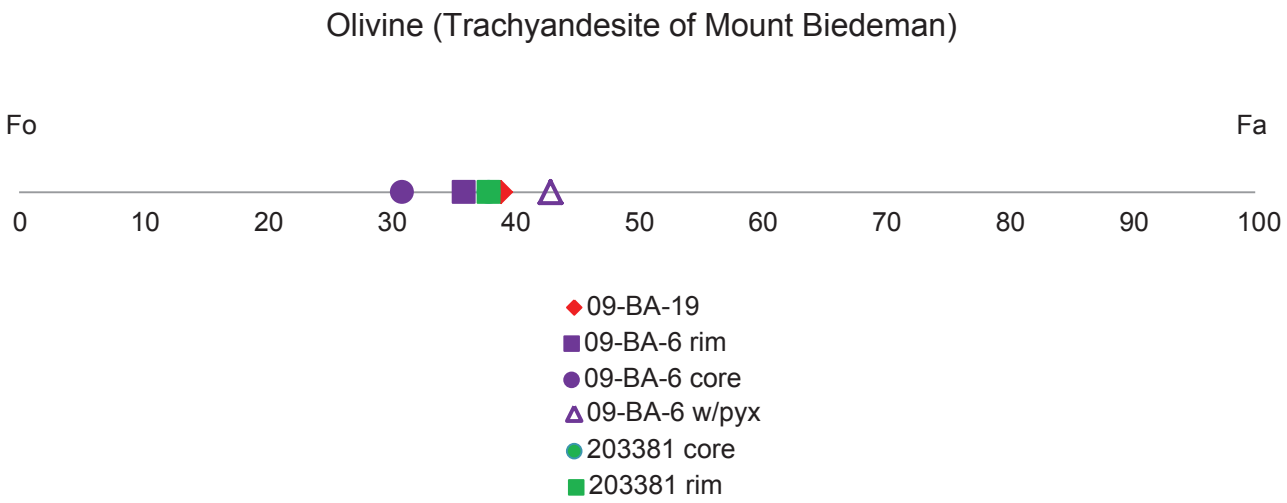

Figure S43. Diagram showing molecular end member proportions of olivine in BHVF rocks. Cores and rims as indicated.

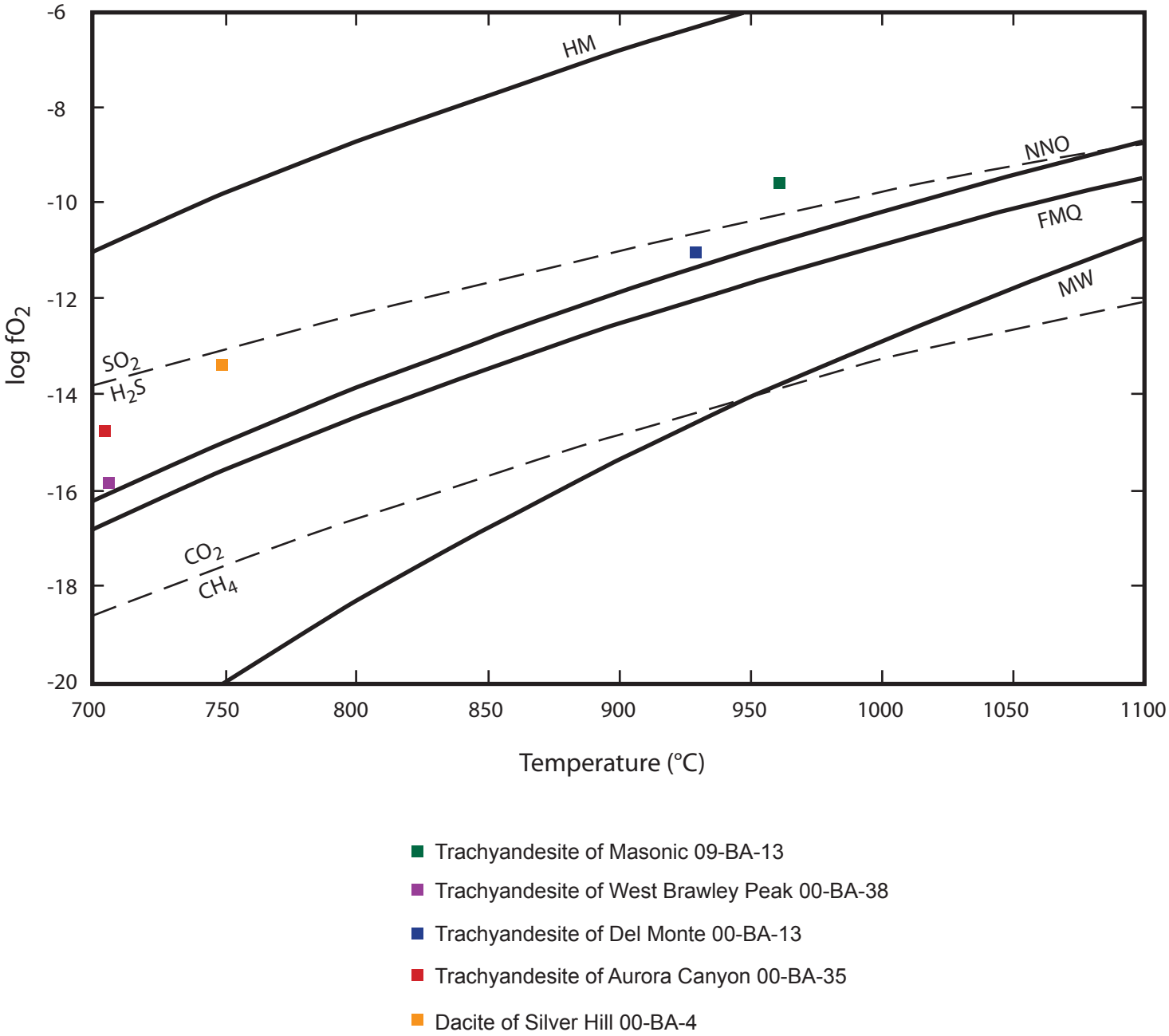

Figure S44. Temperature–log oxygen fugacity diagram for Miocene igneous rocks of the Bodie Hills volcanic field. Temperature and oxygen fugacity estimates calculated from electron microprobe analyses of rim compositions of magnetite-ilmenite pairs in glassy rocks using Fe-Ti oxide geothermometer of Ghiorso and Evans (2008). All mineral pairs checked for possible equilibrium using Mg/Mn partitioning relations (Bacon and Hirschmann, 1988). Oxygen buffer curves: FMQ, fayalite-magnetite-quartz; HM, hematite-magnetite; MW, magnetite-wustite; NNO, nickel-nickel oxide. SO_2-H_2S and CO_2-CH_4 equilibrium curves from Ohmoto and Goldhaber (1997).

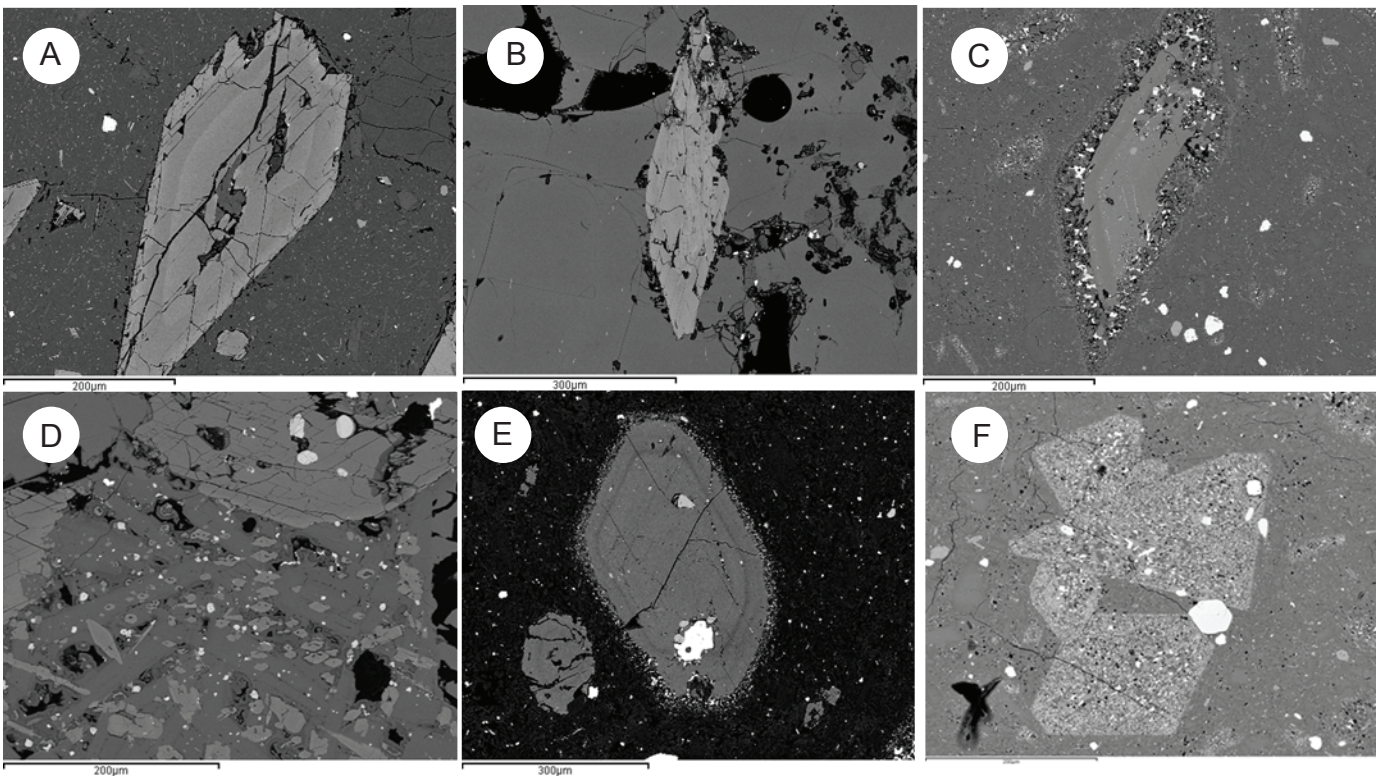

Figure S45. Scanning electron microscope back-scatter images of hornblende textures in rocks of the BHVF (sample numbers in parentheses). A) Intact hornblende with bright (high-Al) rims from the trachyandesite of Willow Springs (00-BA-01). B) Intact hornblende from the rhyolite of Bodie Hills (00-BA-31). C) Hornblende with breakdown rims. D) Large, intact hornblende phenocrysts and foliated small, skeletal hornblende in trachyandesite of Mount Biedeman (203381). E) Hornblende with narrow breakdown rim in trachyandesite of Mount Biedeman (09-BA-22). F) Hornblende with breakdown rims (C) coexist with hornblende pseudomorphs in trachyandesite of Willow Springs (00-BA-02).

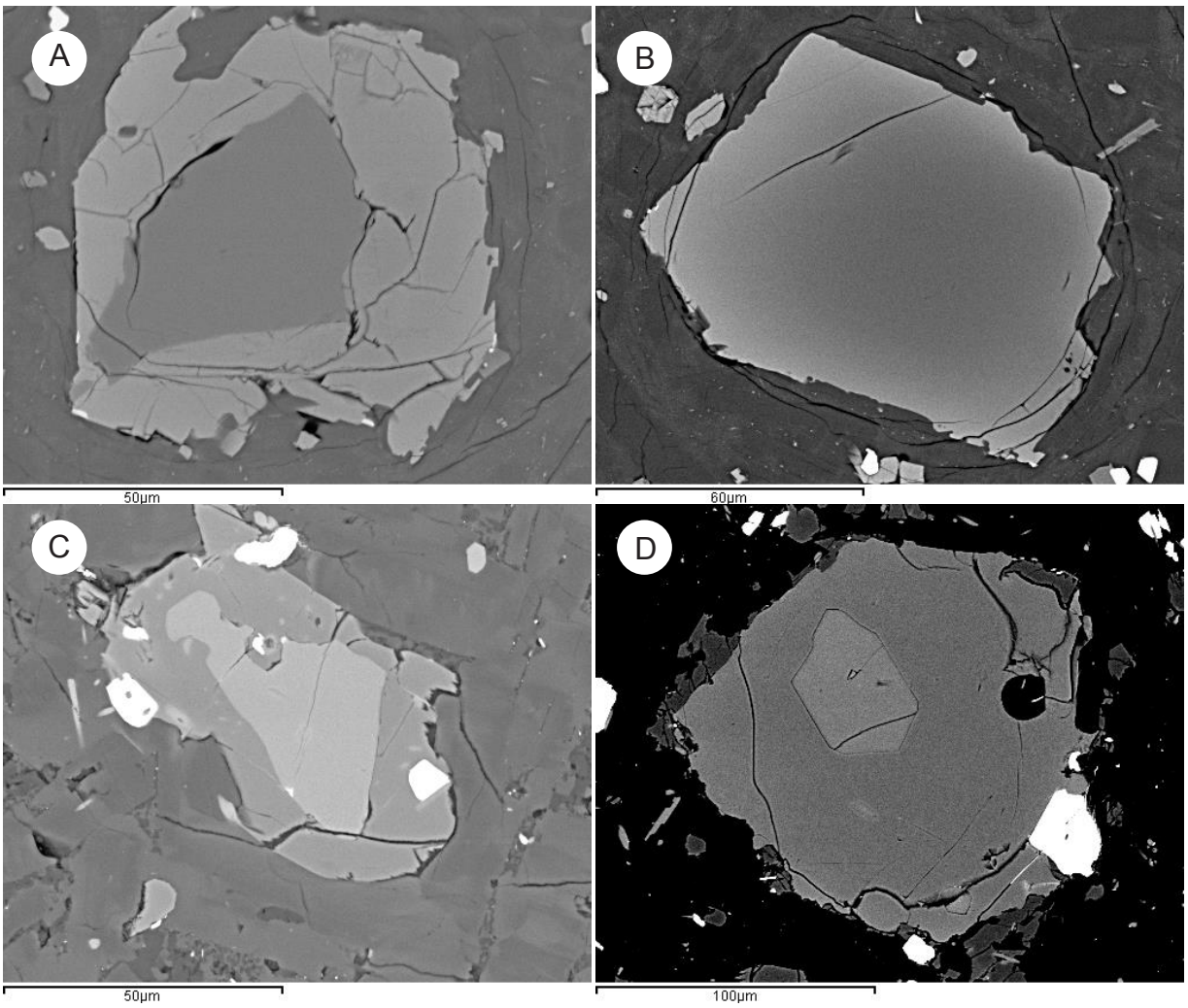

Figure S46. Scanning electron microscope back-scatter images of olivine in the trachyandesite of Mount Biedeman (sample number in parentheses). A) Unzoned olivine and olivine with pyroxene cores (10-BA-61). B) Olivine with diffuse zoning and high-Fe rims. C) Olivine with pigeonite rims (09-BA-19). D) Large unzoned olivine with an apatite inclusion (09-BA-19).

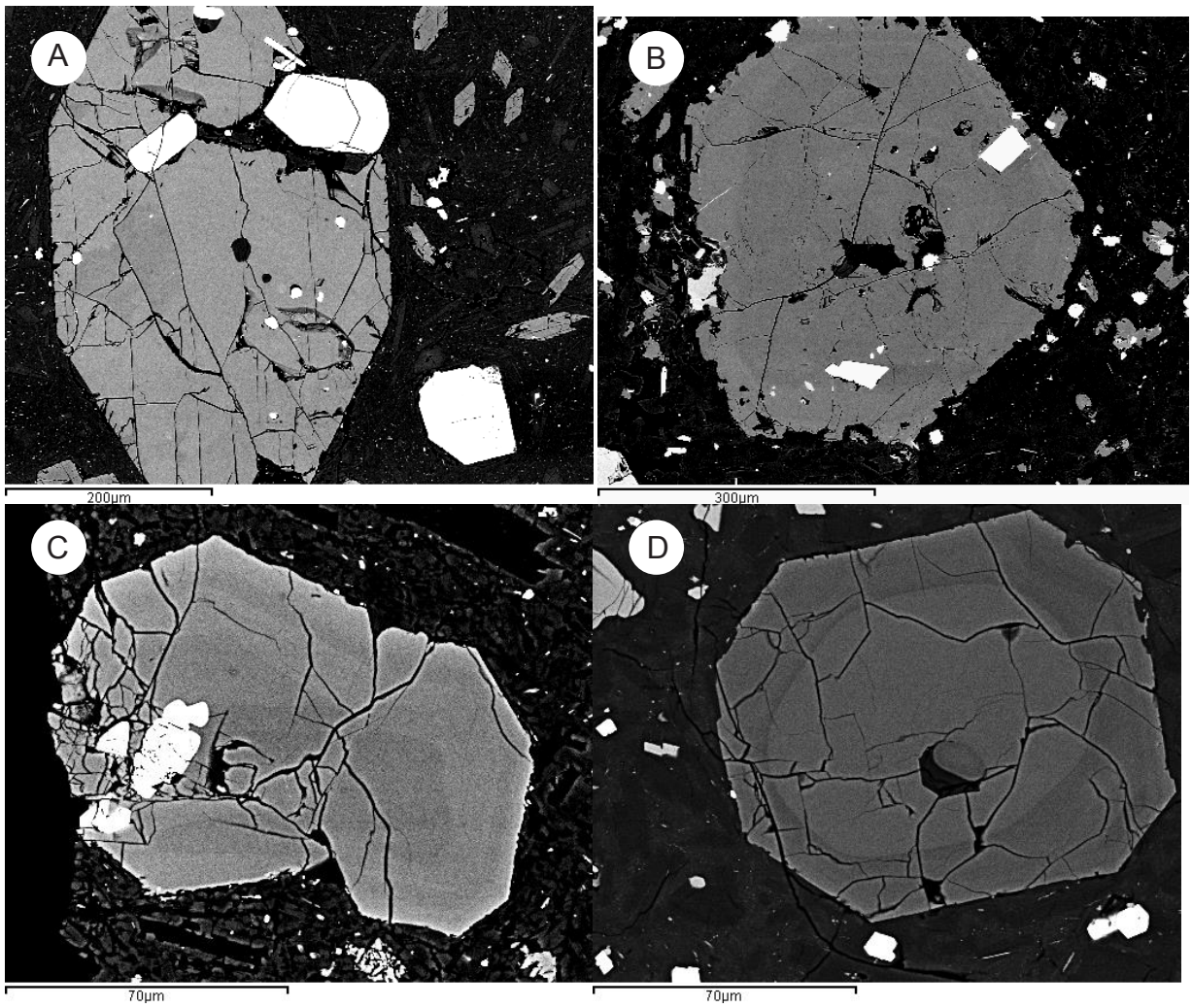

Figure S47. Scanning electron microscope back-scatter images of pyroxene textures in BHVF rocks (sample numbers in parentheses). A) Pyroxene in the trachyandesite of Willow Springs lacks systematic zoning and contains large apatite inclusions (00-BA-1). B) Pyroxene in the trachyandesite of Mount Biedeman has high-Fe rims and is composed of pigeonite (09-BA-19). C) Pyroxene in the trachyandesite of Willow Springs is step-zoned, having high-Fe rims, a Cr-rich core, and chromite inclusions (08-BA-51). D) Pyroxene in the trachyandesite of Mount Biedeman is reverse zoned, having high-Mg rims.

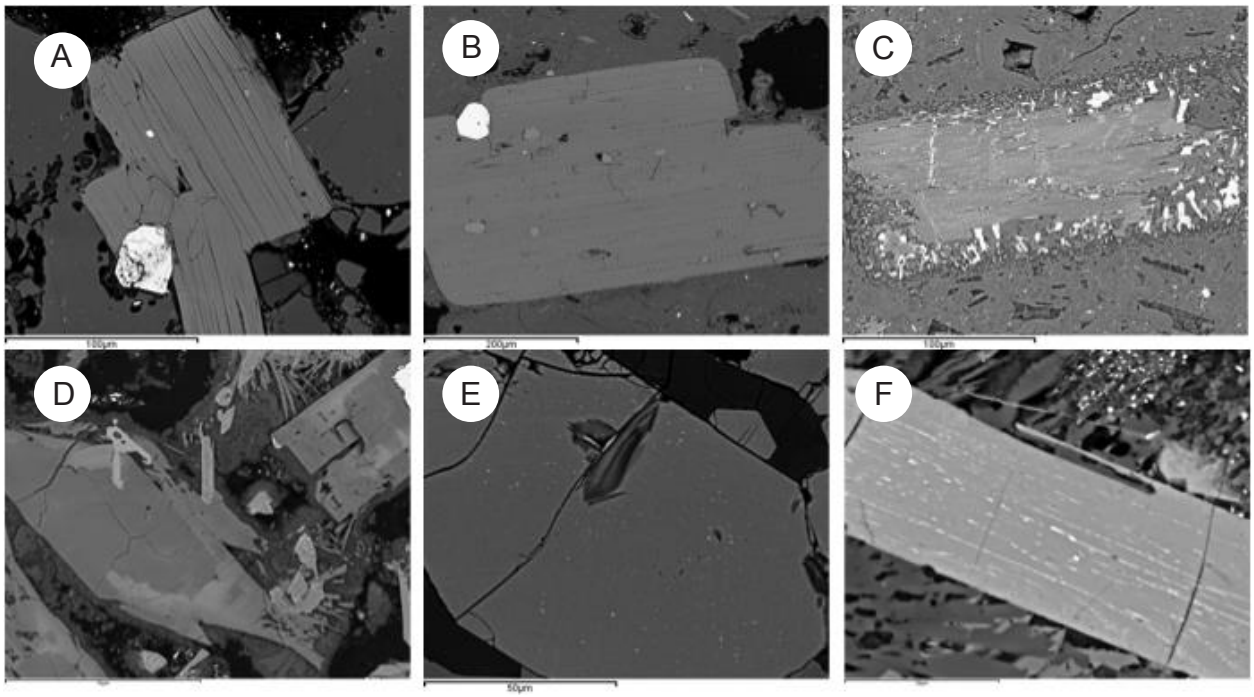

Figure S48. Scanning electron microscope back-scatter images of various minerals in BHVF rocks (sample numbers in parentheses). A) Large intact biotite from rhyolite of Bodie Hills (00-BA-31). B) Biotite in the trachyandesite of Mount Biedeman. C) Biotite pseudomorph in the trachyandesite of Willow Springs (08-BA-51). D) Extreme zoning in plagioclase from the trachyandesite of West Brawley Peak (11-BA-13); this feldspar contains extremely high Ba and Sr concentrations. E) Large, equant apatite containing small sulfide blebs from the trachyandesite of Mount Biedeman (09-BA-19). F) Bladed, skeletal apatite with streaky sulfide inclusions from the trachyandesite of West Brawley Peak (08-BA-2).

Figure S48 du Bray, John, Cousens, Hayden, and Vikre

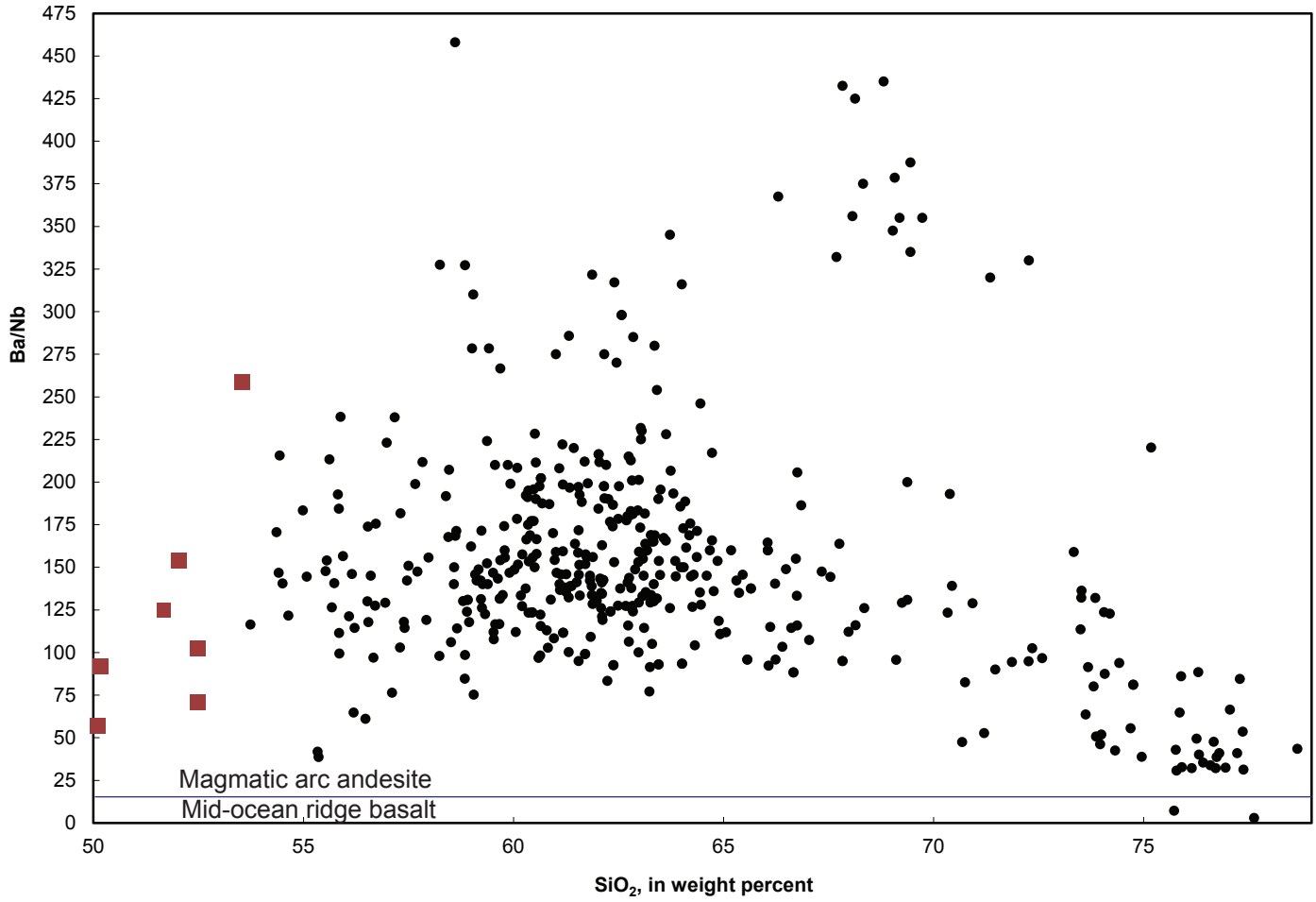

Figure S49. Variation diagram showing Ba/Nb versus SiO2 (wt%) abundances in Bodie Hills volcanic field rocks (black dots); compositions of the most primitive samples, which represent possible parental magma compositions, are shown by tan squares. Blue line at Ba/Nb = 15 (Gill, 1981) separates mid-ocean ridge basalt compositions (below line) from those characteristic of magmatic arc andesite.

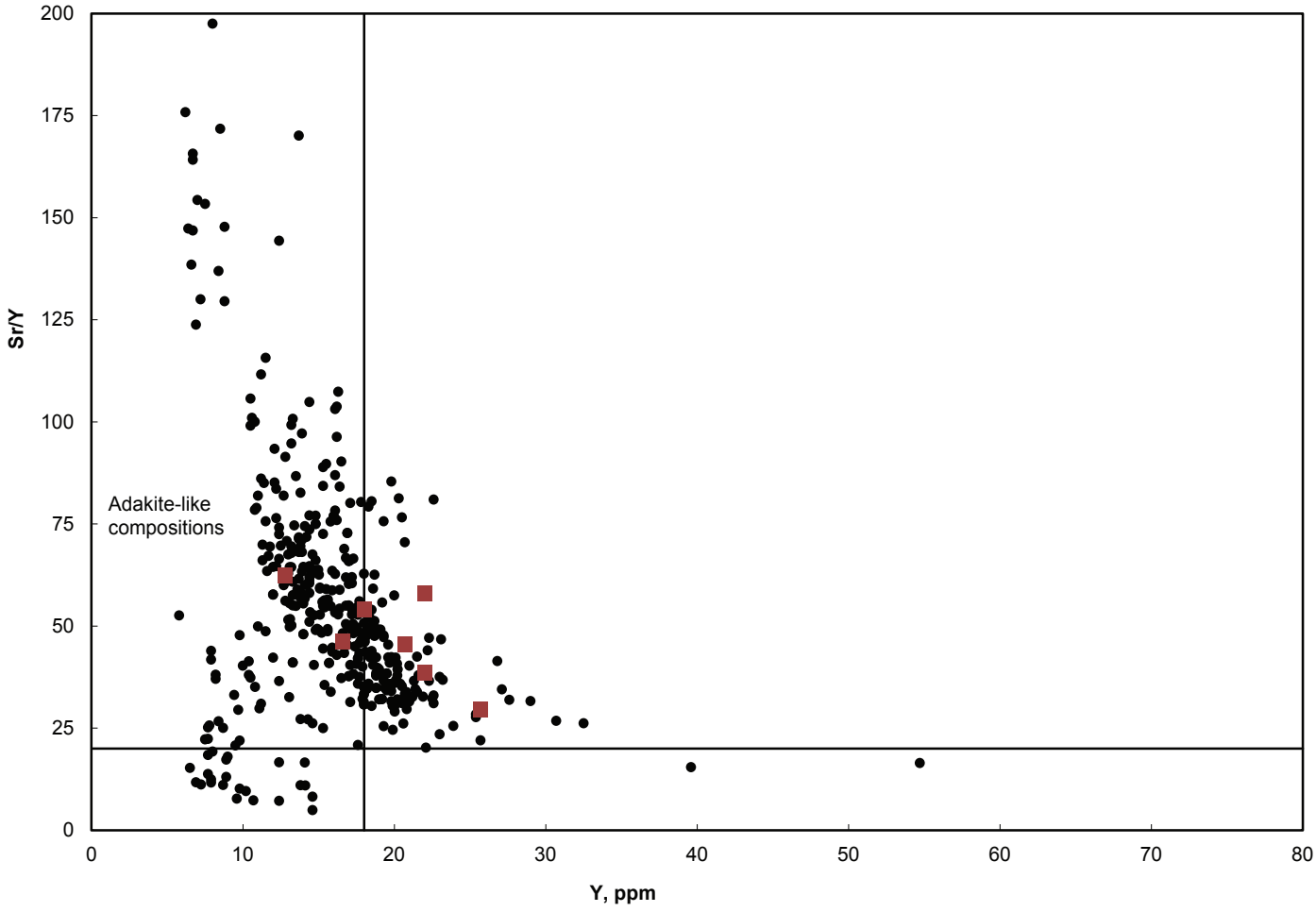

Figure S50. Variation diagram showing Sr/Y versus Y (ppm) abundances in Bodie Hills volcanic field rocks (black dots); compositions of the most primitive samples, which represent possible parental magma compositions, are shown by tan squares.

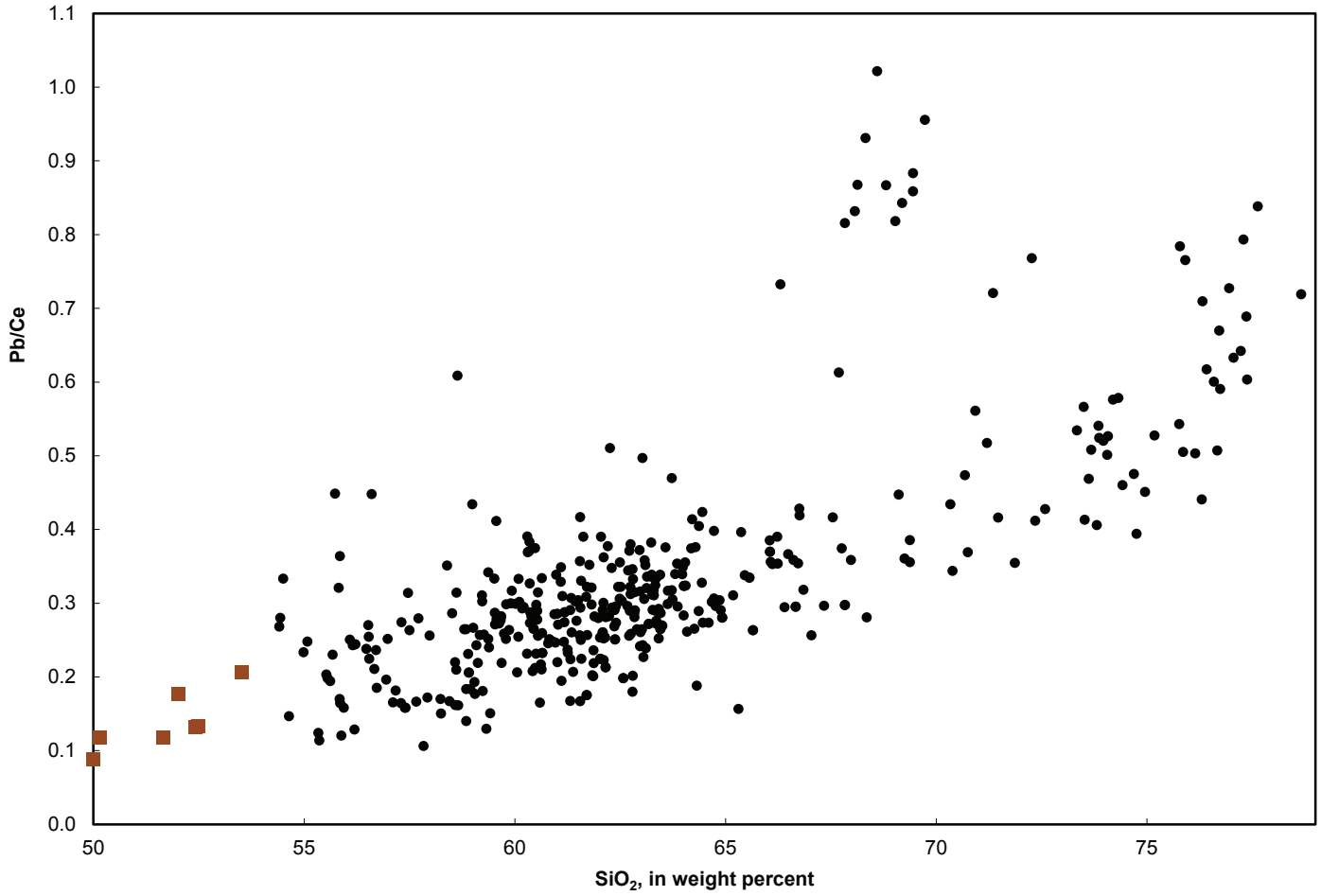

Figure S51. Variation diagram showing Pb/Ce versus SiO2 (wt%) abundances in Bodie Hills volcanic field rocks (black dots); compositions of the most primitive samples, which represent possible parental magma compositions, are shown by tan squares.

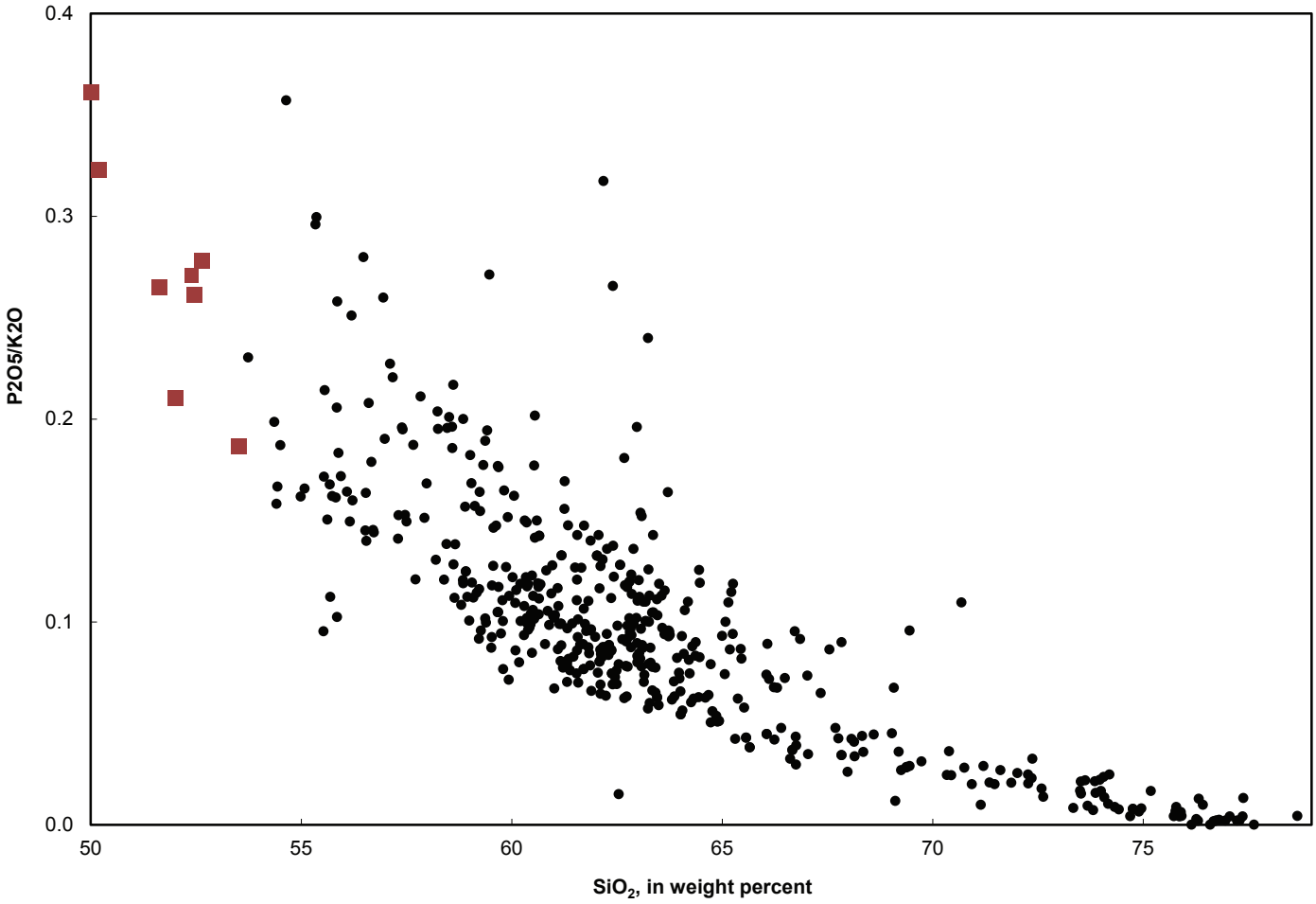

Figure S52. Variation diagram showing P2O5/K2O versus SiO2 (wt%) abundances in Bodie Hills volcanic field rocks (black dots); compositions of the most primitive samples, which represent possible parental magma compositions, are shown by tan squares.

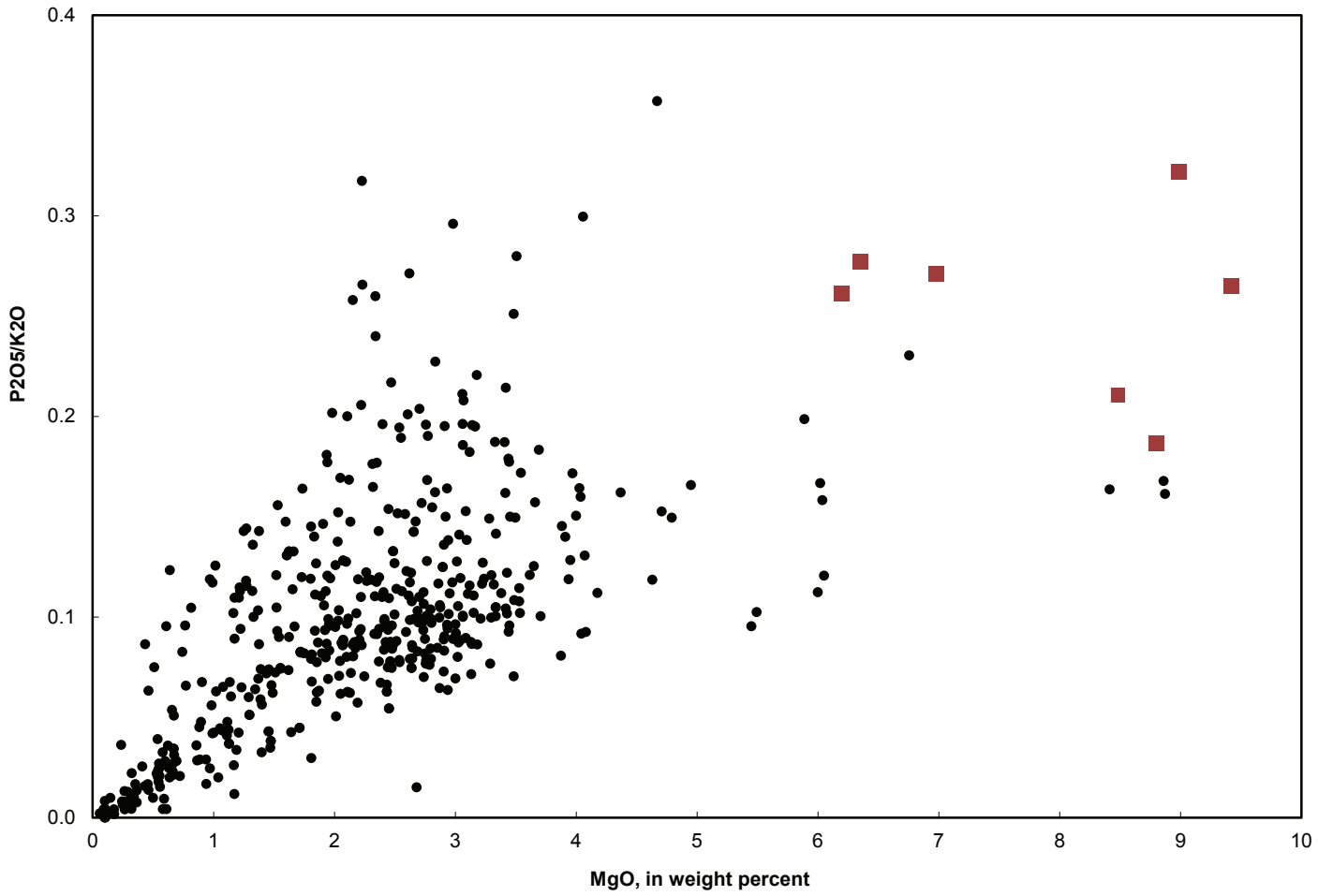

Figure S53. Variation diagram showing P2O5/K2O versus MgO (wt%) abundances in Bodie Hills volcanic field rocks (black dots); compositions of the most primitive samples, which represent possible parental magma compositions, are shown by tan squares.

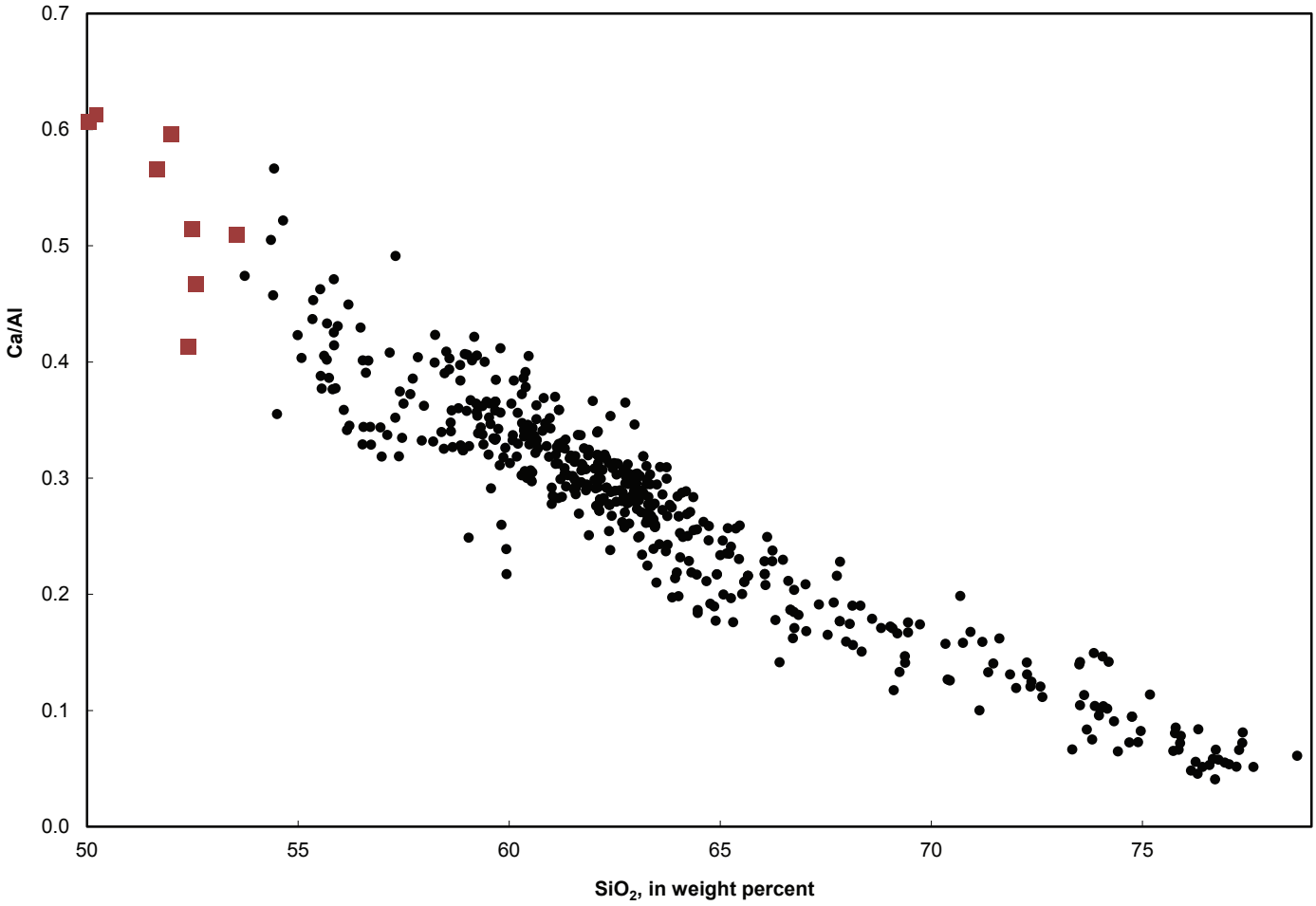

Figure S54. Variation diagram showing CaO/Al2O3 versus SiO2 (wt%) abundances in Bodie Hills volcanic field rocks (black dots); compositions of the most primitive samples, which represent possible parental magma compositions, are shown by tan squares.

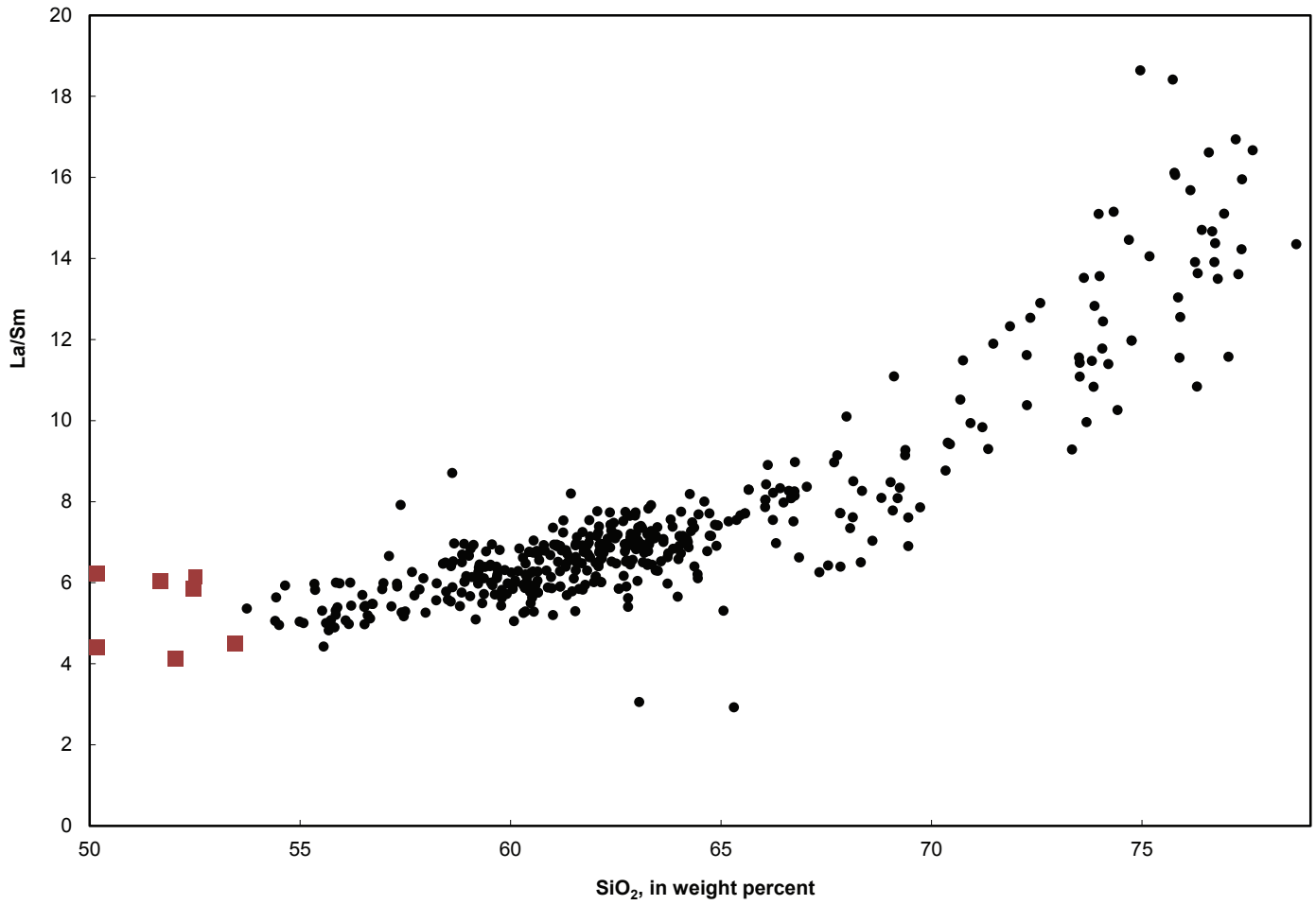

Figure S55. Variation diagram showing La/Sm versus SiO2 (wt%) abundances in Bodie Hills volcanic field rocks (black dots); compositions of the most primitive samples, which represent possible parental magma compositions, are shown by tan squares.

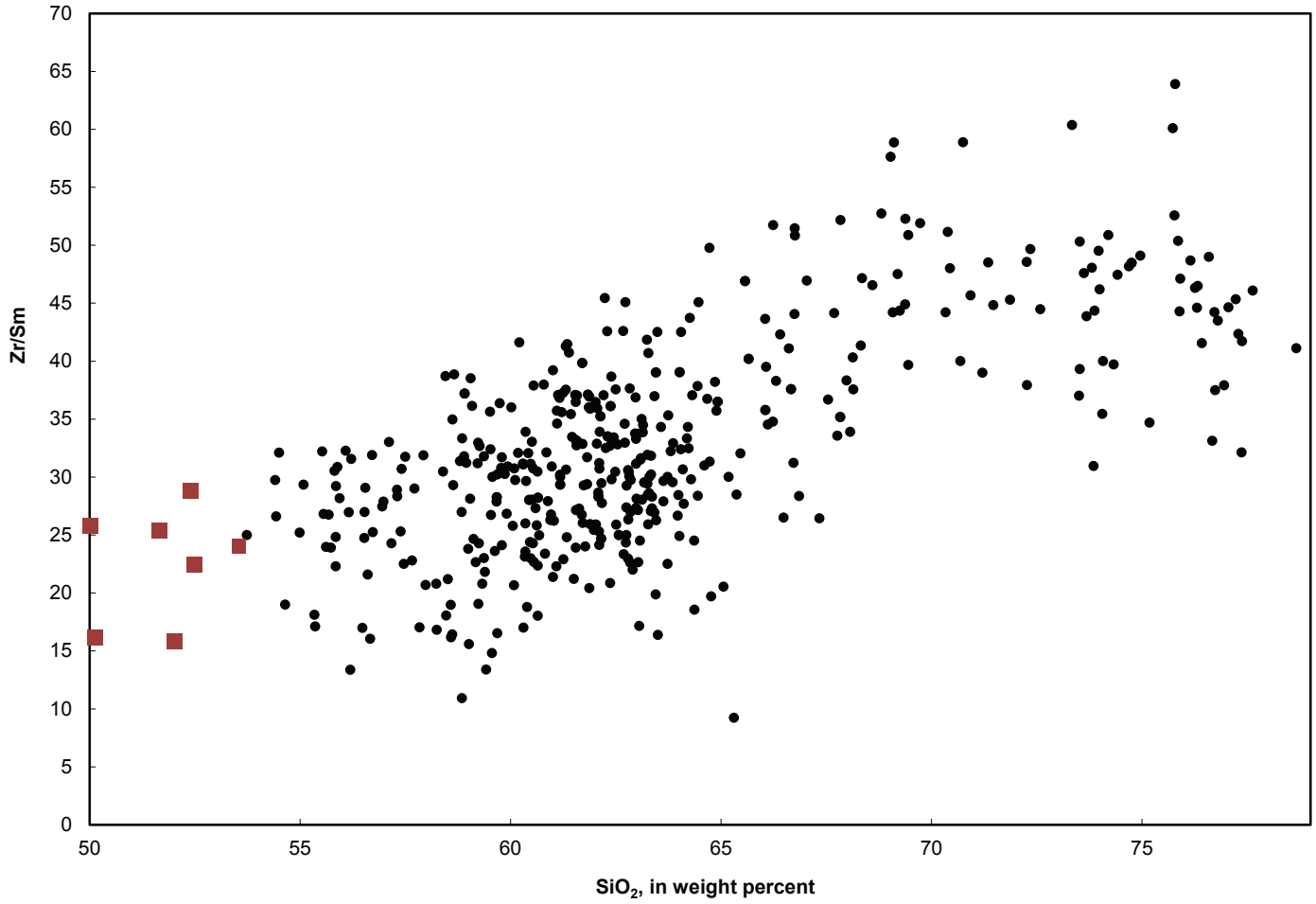

Figure S56. Variation diagram showing Zr/Sm versus SiO2 (wt%) abundances in Bodie Hills volcanic field rocks (black dots); compositions of the most primitive samples, which represent possible parental magma compositions, are shown by tan squares.